DEVELOPMENT OF SUPERCONDUCTING RF SAMPLE HOST CAVITIES AND STUDY OF PIT-INDUCED CAVITY QUENCH

A Dissertation

Presented to the Faculty of the Graduate School

of Cornell University

in Partial Fulfillment of the Requirements for the Degree of

Doctor of Philosophy

by

Yi Xie

January 2013

DEVELOPMENT OF SUPERCONDUCTING RF SAMPLE HOST CAVITIES AND STUDY OF PIT-INDUCED CAVITY QUENCH

Yi Xie, Ph.D.

Cornell University 2013

Superconducting rf (SRF) cavities made of niobium are now approaching their theoretical superheating field limit. Alternative materials such as Nb_3Sn and MgB_2 are predicted to have significant higher fields and are very interesting for next generation srf cavities. A high field and high sensitivity sample host cavity will be an ideal tool for studying various field-dependent loss phenomena and to explore the ultimate performance of these new types of rf superconductors. In this thesis, I will present my developments of two TE-type sample host niobium cavity systems which recently have reached among the highest magnetic field ever achieved ($\sim$ 60 mT) on the sample surface with nΩ sensitivity in rf surface resistance. The rf design, fabrication, surface treatments, input coupler development and rf testing results both with baseline niobium and with a Nb_3Sn sample plate will be presented in detail. Methods of improving sample surface magnetic field up to 100 mT will be presented.

Surface defects such as pits have been identified as some of the main sources of limitations of srf cavity performance. I have made a single cell cavity with 30 artificial pits in the high magnetic field region to gain new insight in how pits limit the cavity performance. The test of the pit cavity showed clear evidence that the edges of two of the largest radius pits transitioned into the normal conducting state at field just below the quench field of the cavity, and that the quench was indeed induced by these two pits. The pit geometrical informa-

tion measured by laser confocal microscopy combined with a numerical finite element ring-type defect model will be compared with temperature mapping results. Insights about quench and non-linear rf resistances will be presented.

BIOGRAPHICAL SKETCH

Yi Xie was born in Danjiangkou, China on February 12th, 1982. In 1998 he entered Chongqing University of Posts and Telecommunications. After obtaining a Bachelor's degree in telecommunication engineering in 2002, he was admitted into Peking University, Beijing where he got a Master's degree in the field of accelerator physics.

He was enrolled into Physics department of Cornell University for graduate studies in 2005. At 2007, he was brought into the field of SRF by Prof. Hasan Padamsee. After Prof. Padamsee's retirement in 2009, he was luckily enough to continue his SRF study with Prof. Matthias Liepe. His next stop will be at Euclid Techlabs and Fermilab to study traveling wave SRF structures.

To my parents, my wife and my son.

ACKNOWLEDGEMENTS

First and foremost I will thank my advisor Prof. Matthias Liepe from whom I have been fortunate enough to receive tremendous guidance and knowledge during these past years. His suggestions not only have helped me solve so many problems in my experiments, but also have been good examples to show me how to tackle a problem in a physicist's way. Matthias has also set a good example on how to be a good advisor. He has always been available whenever I needed his advice. I also want to thank him for his patience and help in improving my writing and presentation skills. In all aspects, I could not have asked for a better advisor than Matthias to guide my graduate research.

I'm greatly indebted to my former advisor Prof. Hasan Padamsee. He brought me into this fascinating field of SRF. He taught me hand to hand on how to test srf cavities even on how to transfer helium. He has always encouraged me how to become an experimental physicist.

I want to thank Prof. David Rubin on your help on showing me the opportunity of continuing PhD study within Cornell SRF group. I also thank Prof. Georg Hoffstaetter on advising me in the first two years in graduate school. I thank Prof. Saul Teukolsky serving in my special committee during graduate school.

I want to thank Dr. Valery Shemelin on your numerous advices on rf calculations. I want to thank Dr. Vadim Veshcherevich on your help on rf couplers.

I would be very thankful to LEPP drafting and machines shop guys: Tim, Tom, Don, Matt, John, Neal, Henry, Randy and Mark. Without your help, the TE cavities, the numerous subsystems and the pit cavity will never be properly fabricated.

I would like to thank current and former members of the SRF group for discussion of any problems with experiments: Alex Romanenko, Andriy Ganshyn, Mingqi Ge, Fumio Furuta, Curtis Crawford, Grigory Eremeev, Nick Valles, Sam Posen, Dan Gonella, Justin Vines, Linh Nguyen, Genfa Wu, Zach Conway, Rongli Geng, Sergey Belomestnykh, Greg Werner, Eric Chojnacki, Ralf Eichhorn, James Sears, Don Heath, Peter Quigley, John Kaufman, Brian Clasby, Benjamin Bullock, Brendan Elmore, Holly Conklin, Teresa Gruber, Paul Bishop and Greg Kulina.

I would like to acknowledge Peggy Steenrod and Monica Wesley for providing me the necessary adminstration support.

Personally, without my wife and parents' support, my graduate school life will be impossible. For all my friends who have finished and have left graduate school at Cornell, I can't name all of you but you are forever remembered as such an important part of my youth.

TABLE OF CONTENTS

LIST OF TABLES

LIST OF FIGURES

CHAPTER 1

INTRODUCTION

1.1 Motivation for cavity research

Superconducting radio frequency (srf) cavities have been transformational for the scientific potential of past and current particle accelerators. Superconducting rf will be a key technology for many future accelerators because of the outstanding efficiency of this technology. This will be especially true for accelerators requiring continous wave (cw) or long rf pulse length such as next generation light sources, single-pass Free Electron Laser (FEL), Energy Recovery Linac (ERL)-based light sources, high-intensity proton linacs for spallation sources and transmutation applications. Compared to normal copper structures, superconducting cavities dissipate more than six orders of magnitude less power due to the small rf surface resistance of superconducting materials. This greatly reduced operating power demand, even taking into account the efficiency of the cryogenic refrigerator (about 1/1000), translates into less capital cost, less operation cost (electricity) and also enables operating superconducting cavities at higher cw gradient of $15 \sim 40$ MV/m compared to copper cavity of 1 MV/m. In addition, superconducting cavities impose less disruption to the particle beam due to their larger apertures and provide a high degree of freedom of operational flexibility.

Niobium has the highest critical temperature T_c = 9.25 K and thermodynamic critical field $B_c \sim 200$ mT among all the elemental superconductors [1]. Bulk niobium is predominantly used to fabricate superconducting rf cavities due to its good metallurgical properties. Accelerating fields of $35 \sim 50$ MV/m at intrin-

sic quality factors Q_0 of $1 \sim 2 \times 10^{10}$ at 2 K are currently achieved in state-of-art single cell and multi cell cavities made out of niobium. The highest accelerating field ever reached in a niobium single-cell cavity was 59 MV/m (206 mT), which is well above the lower critical field B_{c1} = 170 mT of niobium [2]. In fact a metastable superheating field B_{sh} determines the maximum surface magnetic field a superconductor can withstand before magnetic flux starts to penetrate into the superconductor. Recently theoretical efforts by solving Ellenberger equations have been able to determine B_{sh} of $210 \sim 250$ mT for niobium at 2 K, depending on the RRR of the niobium. Since the fields in niobium cavities have reached values near the theoretical limit already, new materials need to be explored for srf applications. Alternative materials such as Nb_3Sn and MgB_2 are predicted to have more than 400 mT superheating fields at 2 K (corresponding to > 100 MV/m accelerating field in a srf cavity) [3]. In addition, Nb_3Sn has smaller BCS rf surface resistance compared to niobium from its larger energy gap. There are also theoretical predictions that the maximum cavity field can be greatly increased with alternating layers of a superconductor and a dielectric coating the inner surface of a cavity, which might prevent strong rf dissipation due to vortex penetrations [4].

Currently many new materials such as MgB_2 are only available in small flat samples. Measuring sample surface resistance R_s and its dependence on frequency f, temperature T, external magnetic field H and sample anisotropic properties is the crucial first step towards new material application for next generation srf cavities. One aim of this thesis is to develop a new generation sample host cavity system which allows testing the rf performance of small, flat sample plates and can reach relatively higher field on the sample surface to characterize new material such as Nb_3Sn and MgB_2. In addition, the sample host cavity sys-

tem can be used to systematically study the field dependence of the rf surface resistance at high magnetic surface fields.

Another field gradient limit of niobium srf cavities is the presence of small defects on the inner surface which can limit the maximum fields to values well below the theoretical limit. Recently irregularities such as small pits-like structures have been suspected to trigger cavities to quench at fields significant lower than the critical field of the niobium superconductor [5]. Identifying the cause for these pits-induced quenches will greatly benefit all projects which require reliably reaching accelerating fields above 20 MV/m. Therefore the other aim of this thesis is to use a single cell niobium cavity with artificial pits drilled into the inner surface as a test bed for gaining insight of why and how pits trigger cavity quenches.

1.2 TE-type sample host cavities as tools for basic superconducting material research

In order to reproduce conditions similar to those in a particle accelerator, usually entire srf cavities are tested to study a specific processing procedure, a new coating method or to investigate the rf surface resistance and its field dependence. But with the cost and time involved in preparing and testing whole cavities, obtaining a statistical significant data set of cavity performance can become challenging. In addition, studying correlations between cavity performance and superconducting material surface features is central in understanding different cavity loss mechanisms. Yet many surface analytical tools such as XPS, SEM and EBSD can not be readily applied to an enclosed cavity shape. Therefore it

would be very desirable to test the RF performance of small, flat sample plates instead of fabricating and processing entire cavities. Also, new materials such as MgB_2 on are available currently on small flat samples. For many years, a variety of sample test cavity systems have been developed with the aim of rf testing material samples in-situ. Tab. 1.1 shows an incomplete list of preceding sample host cavities with their maximum field, area of sample, surface resistance sensitivity and operating frequency. Although each design has its own specific capabilities, none of them can achieve high rf magnetic field e.g. ≥ 50 mT on the sample surface with enough sensitivity in surface resistance of ≤ 1 nΩ. As a result of these limitations in field or sensitivity, none of them has become a real workhorse for sample studies.

Two main methods have been used in the past to determine the surface resistance of the samples in a host cavity. In the following, the basic principle of each method is explained, and a summary of previous sample test systems using these methods is given.

The RF method

In this method, the material sample is one part of the resonating cavity and contributes to the total losses. The sample typically is used as an end-plate of a TE mode cavity. Transverse-electric (TE) modes have long been used in srf sample host cavities in which the bottom plate is the removable sample because the joint losses between the sample end-plate and the cavity body are ideally zero. Microwave joint filters can be used to further decrease the rf losses at the joints. Thus a TE-type sample host cavity potentially can provide the best baseline unloaded quality factor Q_0. Moreover, the fact that there is no electric field perpendicular to cavity surface in TE modes make the srf cavity less vulnerable

Table 1.1: A list of sample host cavities for srf material characterizations

f (GHz)	Sample area (cm^2)	R_s sensitivity (nΩ)	Maximum sample field (mT)	Reference
8.6	0.9	10^4	very low	Allen et.al., 1983
5.7	40	~10^3	15	laurent et.al., 1983
3.5	127	1	2	Kneisel et.al., 1986
5.95	20	1.5×10^4	unknown	Moffat et.al., 1988
0.17~1.5	~1	2.0×10^3	64	Delayen et.al., 1990
10	1	10^4	unknown	Taber et.al., 90
34	35	2.0×10^6	unknown	Martens et.al., 91
1.5	4.9	1	25	Liang et.al., 1993
0.403	44	1	25	Mahner et.al., 03
11.4	19.6	>10^4	> 150	Nantista et.al., 05
5.95	35	2.0×10^3	45	Romanenko et.al., 05
7	1	10^4	0.15	Andreone et.al., 06
0.6~10	<0.1	<100	≤5	Oats et.al., 06
3.54	22	unknown	50	Ciovati et.al., 07
0.4~1.2	44	unknown	51	Junginger et.al., 09
7.5	20	< 100	< 12	Xiao et.al., 12

to field emission. Therefore their cavity preparation process is relatively easier compared to normal srf cavities that are excited in transverse-magnetic (TM) modes. By measuring the whole cavity quality factor first with the unknown sample plate and then with a reference sample plate, the surface resistance of the unknown sample plates can be deduced. Thus the sample surface resistance measured is the average surface resistance of the sample plate and does not provide any information about its potential variation over the area of the sample. An improved version of this method is adding a thermometry system outside the sample plate. From the temperature map data much more accurate surface resistance information can be obtained at specific areas of the sample and the measurement resolution can be greatly improved to below nΩ.

Prior to the work reported here, the highest surface field achieved on the sample in a TE cavity was no more than 45 mT [7]. The earliest effort can be traced back to 1983 when a 6 GHz pillbox cavity with demountable end-plate was made at CERN. It reached 15 mT with a Q_0 above 10^9 [6]. The most recent development was in 2004, when a 6 GHz pillbox cavity was tested to around 20 mT with Q_0 around 10^8 [7]. A normal conducting, mushroom shaped TE cavity has reached sample surface fields above 150 mT. However, since it has to be operated with very short rf pulses and heating is dominated by the normal conducting host cavity, it only gives very poor resolution of surface resistance in the mΩ range [8].

The calorimetric method

In a calorimetric system, a heater and a thermometer are attached to the sample which is thermally isolated from the host cavity. The host cavity can be of different type such as a triaxial cavity [9], quadrupole mode resonator [10]

and sapphire loaded TE pillbox cavity [11]. A triaxial cavity developed at JLAB reached a maximum field of 25 mT, limited by multipacting [9]. A quadrupole resonator developed at CERN reached above 50 mT [10]. But the sample need to be welded and also has an extra loss due to currently flow at sample edges. A sapphire loaded pillbox cavity develped at JLAB reached less than 20 mT because of a significant joint loss issue [11].

I have designed and optimized an improved type of TE cavity with the aim of achieving a improved performance so that it becomes a fully usable system. The previous designs have either low sample to field ratio, using normal conducting materials, poor processing techniques or are without a T-map system attached. For example, revious TE-type sample host cavity designs use a simple pillbox shape in which the maximum magnetic field is not located at the sample surface. Our optimized cavity design increases the ratio of maximum magnetic field on the sample to the maximum field on the walls of the host cavity. Given the ratio now ≥ 1, the critical field of alternative superconducting material samples such as Nb_3Sn and MgB_2 can possibly be tested. Also compared to all previous efforts, we built the sample host cavity using high purity niobium and treated the cavity with the surface preparation procedures shown to results in highest field performance. Finally a temperature mapping system using high sensitivity low temperature carbon resistors is attached on the outside to the sample end plate. Those thermometers are sufficient to measure nΩ surface resistance at fields as low as a few 10 mT.

1.3 Pits cavity as a tool for cavity quench and high field Q-slope studies

Pit-like structures on the niobium surface of srf cavities have been shown to cause thermal breakdown under certain conditions [12]. Thus we need to understand better how pits cause quench and what the relevant parameters are. This can be done experientially and by simulating pits.

However, the field at which quench is caused by a pit defect varies significantly from pit to pit, and frequently, pits do not cause quench up to the maximum field obtained. Previous thermal feedback models treat pits as normal conducting disks assuming the entire pit area is normal conducting starting from low field [12]. However, real pit-like defects observed in srf cavities have a complex 3-dimensional shape which can not be simply treated as a all normal conducting disk. Recent electromagnetic simulations show that the magnetic field enhancement (MFE) effect is present at the sharp edge or corner of a pit. It was calculated that a pit MFE factor β shows a $(r/R)^{-1/3}$ dependence, where r is the radius of the pit edge and R is the radius of the pit [41]. Therefore I developed a more accurate ring-type defect model in which only pit edges get normal conducting above a certain magnetic field level [13].

Previous experimental studies depended on random data sets collected from pits occasionally found on srf cavities. In order to systematically study the nature of pit-induced quench, I have prepared and tested a single-cell niobium srf cavity with many artificially drilled pits with different sizes. Thermometers attached outside the cavity pit locations recorded heating signals as function of the rf magnetic field level.

The experimental results from the pit cavity can be compared with the predictions from the new ring-type defect model [13] which can calculate the cavity outside heating signals based on different values of material parameters. The exact geometry features of pits were also obtained by surface replica techniques and analyzed by laser confocal microscopes. Moreover, since the pit edge areas experience very high magnetic field, those small regions provide valuable information about the high-field Q-slope.

1.4 Organization of the dissertation

The thesis is organized as follows:

Chapter 2 gives a brief introduction to srf cavities and presents superconductivity fundamentals.

Chapter 3 presents experimental setups and techniques used. The chapter has three parts. The first part is on the development of two TE-type sample host cavities systems, a pillbox and a mushroom type. It includes electromagnetic, mechanical and other design aspects of the cavities and the power couplers. The fabrication, surface treatment and the test insert development are also described in detail. The second part is about the design, fabrication and surface treatments of the special pits cavity. The third part is devoted to the cavity thermometry system for both TE cavities and and the pit cavity.

Chapter 4 presents the baseline experimental results of both the TE pillbox and mushroom cavity. Thermal feedback analysis and ways to further improve maximum fields on the sample surface will be explained in detail. I will discuss

the importance of the baseline results achieved.

Chapter 5 presents experimental results from the pit cavity. Optical inspection and laser confocal microscope analysis results are also presented.

Based on the results of chapter 5, chapter 6 will first present the new ring-type defect finite element thermal model, then compare the model predictions with experimental results. Insights on pits induced quench and high-field Q-slope will be discussed.

Finally, conclusions are summarized in chapter 7, and future work is discussed.

CHAPTER 2

SUPERCONDUCTING RF CAVITY FUNDAMENTALS

This chapter will introduce some basic concepts of microwave cavities. Then superconductivity and its dependence on srf cavity material properties will be discussed. Finally different cavity loss and quench mechanism will be introduced as well. These contents have been discussed in great details in Hasan Padamsee's two-volume book [1], [14].

2.1 Microwave cavity fundamentals

SRF cavities have resonating frequencies ranging from tens of MHz to several GHz. Based on the velocity of the particles that are accelerated, there are two types of cavities. One is for electrons that move at nearly the speed of light c and the other is for particles that move at a small fraction (e.g. $0.01 \sim 0.3$) of c. This thesis deals with the first kind of cavities.

The accelerating electric field E_{acc} is defined as an energy gain per unit length:

$$E_{acc} = \frac{V_{acc}}{d}, \tag{2.1}$$

where d is the cavity length and V_{acc} is the maximum energy gain possible during transit per charge.

In order to sustain the rf fields in the cavity, rf currents flow within a thin surface layer of the cavity walls. The non-zero dissipated power per unit area due to Joule heating is

$$\frac{dP_{diss}}{ds} = \frac{1}{2} R_s |\vec{H}|^2, \tag{2.2}$$

where $\vec{H}$ is the local magnetic field and R_s is the surface resistance.

The cavity intrinsic quality factor Q_0 is then defined as

$$Q_0 = \frac{\omega U}{P_{diss}} \tag{2.3}$$

where U is the stored electromagnetic energy in the cavity and ω is the resonating angular frequency.

Since the cavity stored energy U can be calculated by

$$U = \frac{1}{2}\mu_0 \int_v |\vec{H}|^2 dV, \tag{2.4}$$

the cavity quality factor can be obtained by

$$Q_0 = \frac{\omega_0 \mu_0 \int_v |\vec{H}|^2 dV}{R_s \int_s |\vec{H}|^2 ds} = \frac{G}{R_s}, \tag{2.5}$$

where

$$G = \frac{\omega_0 \mu_0 \int_v |\vec{H}|^2 dV}{\int_s |\vec{H}|^2 ds} \tag{2.6}$$

is called geometry factor which only depends on the cavity shape.

2.2 Radio frequency superconductivity fundamentals

2.2.1 Microwave surface resistance

Due to the inertial mass of the cooper pairs, a time-varying magnetic field in the penetration depth induces a time-varying electric field, which acts on the normal electrons and causes power dissipation proportional to the square of the rf frequency. Although the temperature dependence of rf surface resistance

was derived from the BCS theory [15] and is rather complex, involving different material parameters, a useful practical approximation for $T < T_c/2$ and for frequencies much smaller than 10^{12} Hz is [1]

$$R_s = R_{BCS} + R_0 = A\frac{1}{T}f^2 e^{\frac{-\Delta T}{kT}} + R_0, \tag{2.7}$$

where A is a constant, which depends on material parameters, Δ is the energy gap of the superconductor, f is the rf frequency and R_0 is the residual resistance which does not depend on the temperature. For niobium [1]

$$R_{BCS,Nb} = 2 \times 10^{-4}\frac{(f/GHz)^2}{1.5(T/K)}e^{\frac{-17.67}{T/K}} \tag{2.8}$$

Nb_3Sn is a strong type II superconductor. Below $T < 0.7T_c$, the BCS surface resistance of Nb_3Sn can be conveniently described by [1]

$$R_{BCS,Nb_3Sn} = 9.4 \times 10^{-5}\frac{(f/GHz)^2}{T/K}e^{\frac{-40.26}{T/K}} \tag{2.9}$$

Given the London penetration depth λ_L, intrinsic coherence length ξ_0, Fermi velocity, and the electron mean free path l, which characterize material purity, the BCS part of rf surface resistance can be calculated numerically.

2.2.2 RF Critical magnetic fields

Suggested by Ginzburg-Landau theory, there are two types of superconductors called type I and II based on the value of the so-called Ginsburg-Landau parameter. The G-L parameter is defined as

$$\kappa_{GL} = \frac{\lambda_L}{\xi_0} \tag{2.10}$$

where λ_L is the penetration depth and ξ_0 is the G-L coherent length. Type I superconductors exclude DC magnetic fields up to a lower critical field H_c, after which magnetic flux will penetrate the material and cause an abrupt transition to the normal conducting state. For type II superconductors, the surface energy of the normal-superconducting interface becomes negative when the applied magnetic field reaches the lower critical field H_{c1}. Above H_{c1} it is energetically favorable for flux to enter and the superconductor breaks up into finely divided superconducting and normal conducting regions (mixed state). The magnetic flux in the form of fluxoids will increase penetrating into the material until their normal conducting cores start to overlap, which happens at another higher field called upper critical field H_{c2} which is defined as [1]

$$H_{c2} = \frac{\Phi_0}{2\pi\mu_0\xi_0^2} \tag{2.11}$$

where $\Phi_0 = 2.07 \times 10^{-15}$ T-m^2 is the flux quantum.

A superheated superconducting state may persist metastably above H_c for type I and above H_{c1} for type II superconductors [1]. Ginzburg-Landau theory gives an approximate solution of the superheating field valid for $T_c - T \ll T_c$ as

$$H_{sh}(T) = c(0)H_c\left[1 - \left(\frac{T}{T_c}\right)^2\right], \tag{2.12}$$

where for niobium, the thermodynamic critical field $H_c = 2000$ Oe [1], and the critical temperature $T_c = 9.2$ K [1]. The constant $c(0)$ is the ratio of the superheating field and the thermodynamic critical field at zero temperature. For very high purity niobium, $c(0) \approx 1.2$ [1].

Recently Eilenberger equations have been solved for the temperature dependence of the superheating field of different materials [3].

2.3 Cavity loss and quench mechanisms

2.3.1 Field dependence of the RF surface resistance

The performance of a srf cavity is typically evaluated by measuring the cavity intrinsic quality factor Q_0 as a function of the accelerating field E_{acc} or maximum surface magnetic field H_{max} as used in this thesis. The Q_0 vs E_{acc} curve usually shows characteristic field dependence and is divided into three regions as shown in Fig. 2.1: low-field Q-slope, medium-field Q-slope and high-field Q-slope due to different loss mechanisms.

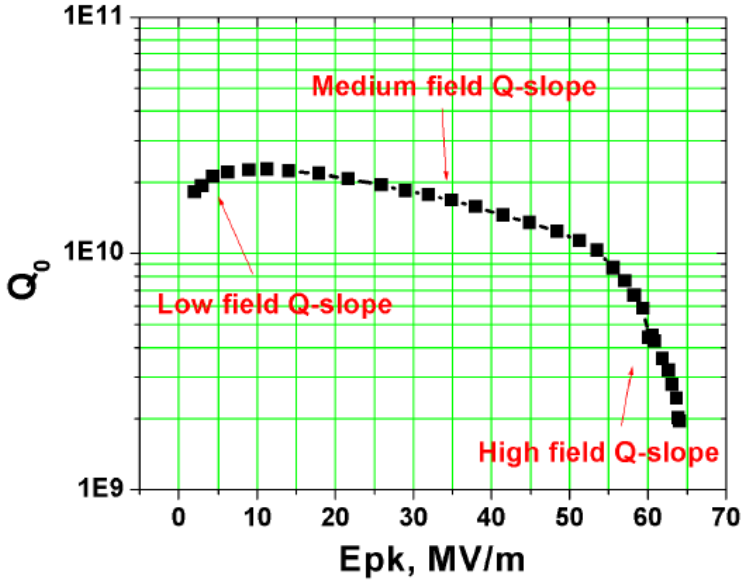

Figure 2.1: Typical Q_0 vs. peak electric surface field E_{pk} curve of a srf niobium cavities shows three regions of Q-slope. [20]

Low-field Q-slope is a decrease in the cavity surface resistance with field in the range of E_{acc} below approximately 5 MV/m. Since it is un-relevant in most srf cavity applications, it is poorly understood. Some experiments suggest that

the low-field Q-slope may originate from the metal-oxide layer [21].

Medium-field Q-slope is a mild decrease of the cavity quality factor with field until a quench or a high field Q-slope happens. There is a strong theoretical indication that the medium-field Q-slope may be due to a fundamental field dependence of the BCS surface resistance amplified by a thermal feedback process [22].

The high-field Q-slope arises when $H_{max} \geq 80$ mT in the absence of parasitic losses such as multipacting, field emission or hydrides. It is the sharp increase in the surface resistance of niobium with increased surface magnetic field. An empirical method of in-situ baking the cavity at 100 ~ 120 °C in ultra high vacuum for 12 ~ 48 hours depending on the grain size generally reduces the high-field Q-slope, specifically for cavities treated by electro-polishing [14]. Various theoretical models of high-field Q-slope such as thermal feedback [14], surface roughness induced field enhancement at grain boundary edges [23], oxygen pollution layer [24], trapped flux [25] and most recently hydrogen presence [26] have been proposed.

2.3.2 quench mechanisms

The maximum field achieved by srf cavities is limited by the thermal breakdown initiated from so-called defect areas in the high magnetic field region around the equatorial welding zone. Optical inspection techniques found that many of these defect regions can be categorized as pit-like structures. Although most of the pits found did not cause quench at the magnetic field achieved, some of them are responsible for initiating quench. This indicates that sizes, depth and

edge sharpness of the pits may determine the quench onset field.

The maximum surface field achieved by srf cavities often is found to be limited to values well below the maximum theoretical limit set by the critical magnetic field of the superconductor [1]. T-maps show that thermal breakdown is initiated by small defect areas and the cavity quench typically is thermal breakdown [26]. Optical inspection results sometimes show visible defect at quench locations, but not always [14]. One type of visible defect are pits. However, many pits also do not cause quench. There are also other sources of quench including normal conducting inclusions, weld defects and others as discussed before [1]. Pits and pits physics will be discussed in chapter 5 and 6.

CHAPTER 3

EXPERIMENTAL SETUP AND TECHNIQUE

3.1 Introduction

In this chapter, the design, fabrication, assembly, preparation and rf test principles of two TE-type sample host cavities and the pits cavity will be discussed in details. Also, the design and fabrication of the input coupler for the TE cavities will be presented. The design and construction of a dedicated rf test insert and thermometry system are also described. Different surface treatments for the cavities are discussed as well.

3.2 TE-type sample host cavity designs

Various versions of TE pillbox cavities have been used at Cornell University in the past to study surface resistance of high temperature superconductors like $YBa_2Cu_3O_7$, ultra-high vacuum cathodic arc films coated samples and MgB_2. For the first TE pillbox cavity, the sample was introduced into the cavity by a sapphire rod through a niobium cutoff tube aligned along the cavity axis [27]. A thermometer was attached to the sapphire rod near the sample and a heater was attached to the bottom of the sapphire rod. This cavity was used to measure rf surface resistance of $YBa_2Cu_3O_7$ at various temperatures with low magnetic field on the sample. The highest magnetic field reached on the sample surface was around 11 Oe [27]. Later the bottom plate of the cavity was replaced by a Nb/Cu end plate with a groove on the surface of the sample which was intended

for removing the degeneracy between TE_{011} and TM_{110} modes [7]. This cavity had a very high residual resistance above 1 $\mu\Omega$ and the maximum surface field achieved was around 300 Oe. Therefore, I designed two new TE type cavities to enable testing flat surface samples and with the aim of of reaching high surface magnetic field by using carefully treatments and improved rf designs.

3.2.1 General considerations of TE-type sample host cavities

For a cylindrical cavity with length d, the resonant frequency of a mode is given by [1]

$$f_{mnl} = \frac{c}{2\pi}\sqrt{(\frac{x_{mn}}{a})^2 + (\frac{l\pi}{d})^2}. \tag{3.1}$$

Here the integer m,n and l are measures of the number of sign changes E_z undergoes in the angular ϕ, radial ρ and longitudinal z directions. a is the radius of the cavity and c is the speed of light. For transverse magnetic (TM) modes, $x_{mn} = p_{mn}$, where p_{mn} is the nth root of Bessel function $J_m(x)$. For transverse electric (TE) modes, $x_{mn} = p'_{mn}$, where p'_{mn} is the nth root of the derivative of $J_m(x)$ with x.

Since $p_{11} = p'_{01} = 3.832$, the frequency of TM_{110} modes is the same as the frequency of TE_{011} modes in pillbox cavities. The electrical and magnetic field distribution of those two modes are shown in Fig. 3.1. Therefore, one of the main tasks of the design of TE-type sample host cavities is to separate those two degenerate modes. In the past, grooves were introduced on the sample plate to break the mode degeneracy. However, such grooves make the shape of the sample plate more complex and flat sample plates can not be tested.

TE_{0nl} modes are chosen as the operating modes in endplate replacing sample

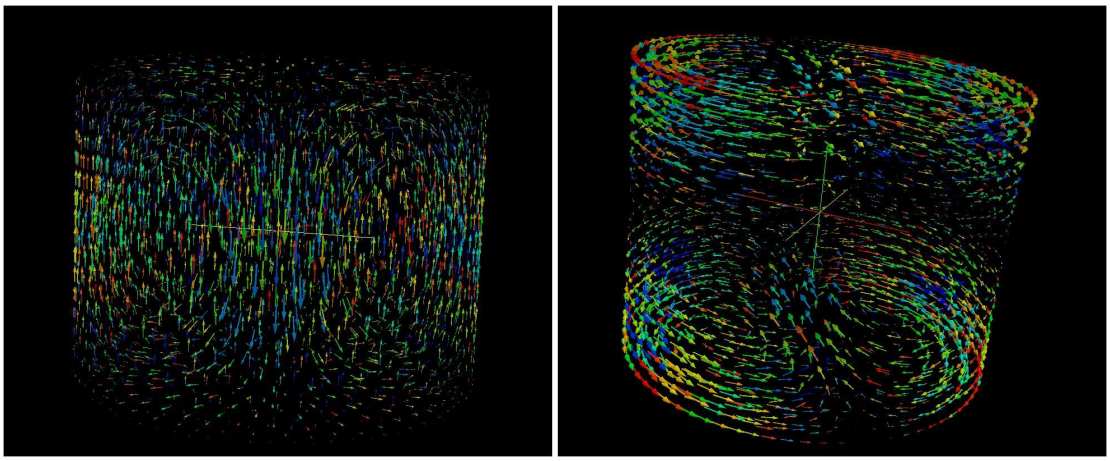

Figure 3.1: Magnetic field distribution of TE_{011} (left) and TM_{110} (right) modes inside a TE pillbox cavity.

host cavities for the following reasons:

- The TE_{0nl} monopole modes have no electric field lines terminating on any cavity surfaces so that electron multipacting and field emissions are absent theoretically.
- The currents in the sample plate and the host cavity flow azimuthally and theoretically should not create any losses in the joint for a sufficiently small joint;

The first reason listed above strictly does apply to a perfect pillbox shaped cavity. Normally a power coupling port and a rf signal pickup port are placed on the top of the host cavity, and this will deform the magnetic field line distributions. Thus there will be a chance that multipacting may happen somewhere in the host cavity coupling port or the sample surface.

The second reason listed above strictly does only apply to a perfect pillbox shaped cavity which assumes there is no gap between the host cavity and the

sample plate. However, indium wires with diameters ranging from 0.5~1.5 mm are used to seal the host cavity and the sample plate. The thickness of indium wires can not be pressed to zero and thus there is always a certain gap between the TE cavity flange and the sample plate. The electromagnetic field will decay exponentially into the gap. The maximum field at the location of the indium wire will determine the rf losses at the cavity joints and how far away from the cavity inner surface the wire need to be placed.

To investigate how the gap due to the indium sealing wire will affect the cavity performance, a numerical model was set up as shown in Fig. 3.2.

Assuming two different indium seal gap heights of d 0.5 mm and 1 mm, the decrease in cavity quality factor Q_0 due to penetrating field causing rf losses at the indium joint is shown as Fig. 3.3. It shows that when the indium seal is >2 mm outside from the cavity inner wall surface, the further from the cavity, the influence of the indium joint loss on the cavity Q_0 is negligible. In reality, the height of the indium gap h is even smaller than 0.5 mm, and the indium joint loss is nearly zero. This calculation guides us how to design the sealing flanges between the host cavity and the sample plate. The flange width is made larger than 10 mm so that during the cavity assembly process, the indium wire is placed at least 5 mm far from the host cavity inner surface.

3.2.2 New TE pillbox cavity electromagnetic design

As discussed above, grooves were introduced to the bottom sample plate to break the mode degeneracy between TE_{011} and TM_{110} modes in previous TE pillbox cavity designs. However, the grooves will cause unwanted local mag-

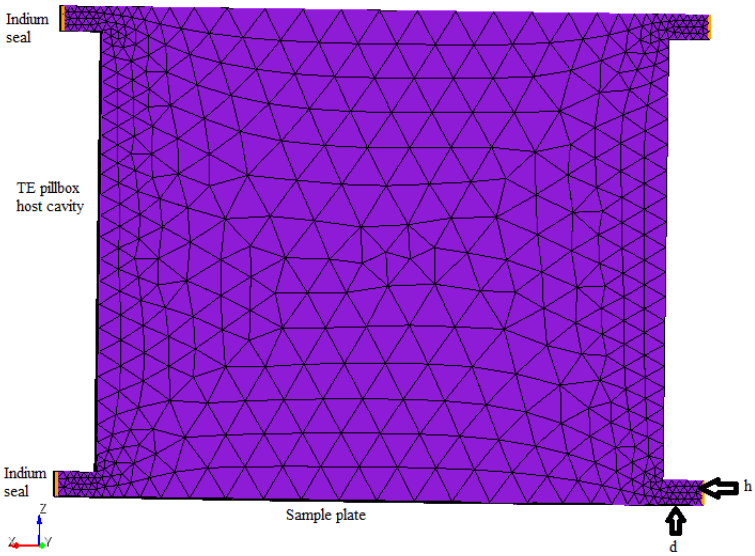

Figure 3.2: A meshed model of a TE pillbox cavity with indium seal gap. Here d is the distance between indium seal and cavity inner wall, h is the height of compressed indium seal which typically is 0.5~1 mm.

netic field enhancement and thus the design of such grooves needs to be done carefully to minimize the undesirable effect. Fig. 3.4 shows different grooves added to either the bottom sample plate or the top plate.

The traditional way of measuring the cavity is by phase locking the transmitted power signal (cavity field probe signal) from the excited cavity. Therefore both an input power coupling port and a pickup power port are needed. The left of Fig. 3.4 shows two coupling ports added to the top plate. In order to keep the bottom sample flat, the grooves are separated and moved to the top plate with the coupling ports as shown in the right of Fig. 3.4. However, this comes at the cost of making the top plate complex, difficult to fabricate, and does not leave room for a larger, more robust rf input coupler. A better solution is using the reflected power instead of the transmitted power signal for phase locking,

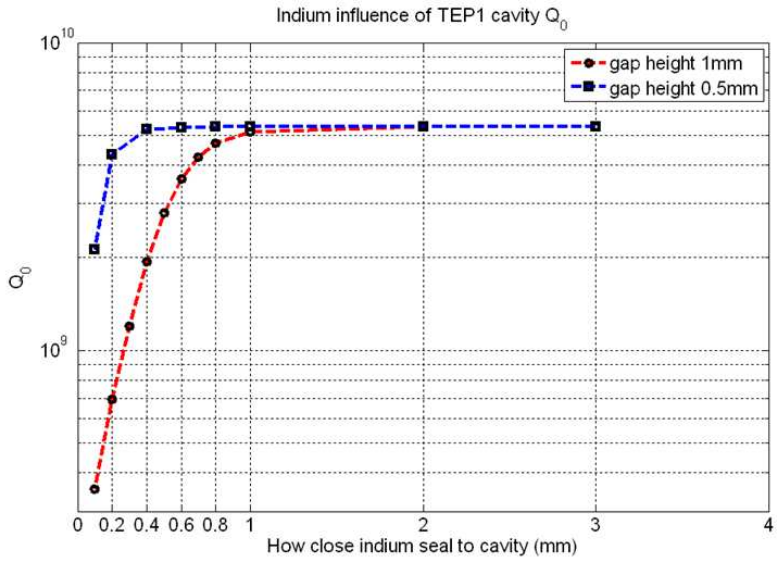

Figure 3.3: The TE pillbox cavity quality factor Q_0 versus the distance d from indium seal to the cavity inner wall for two different indium seal heights d of 0.5 mm and 1.0 mm at 2 K and 6 GHz. Indium wire is assumed to be normal conducting.

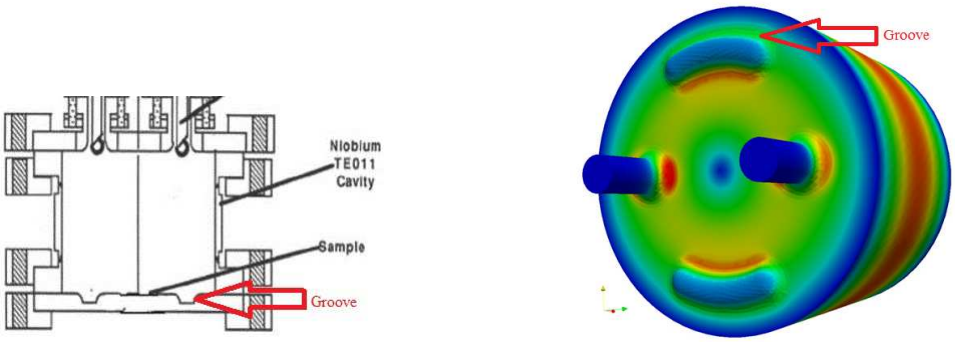

(a) A circular groove on the bottom sample place (b) Two separate grooves on the top plate.

Figure 3.4: Different mode shifting grooves introduced to TE pillbox cavities.

thus avoiding the need for the second pickup power port.

By increasing the diameter of the input power coupling port and moving it to the center of the cavity, the port itself is sufficient to break the mode degeneracy between TE_{011} and TM_{110} modes. The fabrication process is greatly simplified

by not requiring dies to make grooves. Fig. 3.5 shows the magnetic field contour plot in a cross-section view of the new design. The design parameters of this TE pillbox are shown in Tab. 3.1. This TE pillbox cavity consists of three separate niobium parts: the top plate with coupler port, the cavity tube and the flat sample plate (baseline niobium). The three parts are assembled together by two indium seals using non-magnetic standard steel type 316 clamps. The highest surface magnetic field is located at the middle of cavity wall as shown in Fig. 3.5.

The field ratio R, defined as

$$R = \frac{H_{max,sample}}{H_{max,cavity}} \tag{3.2}$$

for TE pillbox cavity is about 0.77. We have chosen the frequency near 6 GHz to keep sample size reasonably small.

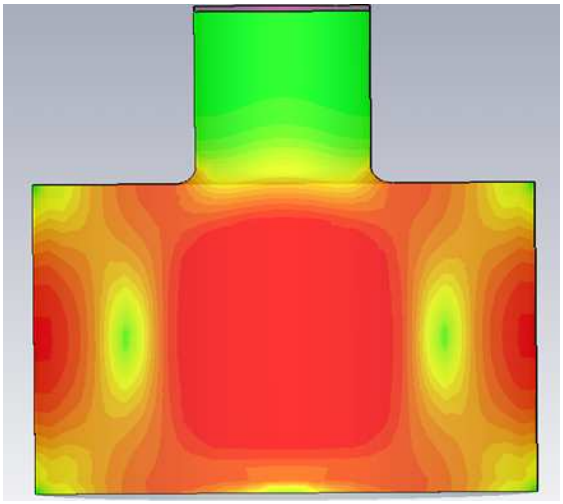

Figure 3.5: Magnetic field contour plot of the TE_{011} mode of new TE pillbox cavity. Red color indicates higher magnetic field region.

Table 3.1: The design parameters of the new TE pillbox cavity

	Big flat sample plate
frequency of TE_{011} (GHz)	5.88
frequency of TM_{110} (GHz)	5.68
$\frac{H_{max,sample}}{H_{max,cavity}}$	0.77
sample diameter (cm)	7.0

3.2.3 TE mushroom cavity electromagnetic design

The field ratio *R* is still lower than 1 for this new TE pillbox cavity, which means that not the sample plate but the host cavity will reach the maximum magnetic field first. In order to fully characterize the RF performance of Nb_3Sn and MgB_2, it is essential to achieve surface magnetic fields on material samples above 2000 Oe. The maximum magnetic field that can be achieved on the sample is limited by the breakdown magnetic field of the host cavity. Thus only a new host niobium TE cavity with an optimized shape having a field ratio R > 1 can achieve magnetic fields on the sample above the RF critical field of niobium.

Therefore, the main design goal is to maximize the ratio *R* of maximum sample plate surface magnetic field to maximum host cavity surface magnetic field. Other design constraints of such an improved shape TE host cavity are:

- The sample size (bottom plate of the cavity) should be small (< 10 cm, i.e. 4 inches diameter).
- Lower operating modes frequencies (3 ~ 6 GHz) are desirable to avoid global thermal instability.
- The cavity configuration should be relatively simple and the bottom sam-

ple plate should be easy to attach.

We started from several possible basic shapes that were evolved from the pill-box shape. Each shape can be defined by a parameter set $(a_1, a_2, ..., a_n)$. For example, Fig. 3.6 shows a half cell shape for a sample host cavity. We employ the construction of the half cell profile line as two elliptic arcs with half-axes a_3, a_4, a_5 and a_6, separated by a straight segment of length l which is tangential to both arcs and also is determined by a_8. The parameter a_7 and a_9 determine the input power coupling port.

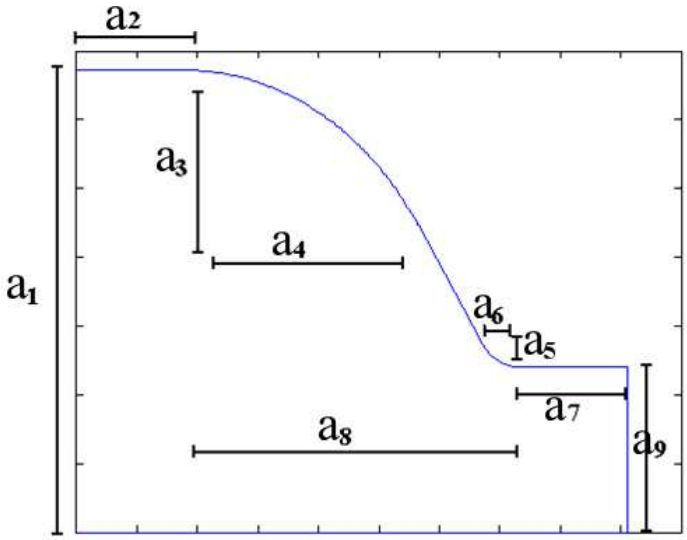

Figure 3.6: A basic half cell shape for a sample host cavity represented by a parameter set $(a_1, a_2, ..., a_9)$. a_1 is the sample plate radius.

Fig. 3.7 shows four basic shapes from which the optimization began. They all share two elliptic arcs joined by a tangential line. The differences are the connection to the sample plate and to the coupling port.

Matlab scripts were used to generate geometry input files used by CLANS/SLANS [17] for a given parameter set. A modified version of CLANS was

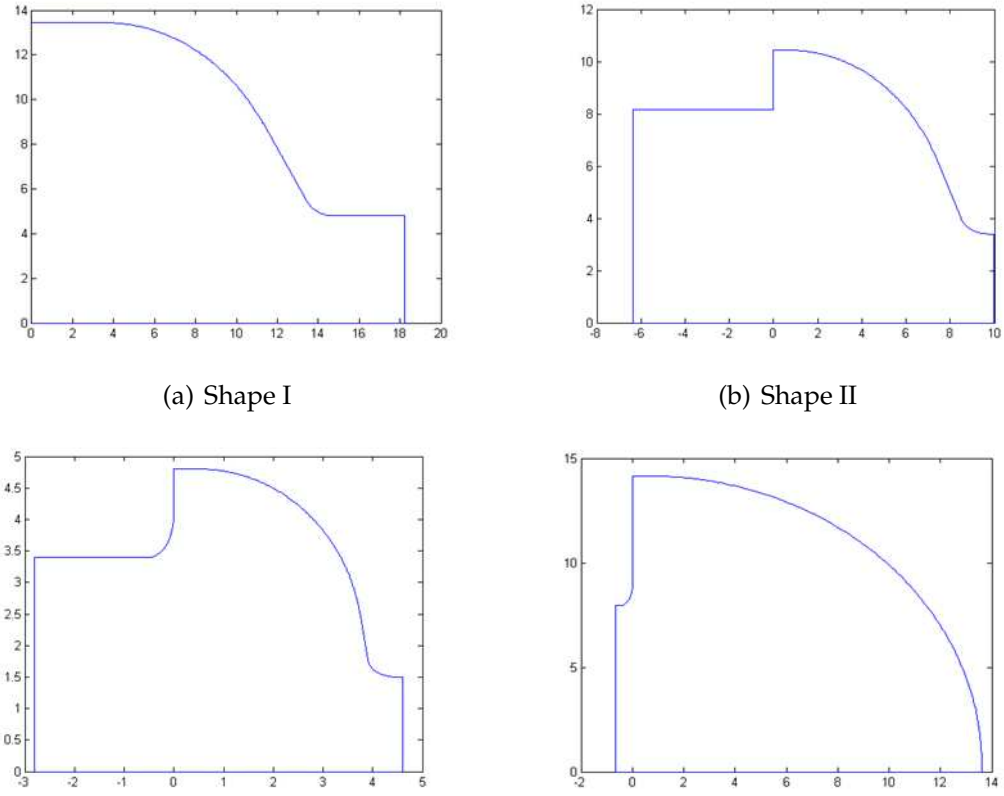

(a) Shape I

(b) Shape II

(c) Shape III

(d) Shape IV

Figure 3.7: Four basic shapes of TE sample host cavities.

used to calculate EM eigenmodes and generated a file containing surface magnetic fields of calculated modes for each geometry. Then the surface field ratios R were calculated from the surface fields. Each parameter in the parameter set was modified by a centain step size and the ratio R was obtained for each variation. The iteration process was repeated until the best ratio was found. Since this optimization method was basically a gradient ascent search algorithm, the previous best result was re-optimized by the MATLAB optimizer Fminsearch [18] which uses the simplex search method. Fig. 3.8 describes this method of cavity design.

Three host cavity shapes have been obtained as shown in Fig. 3.9, 3.10 and

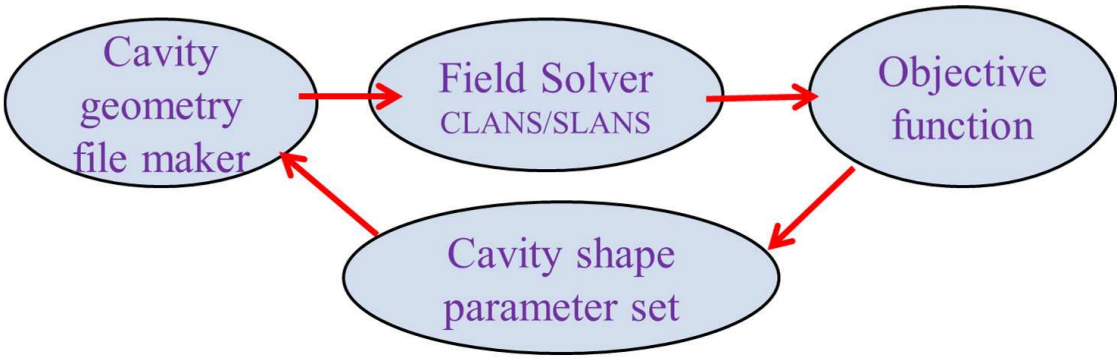

Figure 3.8: The design process of TE sample host cavities.

Table 3.2: The design parameters of three types of TE sample cavity

	Design A: TE_{011} mode	Design B: TE_{012} and TE_{013} mode	Design C: TE dipole mode
$R = \frac{H_{max,sample}}{H_{max,cavity}}$	1.40	1.25(TE_{012}) 1.56(TE_{013})	3.25
f (GHz)	5.02	4.78(TE_{012}) 6.16(TE_{013})	4.01
Sample diameter (cm)	10	10	10

3.11. Two of them are excited in TE_{01x} monopole modes as stated before. In a third design a dipole TE mode is explored because of its attractive high sample to cavity surface magnetic field ratio R. The design parameters of the three optimized shapes are summarized in Tab. 3.2. Note that the size of the sample plate can be readily scaled inversely proportional to the host cavity operating frequency.

Fig. 3.9(a) shows the magnetic field line distribution for the first type (Design A) of a TE cavity excited in TE_{011} mode. The cavity is of slightly reentrant

shape. The surface magnetic field along the entire cavity wall and sample plate is displayed in Fig. 3.9(b). The surface field ratio R is 1.4 which indicates that 2800Oe can be reached theoretically on material samples assuming a niobium superheating field of 2000 Oe.

In design B, the cavity is operating in the two modes TE_{012} and TE_{013}. The novel feature of this cavity design is that it allows to test material samples under two different frequencies. The maximum of the surface magnetic field on the sample plate is at the same location for both modes as seen in Fig. 3.10(c). This beneficial feature enables us to determine the frequency dependence of the rf performance of sample materials without changing the host cavity. Fig. 3.10(a) and Fig. 3.10(b) show the magnetic field lines distribution for both the TE_{012} mode and the TE_{013} mode. The surface field ratio R for the TE_{012} mode is 1.24 which suggests that surface magnetic field on material samples theoretically reach up to 2480 Oe. The surface magnetic field on material samples can theoretically even reach up to 3140 Oe for the TE_{013} mode with a field ratio R = 1.57, again assuming a superheating field of 2000 Oe for the niobium host cavity.

Design C, i.e., the TE dipole mode host niobium cavity design, has the highest surface field ratio of R = 3.25 which means that the surface magnetic field on sample plates can reach 6500 Oe theoretically. The maximum of the surface magnetic field is located at the center of the sample plate as shown in Fig. 3.11(b). Fig. 3.11(a) shows the surface electric and magnetic field distribution at the sample plate. Due to the presence of surface electric fields, carefully cleaning and preparation of the host cavity would be essential to avoid possible multipacting and field emission in this design.

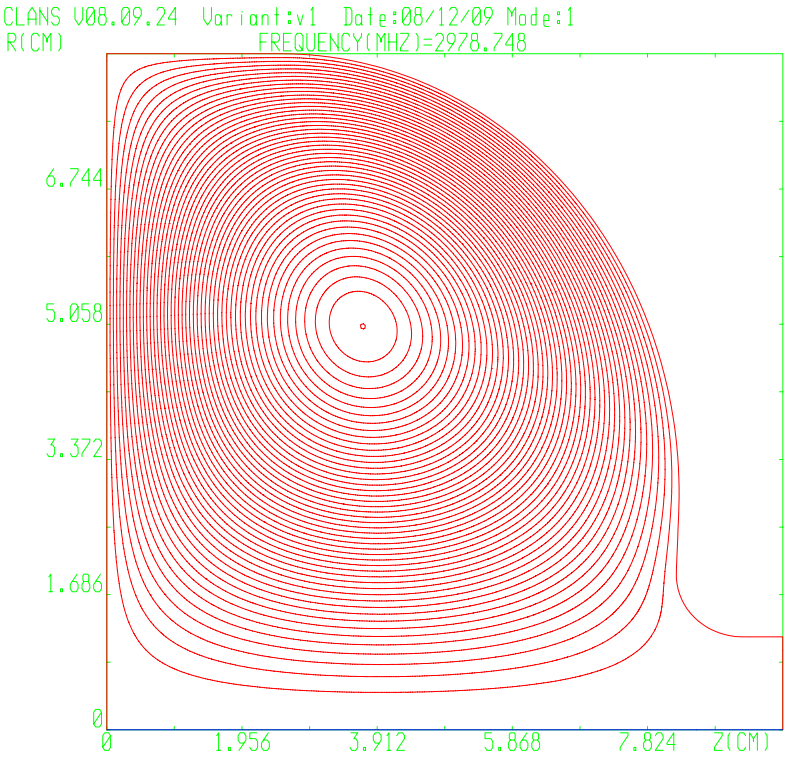

(a)

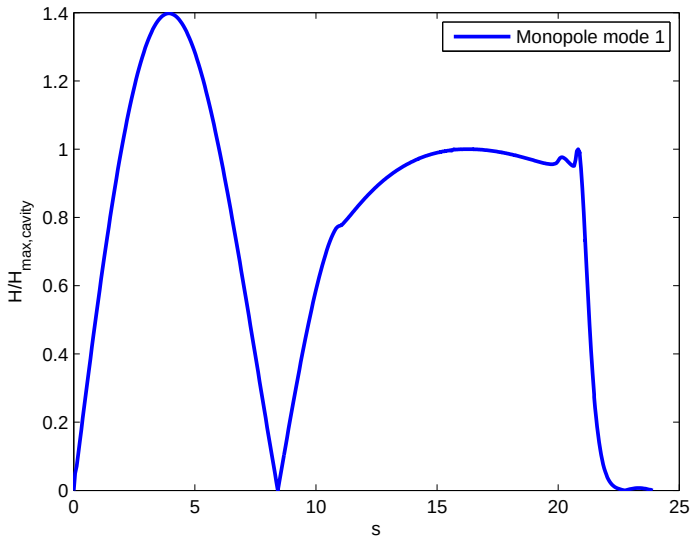

(b)

Figure 3.9: Magnetic field lines distribution (a) and normalized surface magnetic field distribution (b) of design A along the sample plate (s=0 to 5 cm) and walls of the host cavity (s=5 to 14 cm).

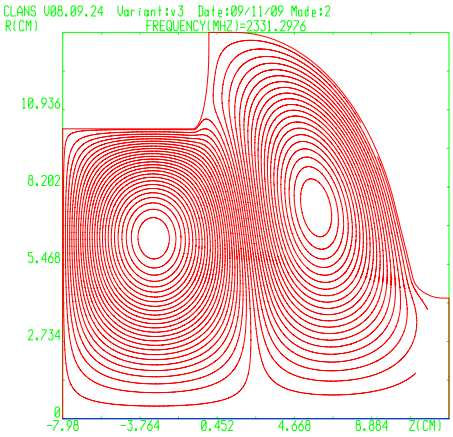

(a)

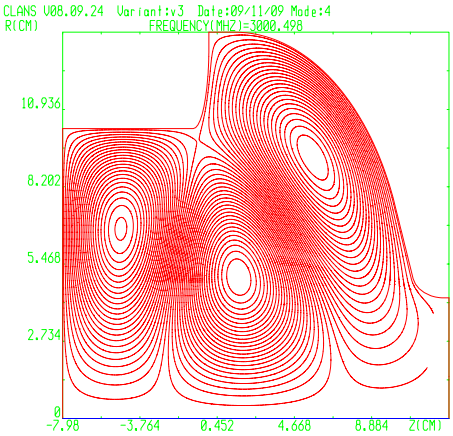

(b)

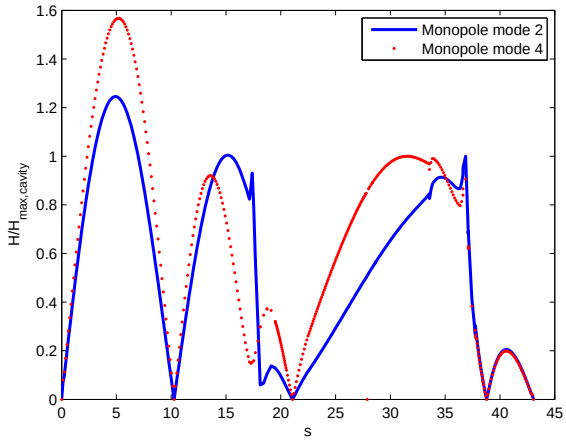

(c)

Figure 3.10: Magnetic field lines distribution for a TE_{012} mode (a) and a TE_{013} mode (b) in cavity design B. (c) is the normalized surface magnetic field along the sample plate (s=0 to 5 cm) and walls of the host cavity (s=5 to 21 cm).

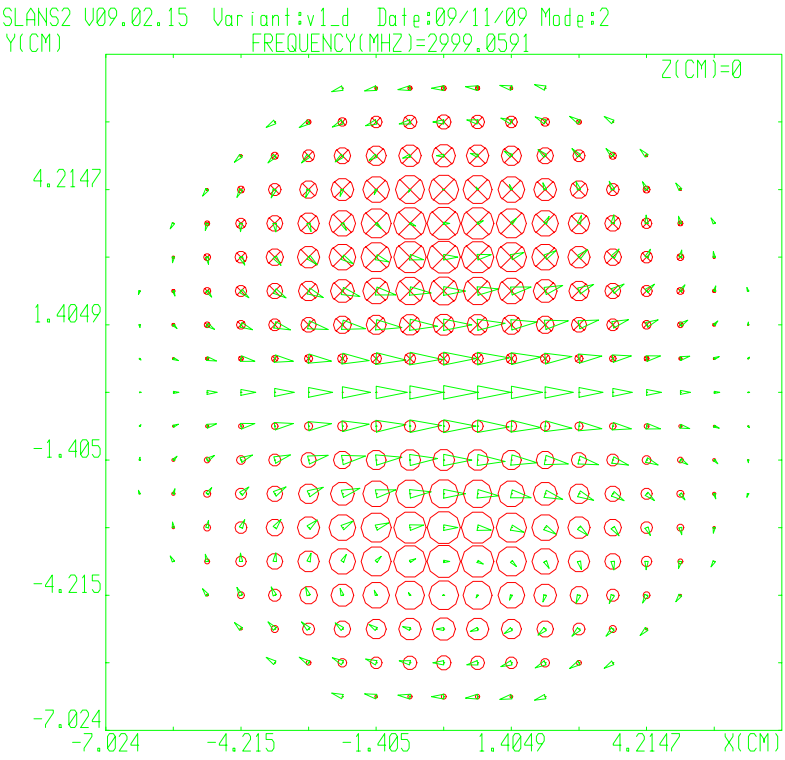

(a)

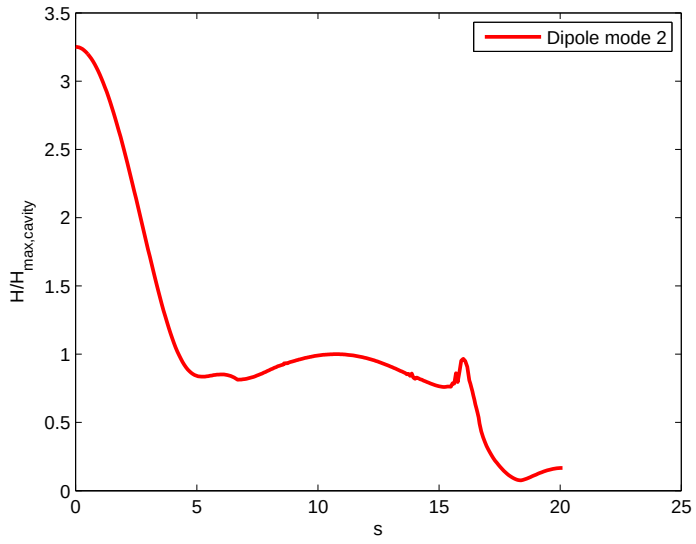

(b)

Figure 3.11: Surface magnetic (green) and electric (red) field distribution (a) on the sample plate for a TE dipole mode design C. (b) is the normalized surface magnetic field along the sample plate (s=0 to 5 cm) and walls of the host cavity (s=5 to 15 cm).

Since surface magnetic fields at the edge of the sample plate for the TE monopole mode in design A and B go to zero, as shown in Fig. 3.9(b) and 3.10(c), there should not be any loss at the joints ideally. In the presence of finite size joints, our calculations show that small surface magnetic fields leaking into the joint region outside the sample plates decay exponentially in the radial direction. Therefore very low loss joints between host cavities and sample plates can be achieved for the TE monopole mode in cavity designs A and B. However, the seal problem is pronounced for the TE dipole mode design C because the surface magnetic field at the edge of the sample plate does not go to zero as shown in Fig. 3.11(a). Thus a choke joint would need to be designed to decrease the surface magnetic field at the joint and to enable low loss at the indium seal.

3.2.4 TE sample cavities mechanical stability analysis

In order to study the deformation of the host cavity and sample plate when the cavity is under vacuum and the outside at atmosphere pressure, stress analysis was performed using ANSYS [19] for all three types of TE sample host cavities. The most serious deformation is located at the center of the sample plate for every design. Figure. 3.12 shows deformation calculations under 1 atm outside pressure. The scaling law is that the maximum deformation is approximately proportional to the diameter of sample plates. The largest deformation is about 0.15 mm for a 10 cm diameter niobium sample plate of 3 mm thickness, which is still acceptable. Sample plates with diameters above 15 cm become unfeasible because of the high stress and strains if the cavity is evacuated.

Due to the small size, the new TE pillbox cavity does not show significant

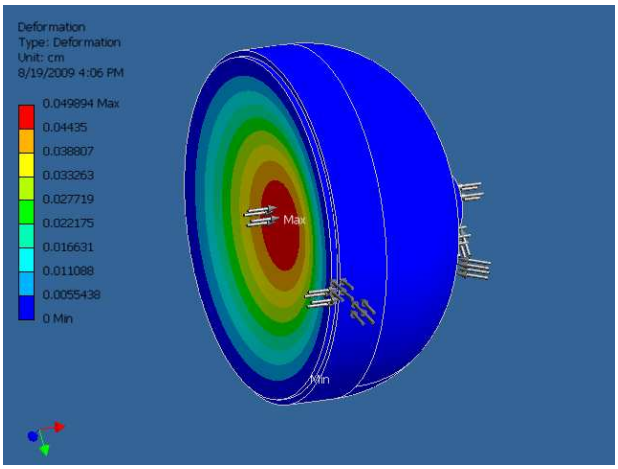

(a) Design A

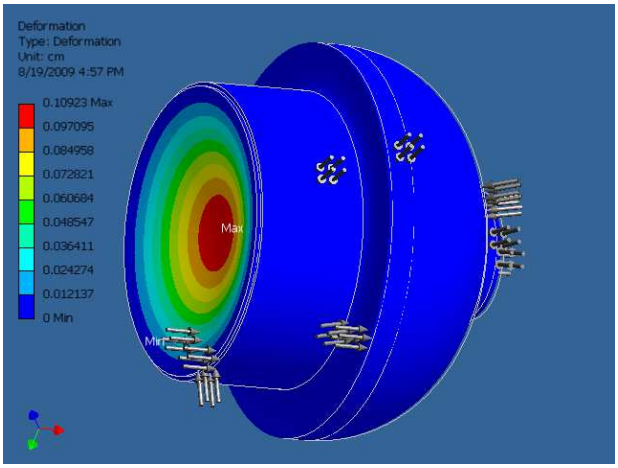

(b) Design B

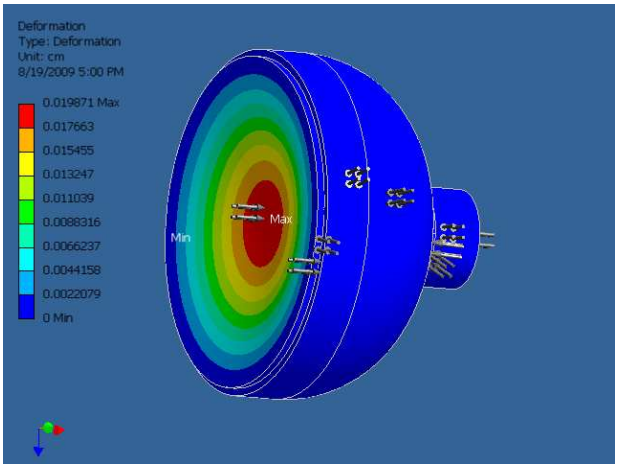

(c) Design C

Figure 3.12: Deformation calculations for the case that the host cavites are under vacuum and the outside is at atmosphere pressure, assuming a 3 mm thickness niobium plate.

deformation under vacuum.

3.3 Coupler design

Out of the three optimized versions of an improved TE sample host cavity, design B was chosen to be fabricated for the following reasons: it enables dual mode operation to study frequency dependence of the surface resistance, ideally has no surface electric fields and no joint losses, and has a high ratio of sample magnetic field to the host cavity surface magnetic field. In the following, design B is referred to as the TE mushroom cavity because of its shape. The input coupler port is located at the center top of the mushroom type cavity and the pickup probe and pumping ports are distributed symmetrically along the input coupler port. Fig. 3.13 shows the TE mushroom cavity with both coupler ports and the pumping port.

In the following sections, the rf design of the input coupler, coupler heating considerations, and 3-dimensional multipacting simulations to both operating modes using SLAC A3P codes [38] will be described.

3.3.1 Input coupler electromagnetic design

The rf input coupler to the TE_{012} and TE_{013} modes of the TE mushroom cavity needs to effectively couple to both operating modes. As we can see from a typical "Saclay" style input coupler as shown Fig. 3.14, the coupler tip plane is always aligned with the magnetic field line plane of the TE_{0mn} monopole modes no matter what direction the tip is positioned, if the loop/hook is at the cavity

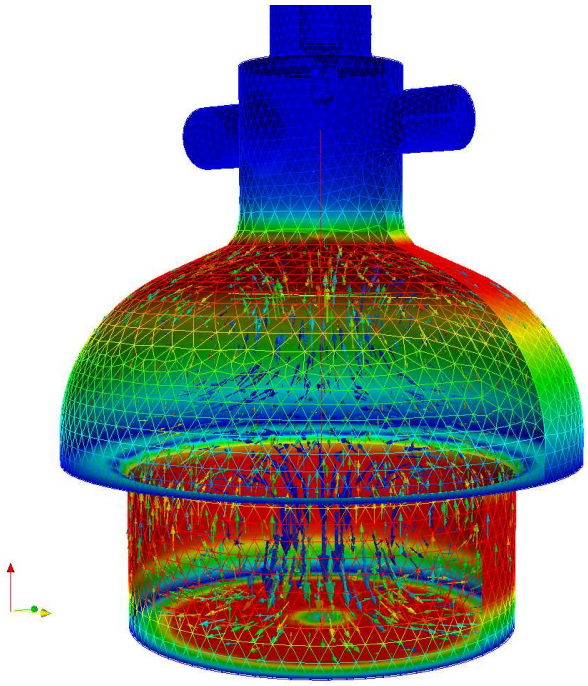

(a) Spacial magnetic field distribution of the TE_{012} mode. Red indicates high surface magnetic field. The maximum magnetic field on the sample plate is 1.24 times higher than on host cavity wall

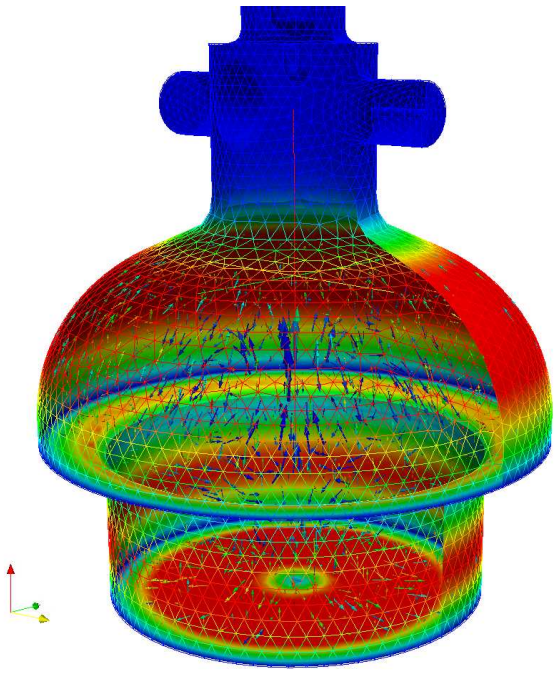

(b) Spacial magnetic field distribution of the TE_{013} mode. Red indicates high surface magnetic field. The maximum magnetic field on the sample plate is 1.57 times higher than on host cavity wall

Figure 3.13: Magnetic field distribution in the TE mushroom cavity.

axis. Therefore, an off-center loop has to be used as shown in Fig. 3.15 to achieve sufficient coupling to the TE cavity modes.

The strength of coupling depends both on the tip penetration depth and the angle of the direction of the hook. The external quality factor is used to characterize the coupling between the rf input coupler and the cavity as

$$Q_{ext} = \frac{\omega U}{P_e}, \tag{3.3}$$

where U is the cavity stored energy and P_e is the power leaking back out the rf input coupler when the rf drive is off [1].

The external quality factor Q_{ext} of the input coupler was calculated by both *Omega3P* [38] and *MWS* [28] and agreed well. Since rf surface resistance of new superconducting materials may vary a lot, matched coupling should be achieved for a large range in cavity intrinsic Q_0 so that power can be transferred efficiently to the cavity. Thus the coupler is designed to enable a large range of coupling variation from 10^7 to 10^{10}. The Q_{ext} dependence on hook tip penetration depth is shown in Fig. 3.16.

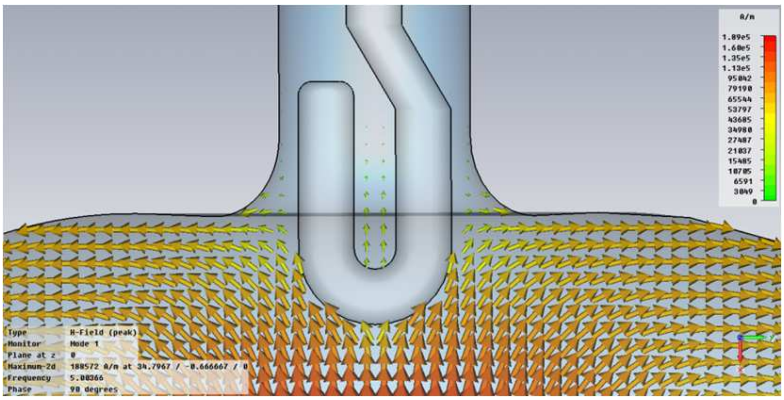

Figure 3.14: Magnetic field distribution near a "Saclay" style loop coupler calculated by MWS.

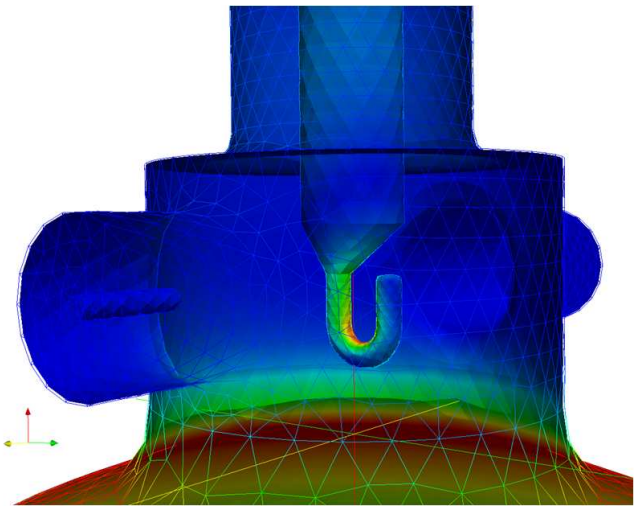

Figure 3.15: Magnetic field distribution near an off-center hook coupler calculated by Omega3P.

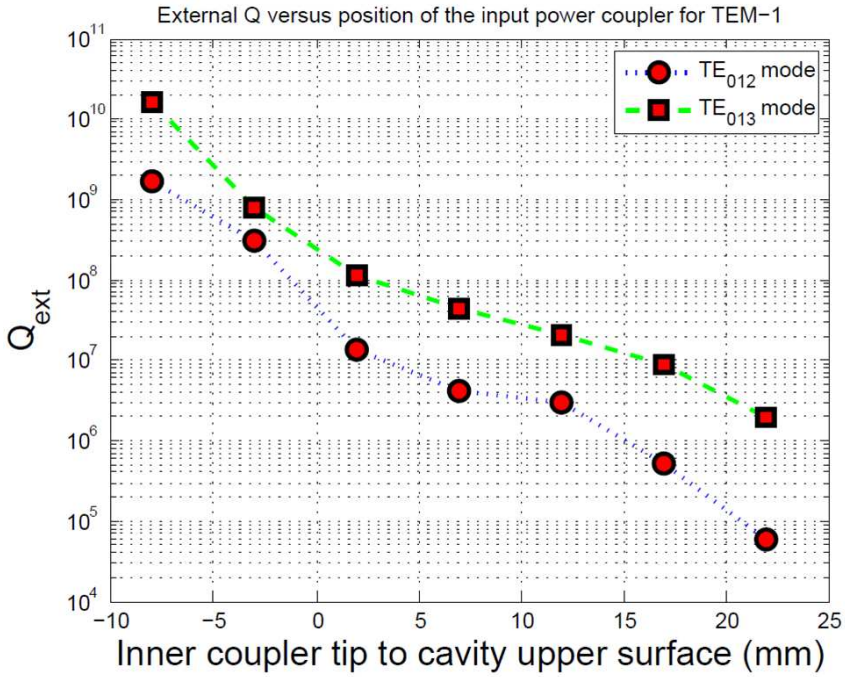

Figure 3.16: Q_{ext} dependence on coupler penetration depth into the cavity.

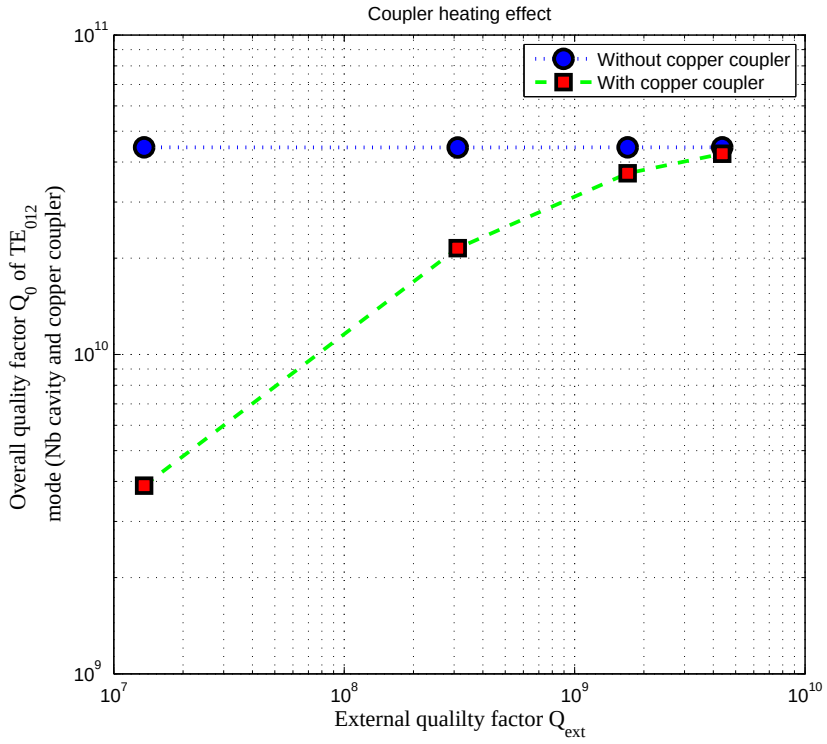

Figure 3.17: Host cavity Q_0 degradation due to coupler penetration.

The Q_{ext} simulations results show that enough coupling range is achieved for both operating modes for a coupler movement about 25 mm. As the input coupler tip penetrates into the cavity, the superconducting host cavity quality factor Q_0 may be degraded due to the rf losses at the normal conducting coupler inner conductor, which is made of copper. Fig. 3.17 shows that the input coupler does not significantly reduce the cavity Q as long as Q_{ext} is kept above 10% of the intrinsic quality factor Q_0 of the cavity.

3.3.2 Input coupler multipacting analysis

Multipacting (MP) is a resonant electron discharge inside rf structures, produced by the synchronization of emitted electrons with the rf fields and by the electron multiplication at the impact point at the surface of the structure. The current of re-emitted electrons will grow rapidly through secondary electrons when the secondary electron yield (SEY) (ratio of secondary electrons over impact electrons) for the primary electron impact energy is greater than one.

Ideally TE_{0mn} monopole modes do not have surface electric field on the host cavity walls. Therefore there should be no multipacting. However due to the presence of the off-center hook coupler, there may be some non-zero electric field presents in coupler port area and sample plate that is likely to induce multipacting. Therefore a fully 3-dimensional multipacting simulation was performed to check the possible existence of multipacting barriers. Numerical simulation using *SLAC*'s parallel computing EM codes ACE3P were performed [38]. First, the electromagnetic field inside the cavity with full length input coupler port and side ports was calculated using Omega3P with high order tetrahedra mesh elements. The magnetic field distribution of the TE_{012} mode inside the host cavity is shown in Fig. 3.18.

The precise surface field extracted from Omega3P was then used in Track3P [38] to search for resonant electron trajectories. Electrons were launched from specific surfaces at different phases over a full rf period. The initial launched electrons are accelerated by the electromagnetic fields in the structure and eventually hit the boundary, where secondary electrons are emitted, depending on the impact energy of the primary electrons. In the simulation, it is assumed that the particles just bounces back at the surface and the trajectories continue to be

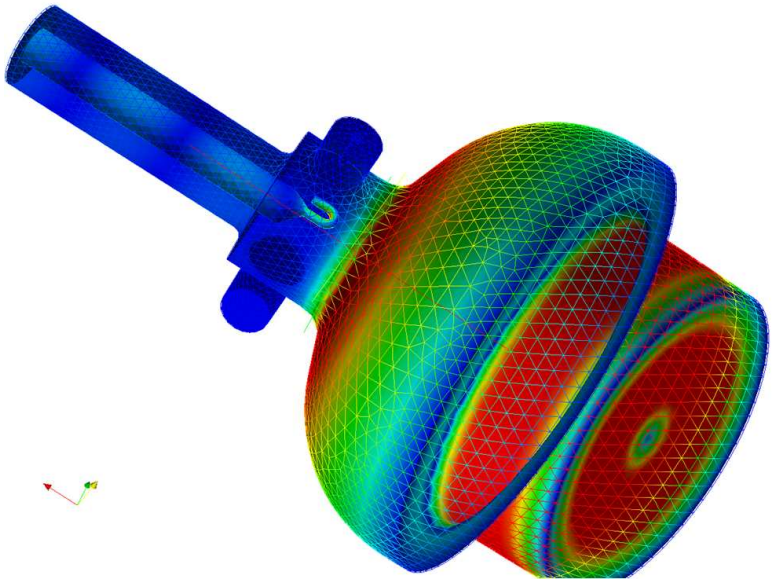

Figure 3.18: TE_{012} magnetic field distribution of the TE mushroom cavity with full length input coupler port calculated by Omega3P.

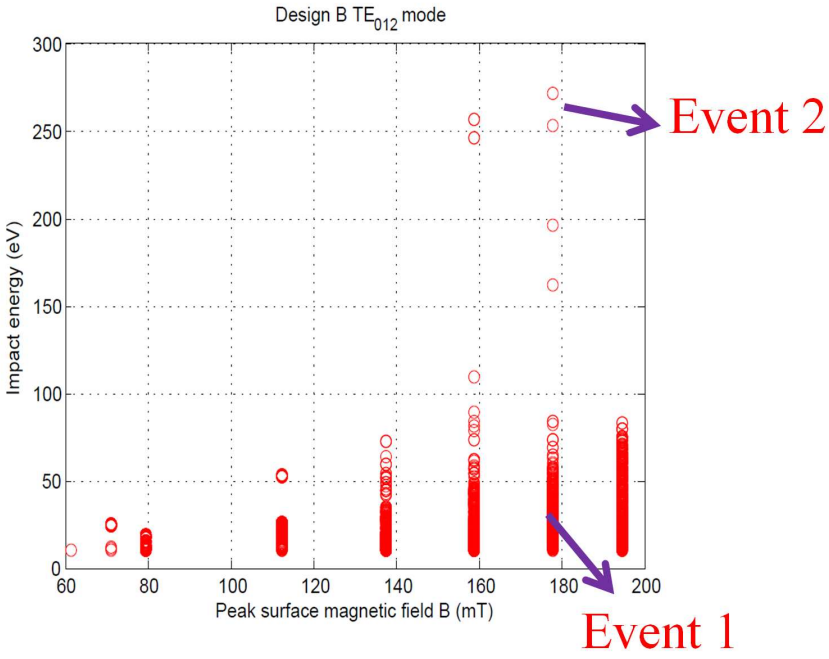

Figure 3.19: Impact energy dependence with cavity peak surface magnetic field values near the input coupler region for certain peak surface magnetic field. Only electrons with repetitive paths are shown here.

determined by the EM field. The tracing of electrons will continue for a specified number of rf cycles, after which resonant trajectories (possible multi-impact events) were identified.

Fig. 3.19 shows repetitive electrons impact energy as the function of peak magnetic field for the TE mushroom cavity simulated near the input coupler region. These resonant electrons are tracked individually to identify whether their traveling paths are repeatable over many rf cyles or not. Electrons that still survive after many rf cycles are possible multipacting electrons. Although we haven't identified any possible multipacting barriers, two events are used here to illustrate the identification process of the possible multipacting barriers. Event 1 has 50 impacts during 50 simulated rf cycles as shown in Fig. 3.20. From SEY data of niobium, this event will not cause the electron number to increase because the impact energy is too low. Event 2 has 11 impacts during 50 simulated rf cycles as shown in Fig. 3.21. The impacting energy is in the range of the high SEY region, but the trajectory is not stable when the individual electron path is identified [29]. Therefore, steady multipacting is not established.

Similar studies have shown that asymmetric coupling ports at the top of a TE mushroom cavity can cause sufficient distortion of the TE_{011} mode inside the cavity to lead to multipacting [30]. Our design confirms that by symmetrizing the side ports, the field distortion is minimized, and the monopole TE modes will not have multipacting barrier existing on the flat bottom plate and at the coupler port region [29].

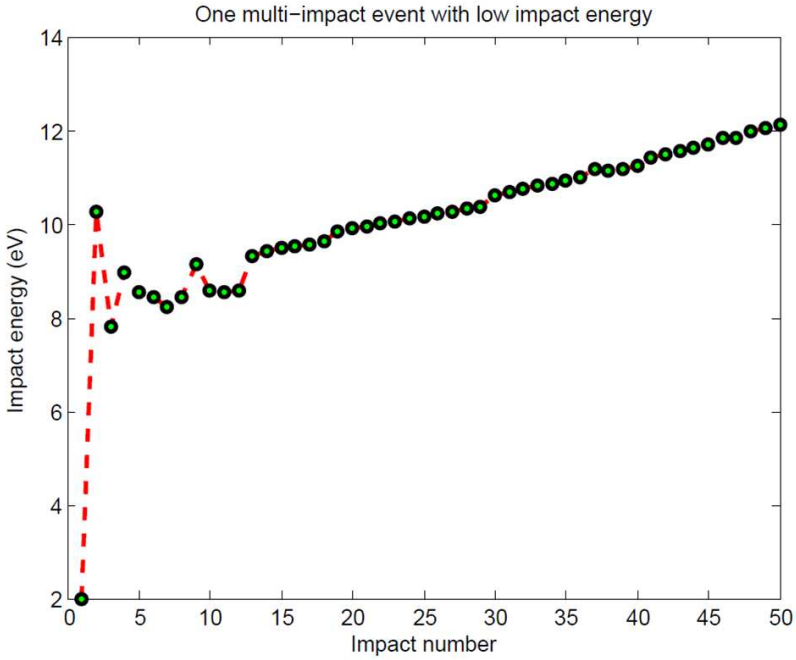

Figure 3.20: Impact energy dependence with impact number for event 1.

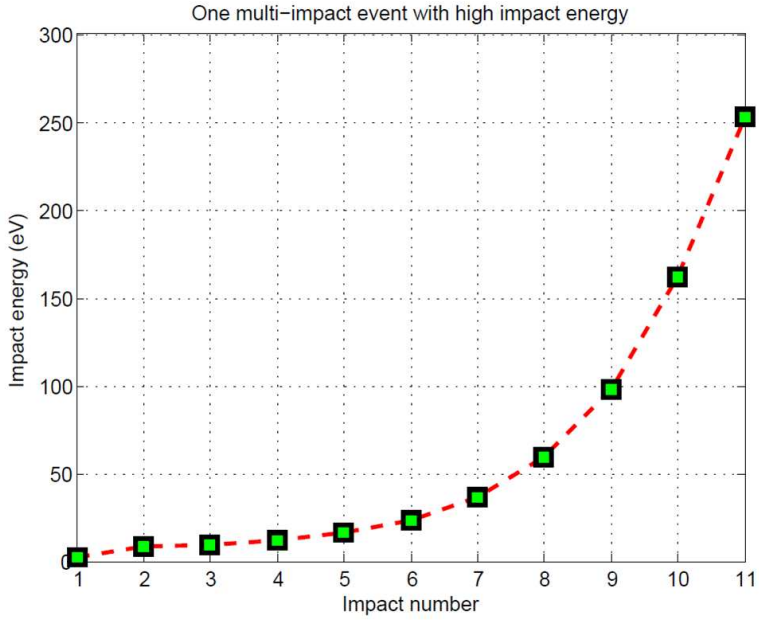

Figure 3.21: Impact energy dependence with impact number for event 2.

3.3.3 Pickup coupler

For the TE mushroom cavity, the pickup coupler/antenna is used to sample the stored energy inside the cavity. The so-called transmitted pick up signal is then used in determining the field inside the cavity and is also used as input signal to the phase lock loop to lock the rf drive to the cavity eigenfrequency. It has a very high external coupling factor Q_{ext}, i.e. a very weak coupling, in the 10^{12} range in order to avoid reducing the overall quality factor of the cavity. The pickup antenna consists of a type N connector feedthrough with an antenna tip made of copper. Fig. 3.22 shows the pickup antenna mounted to a transition piece from mini-Conflat to 1.5 inch indium flange.

Figure 3.22: The pickup coupler for the TE mushroom cavity.

Table 3.3: The design parameters of the TE mushroom cavity

	TE_{012}	TE_{013}
f(GHz)	4.78	6.16
$\frac{H_{max,sample}}{H_{max,cavity}}$	1.24	1.74
Sample diameter (cm)	9.525	9.525

3.4 TE sample host cavities and coupler fabrication

3.4.1 TE mushroom cavity

As discussed before, the mushroom shaped TE cavity operates at both TE_{012} and TE_{013} modes. The input coupler port is located at the center top of the mushroom type cavity and the pickup probe and pumping probe are distributed symmetrically along the input coupler port. In the final, fabricated version of this cavity, the sample plate diameter has been scaled from 10 cm to 9.525 cm (4.75 inch) in order to accommodate coating technique requirements on the sample size. The final parameters are shown in Tab. 3.3.

This cavity was fabricated from 3 mm thick, RRR 300 niobium sheets by the following steps; see also Fig. 3.23:

- forming of half cell ① and iris end tube ④ by deep drawing,
- machining transition piece ② from a solid niobium block, piece ③ and top tube ⑧ from niobium tubes,
- machining two side tubes ⑦ and weld flanges to tube ④,
- trimming of the weld areas between half cell ① and transition piece ②,

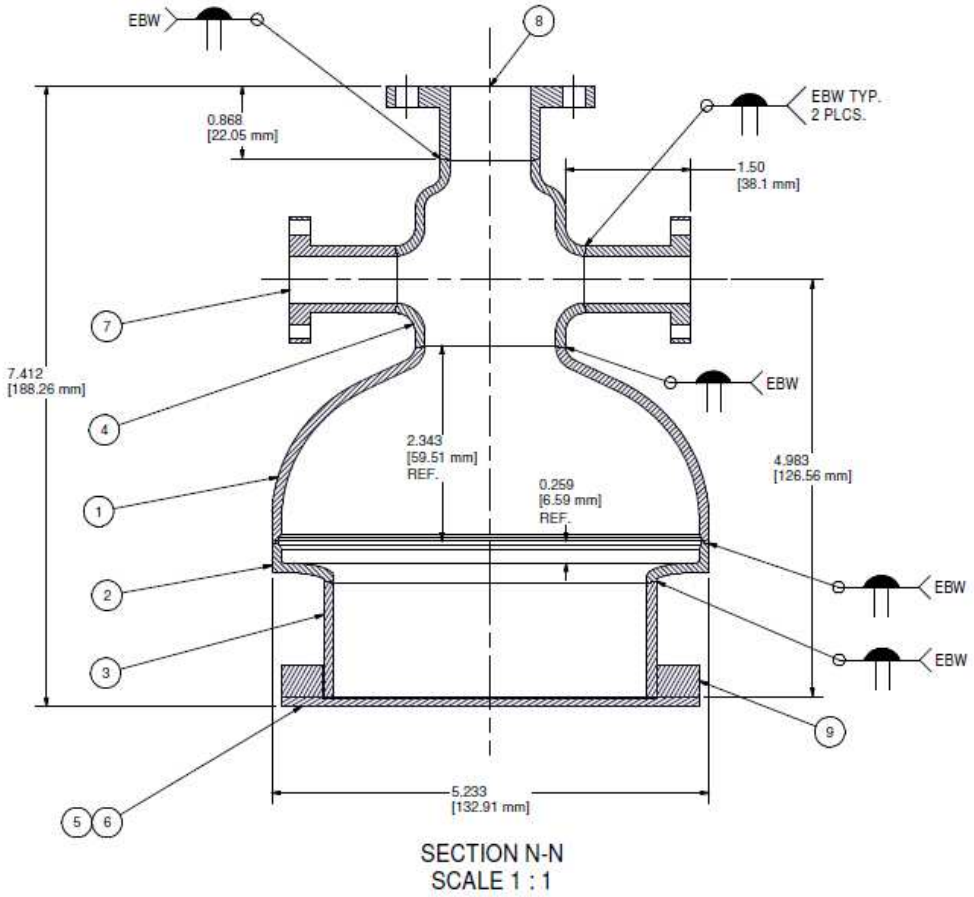

Figure 3.23: TE mushroom cavity mechanical drawing.

- all the parts are degreased in soap and water and received a light buffered chemical polish treatment (BCP),
- electron beam welding pieces including tube ③, transition piece ②, half cell ①, iris end tube ④ and top tube ⑧.

Deep drawing is a forming process where a metal sheet is pressed into certain shape by a set of dies. Fig. 3.24 shows the dies used to deep draw the half cell for the mushroom cavity. These dies are typically machined using 7075 aluminum due to its high yield strength. A Carl Zeiss coordinate measuremen-

t machine (CMM) was used to examine the shape of the half cell after deep drawing. It was found that the maximum deviation was 0.02 inch as shown in Fig. 3.25. After deep drawing, the trimming of the weld area was done on a CNC (computer numerical control) milling machine. Lubricants with good cooling must be used because of niobium is high reactivity with the oxygen. Then the trimmed parts and other tubes machined were degreased with detergent and soaked in cold BCP acid for half hour to remove the surface damage layer and clean the weld regions. All parts were electro-beam welded together in a vacuum chamber with pressure less than 10^{-5} torr. The weld parameters were selected to achieve full penetration welds by a defocused electron beam.

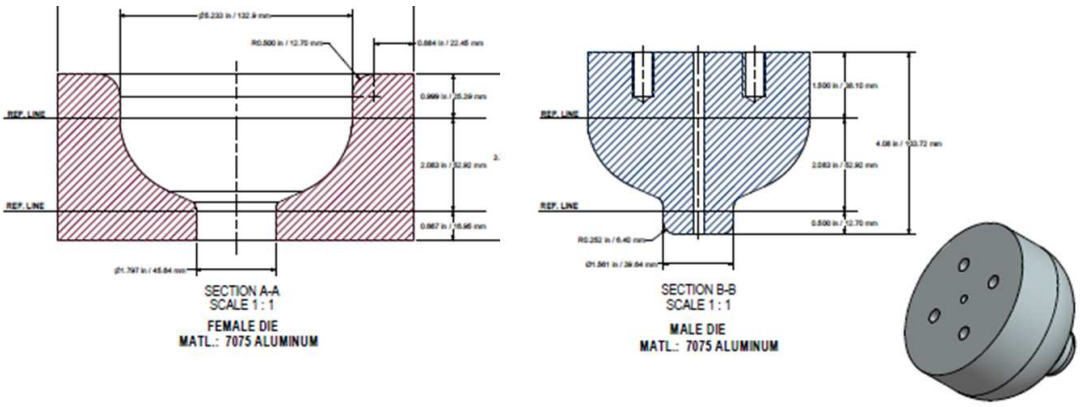

Figure 3.24: Dies for forming the mushroom cavity half cell.

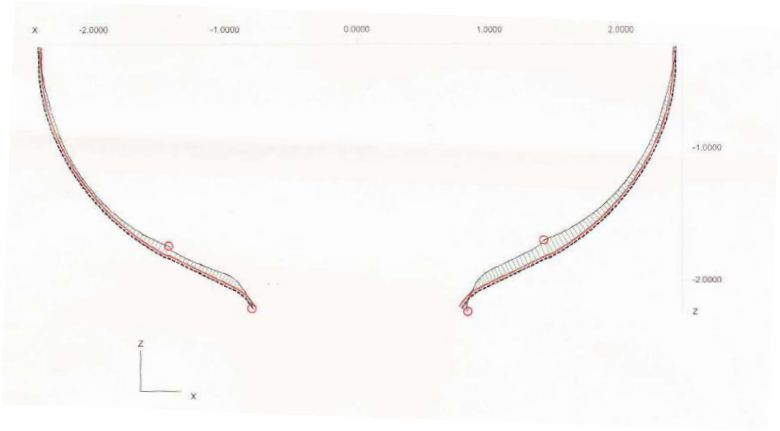

Figure 3.25: The profile of the mushroom cavity half cell. The red circle indicates the maximum deviation from design value. Black: ideal shape. Green:deviation from ideal shape, magnified by a certain factor. The maximum deviation is 0.02 inch.

The completed mushroom cavity after welding is shown in Fig. 3.26

Figure 3.26: Finished TE mushroom cavity after a heavy BCP.

3.4.2 TE pillbox cavity

(a) The pillbox tube section

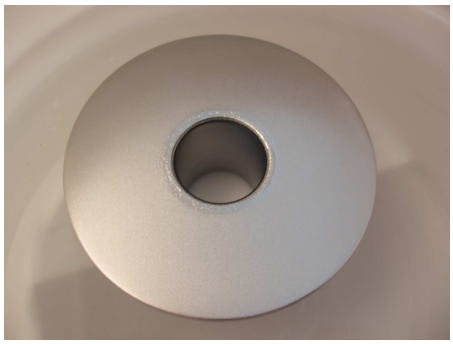

(b) The top plate with coupling port

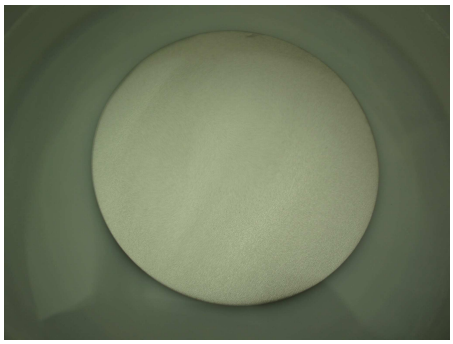

(c) The flat sample plate

(d) The fully assembled TE pillbox cavity.

Figure 3.27: The new TE pillbox sample host cavity with its three components.

The new TE pillbox cavity consists out of three parts, a tube with flanges, a top plate with a single input coupling tube and a flat sample plate as shown in Fig. 3.27. All parts were fabricated out of RRR 300 niobium, using fabrication and cleaning steps similar to the ones used for the mushroom cavity. For evacuating the cavity, an adapter tube with a pumping port is attached to the coupling tube. The three parts of the pillbox cavity are joint together by indium

wire seals, using flange clamp rings; see Fig. 3.27.

3.4.3 RF input coupler

The mechanical design of the rf input coupler for the TE mushroom cavity is shown in Fig. 3.28. The radii of inner and outer conductor are designed so that the impedance of the coaxial transmission line formed is 50 Ω, matching the rf connector impedance. The inner conductor is made out of oxygen-free copper. It consists out of three sections. The center section is a hollow tube and can be made of different length to accommodate different coupling variation requirements of the TE pillbox and mushroom cavities. The ceramic window is brazed to the the mounting flanges by cusil and nioro under 600°C in the furnace. The window is used for electric insulation between outer conductor and inner conductor of the input coupler. The rf connector is plated with silver to enhance electric and thermal conduction.

After brazing of the ceramic window, the mounting flange and the ceramic window were carefully washed and transferred into class-10 clean room with other parts for final assembly. The assembled coupler is shown in Fig. 3.29. Notice the off-center hook at the top of the antenna, providing efficient coupling to the magnetic field inside the TE cavity.

3.5 TE sample cavity test insert system design and fabrication

In the past, the old Cornell TE pillbox cavities were tested in a small helium dewar and not shielded well for residual magnetic field. Good magnetic shielding

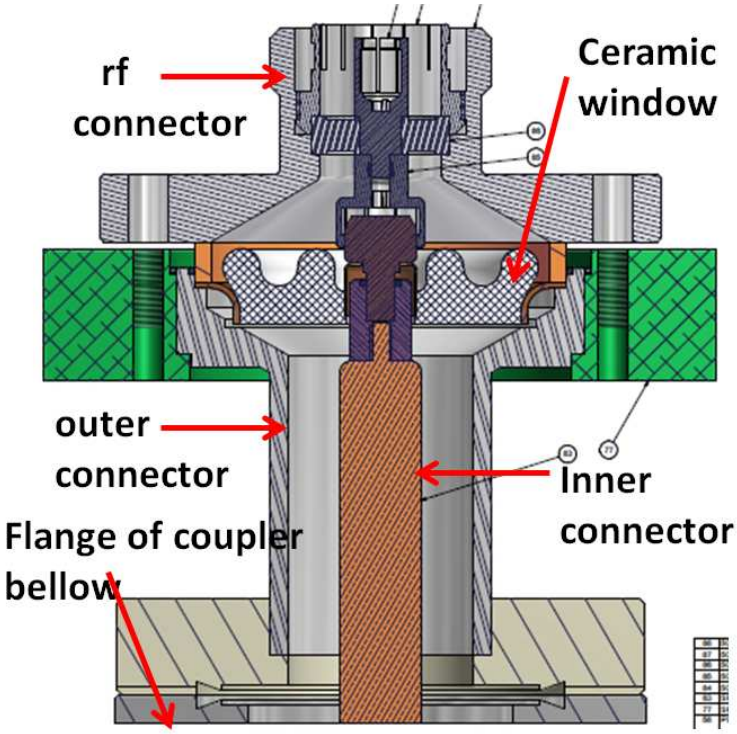

Figure 3.28: The mechanical design of the rf input coupler for the TE cavities.

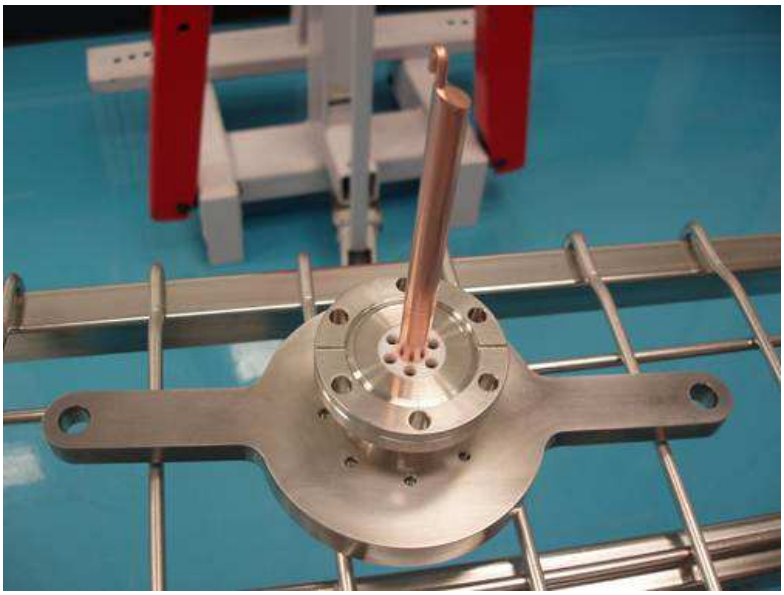

Figure 3.29: Completed rf input coupler for the TE cavities after final assembly.

is needed especially at higher rf frequencies as trapped magnetic flux induced residual surface resistance is proportional to the square root of frequency as shown before [1]. During the test, the helium was directly vented to the atmosphere and could not be recovered. Also, the small helium dewar did not allow adequate cooling of the cavities. Therefore, a completely redesigned, dedicated insert for the new TE pillbox and mushroom cavities was fabricated. It allows TE cavity testing inside the existing, well shielded center cryogenic dewar in Cornell's SRF lab.

The design of the new TE sample cavity test insert system has the following features (see also Fig. 3.30):

- The insert provides good mechanical support and balance of the cavities inside the liquid helium bath;
- In-situ pumping of the TE cavity by an ion pump can be done during rf test in addition to normal pumping through a turbo pump;
- The input coupler coupling can be adjusted by a stepping motor, controlling the penetration of the rf input coupler into the TE cavity;
- The insert provides adequate feedthroughs including ports for rf signals and a thermometer system for monitoring the helium bath temperature and the cavity wall temperature;
- Both the TE pillbox and the mushroom cavity can be mounted onto the same insert, using the same rf input coupler;

Fig. 3.30 shows the mechanical design of this dedicated insert for TE cavities. All the mechanical parts close to the cavity are fabricated from non-magnetic type 316N stainless steel. Two titanium rods are used to support the cavity

frame. Titanium is chosen because it has nearly the same thermal expansion coefficient as the niobium cavity. Fig. 3.31 shows the lower section of the completed new insert, adapted for either the pillbox or the mushroom TE host cavity.

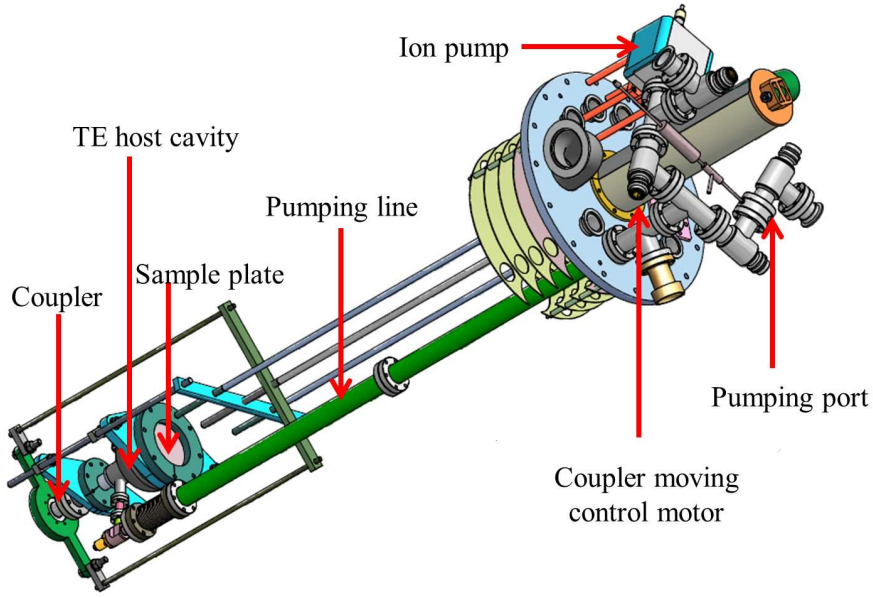

Figure 3.30: The mechanical design of the TE sample cavity test insert.

3.6 TE sample host cavity processing techniques

A fabricated cavity goes through many procedures before it is ready for final rf test. First the inside surface, especially the weld area, is optically inspected carefully. If the welds have imperfections, tumbling and other mechanical polishing techniques may be applied to smooth the questionable area. A light buffered chemical polishing (BCP) of about 20 ~ 50 μm then removes dirt left behind by the mechanical removal process.

Since 3 mm raw niobium sheet typically has a surface damage layer of 100 ~

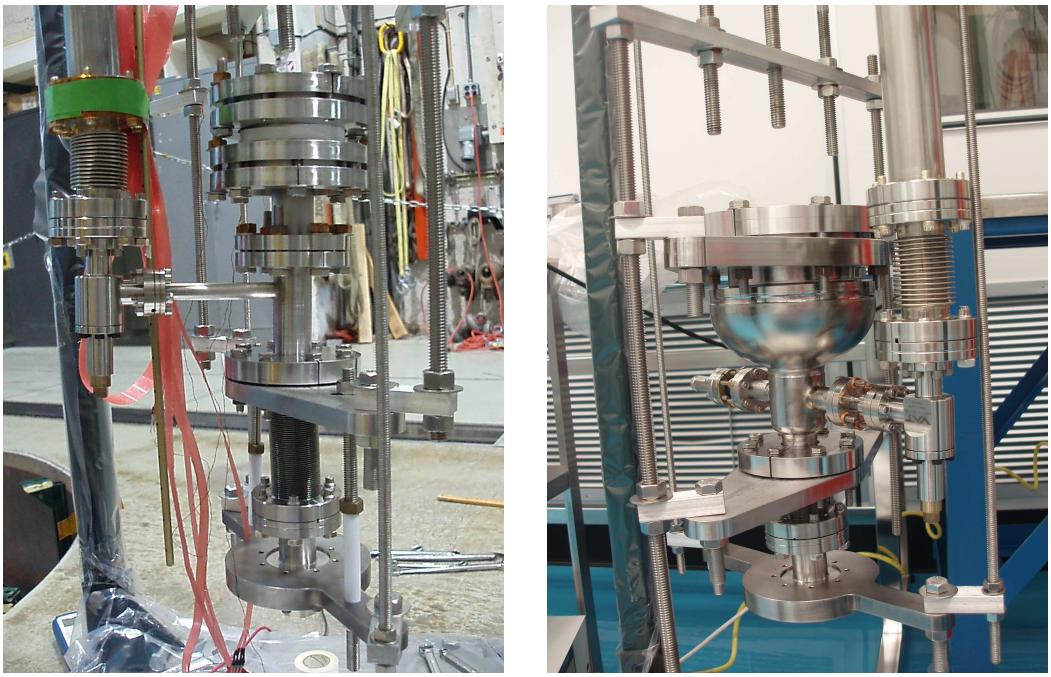

(a) (b)

Figure 3.31: Test insert for both the TE pillbox and mushroom cavities. The TE pillbox cavity with coupler is shown on the left. The TE mushroom cavity is shown on the right.

200 μm due to sheet rolling, a bulk chemistry is typically needed to remove this amount of material from the inner surface of the finished srf cavity. BCP is often used for this heavy etch for cavities not required to reach gradients above $\sim$ 100 mT. Electropolishing (EP) is an alternative to BCP, which generates a much smoother surface compared to BCP. It also results in higher gradient performance, allowing to reach surface magnetic fields above 100 mT when combined with a 120 °C, 48 hours bake [14]. There is chance of hydrogen contamination due to BCP and EP especially at higher acid temperatures.

High temperature annealing is used to relieve stress from the metal and remove hydrogen contamination brought by acid treatments. There are two common practices, one is 600°C for more than 10 hours and the other is 800 °C for 2

hours.

The final chemical treatment is a light etch of about 20 μm either by BCP or EP. After etching, high purity deionized (DI) water is used to rinse the cavity to remove acid residuals thoroughly. The cavity is then transferred to a class-10 clean room where the inside surface of the cavity is high pressure rinsed (HPR) with DI water for several hours. After the HPR, the cavity is left on the HPR stand for drying several days and then is assembled inside a class-10 clean room with great care.

To reach high fields, an electropolished cavity needs to be baked at 120 °C for 48 hours under vacuum in order to remove the high-field Q-slope as discussed in Chapter 2. Usually, the cavity is being baked in-situ, fully assembled and pumped under 10^{-7} torr. The 120 °C baking will not only removes the high field Q-slope, but also decrease BCS surface resistance by about a factor of two by lowering the mean free path of the electrons [14].

Since the normal BCP, EP, HPR, and baking facilities at Cornell's SRF group are designed for standard 1.3 GHz TM mode cavities, they had to be modified in order to allow processing of the 6 GHz TE pillbox and mushroom cavities. Those efforts are described in the following sections.

3.6.1 Buffered chemical polishing

The standard BCP uses an acid mixture of HF (48 % conc.), HNO_3 (65 % conc.) and H_3PO_4 (85 % conc.) in the volume ration 1:1:2. During the BCP process, the solution temperature must be kept below 15 °C to avoid hydrogen contam-

ination of the niobium [1]. When the acid mixture contacts the niobium metal, the nitric acid oxidizes the surface layer, forming a niobium oxide film. The hydrofluoric (HF) acid then reacts with the newly formed niobium oxide layer and removes it. The phosphoric acid is used to slow down the reaction rate because of its high viscosity.

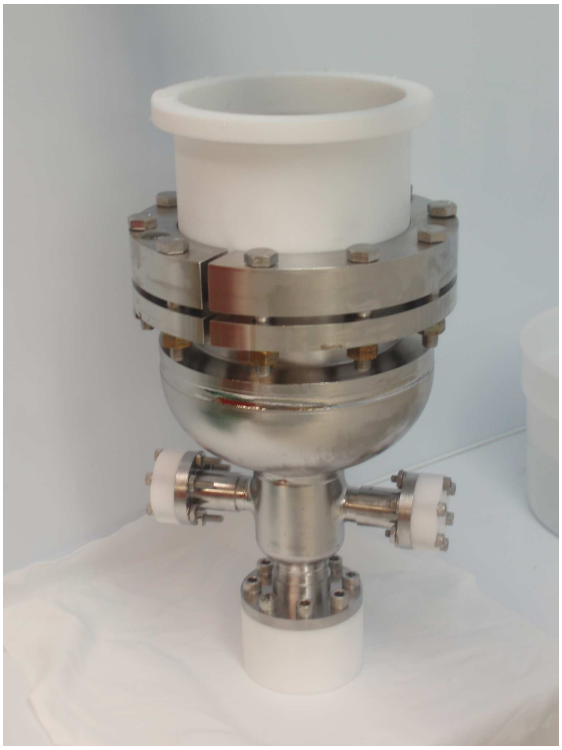

Figure 3.32: BCP seal setup for the TE mushroom cavity.

For the new TE pillbox cavity, all three parts are directly put inside the cold BCP solution. For the TE mushroom cavity, the cavity inside is filled with BCP solution with the two side ports being sealed by PTFE seals as shown in Fig. 3.32. During the BCP process, a mild stirring by a PTFE rod is used to keep the acid temperature uniform. A niobium sample is put inside the acid bath in the cavity and used as the gauge to monitor the etching rate.

Table 3.4: EP parameters for TE sample cavities

Current density	10~30 mA/cm^2
Voltage	14 V
Electrolyte temperature	≤22°C
Rotation speed	1~2 rpm
Acid flow rate	6~10 L/min

3.6.2 Electropolishing

The standard EP electrolyte is a mixture of HF (40 % conc.) and H_2SO_4 (98 % conc.) by volume ratio of 1:9. The niobium cavity is used as the anode and the cathode is typically made from pure 1100 series aluminum. The niobium surface turns into niobium pentoxide (Nb_2O_5) facilitated by the current induced electrons. Nb_2O_5 dissolves in the HF and converts into soluble NbF_5 or H_2NbOF_5. This process is repeated and results into continuous niobium etching. Hydrogen will generate from cathode and needs to be guided away. The entire solution is cooled below 22°C.

Fig. 3.33 shows the EP setup for the top and bottom plates of TE cavities inside a chemical room fume hood. PTFE o-rings are used to seal between polyvinylidene fluoride (PVDF) tubes, flanges and the niobium flat plate. The top PVDF cover has several holes to vent hydrogen generated in the EP process. In order to stir the acid during the electropolishing, there is a PVDF stirring rod rotated by a rotor-chain system which is powered by a square-wave generator. The stirring is essential to reduce the thickness of the viscous layer on the niobium surface so the EP current can sustain [14]. The whole setup is placed inside a secondary container which is cooled by running DI water. A similar setup can

be applied to every part of the TE pillbox and TE mushroom cavities. Table. 3.4 lists the range of voltage, current density, temperature, and flow rate typically used during the EP process.

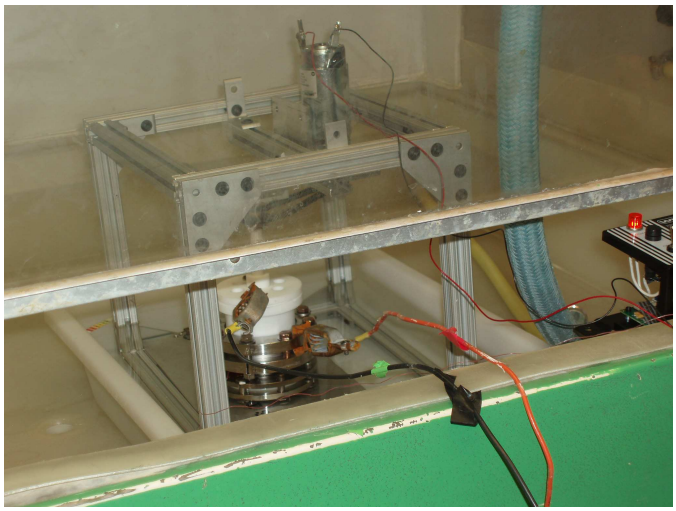

Figure 3.33: EP setup for the TE sample host cavities.

3.6.3 High temperature baking

Hydrogen contamination of the niobium generated during the EP or even BCP (if acid solution temperature too high) must be driven out by a furnace treatment. 800 °C for 2 hours and 600 °C for 10 hours are two ways commonly used to reduce the hydrogen concentration to below a few atomic ppm in the bulk. The heat treatment is also generally believed to help relieve stresses and dislocations introduced by mechanically rolling and deep drawing of the sheet niobium metal.

Because the TE sample cavities use an indium wire seal between the host cavities and sample plates, and the melting point of indium is 156.6 °C, the host

cavities and the sample plates must be baked separately. Fig. 3.34 shows the temperature of the TE pillbox cavity during its 800 °C heat treatment together with the vacuum pressure in the furnace as function of time. It can be observed that during the 2 hour treatment the furnace vacuum initially rises due to hydrogen release from the niobium cavity. As time progresses, less hydrogen is released and the vacuum pressure drops due to active pumping on the furnace vacuum by cryogenic pumps.

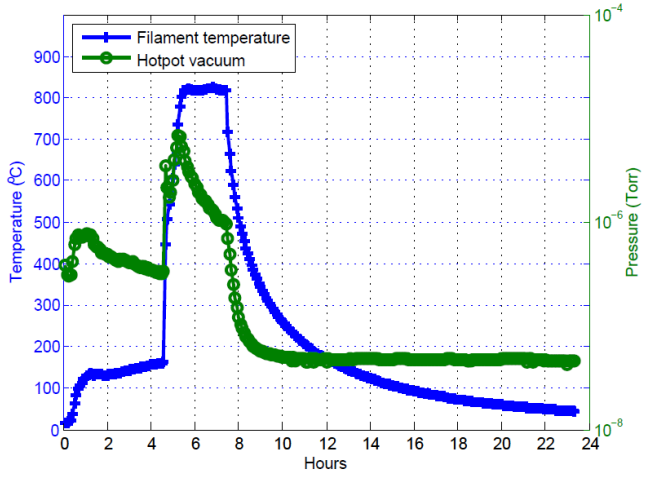

Figure 3.34: Furnace vacuum and cavity temperature vs time during the 800 °C treatment of the TE pillbox cavity.

3.6.4 Low temperature baking

Mild baking at around 120 °C for 48 hours was discovered to eliminate the high-field Q-slope for large grain BCP and all grain sized EP cavities [14]. In practice, the cavity can be baked by hot air in a thermal insulation box placed around the cavity while the inside of the cavity is kept under vacuum. Usually, this is done as the last step prior to the rf test of a cavity. However, due to the lower

melting temperature of the indium wire seal used in assembling the TE cavities, the individual TE cavity parts need to be baked at 120 °C before assembly. Fig. 3.35 shows the mechanical design of the setup used for the low temperature bake of the TE cavity parts. The long pumping tube is designed to maintain the thermal gradient from the 120°C of the heating chamber to room temperature at the pumping line. During the baking, the vacuum inside the heating chamber is kept below 10^{-7} torr. After the baking, the chamber is sealed at the pumping port and transferred directly to the class-10 clean room for assembly of the TE cavity. Past experience has shown that the low temperature baking benefits are preserved even if the niobium is exposed to air or water after the baking [14].

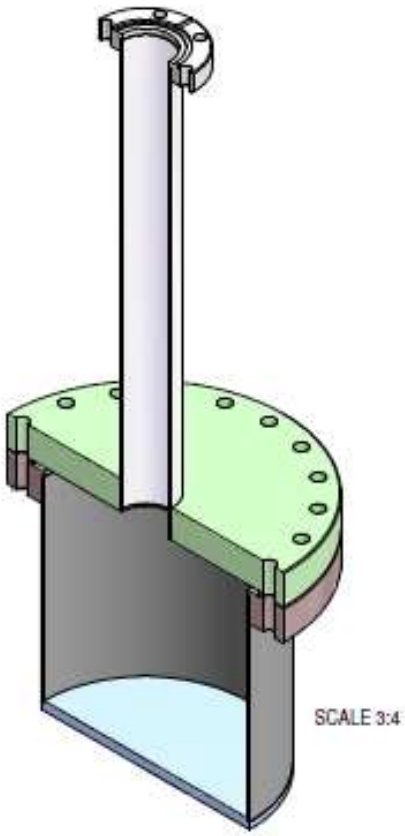

Figure 3.35: A setup for the 120 °C bake of the TE sample cavity parts under vacuum.

Table 3.5: HPR parameters for cleaning of the TE sample cavities

Water flow rate	5~20 L/min
Pressure	10^7 Pa
Filter pore size	$\leq 0.1\mu$m
Rotational speed	2 rpm

3.6.5 High pressure rinsing

Rinsing with high pressure pure DI water is the most effective way of remove microparticles from the inside surface of the srf cavities that may lead to electron field emission and quench during rf test. Although TE monopole mode cavities are not vulnerable to field emission due to the zero perpendicular electric field presence on the cavity surface, cleaning all the dust particles is still very important to reduce the residual loss they might cause and raise the quench field of the TE cavities. The TE host cavities and sample plates need to be cleaned separately due to the indium wire seal. A special design for holding the flat sample plates and a small diameter HPR nozzle head were developed for cleaning of the sample plates and of the host TE cavities. HPR must be carried out inside a class-10 clean room to prevent recontamination. Fig. 3.36 shows the special setups used during high-pressure rinsing of the TE cavity parts. Table. 3.5 summarizes the HPR parameters for TE cavities.

3.7 Pits cavity design and fabrication

As discussed in the introduction, a single cell cavity with artificial pits is an ideal tool to investigate pits induced cavity quench and even the high field Q-

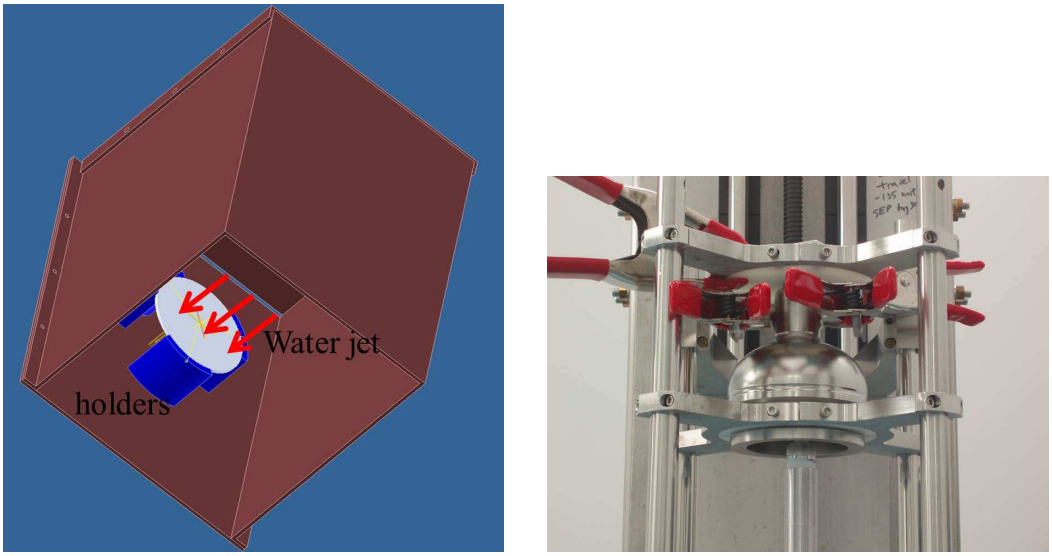

(a) (b)

Figure 3.36: HPR setup for cleaning of the flat sample plates (left) and of the host cavities (right).

slope phenomena. The Magnetic field enhancement (MFE) factor h at the pit edges depends only on pit radius R and edge radius r if the pit depth is several times larger than its radius (see Chapter 6 for a detailed discussion of the field enhancement by pits).

A single cell 1.3 GHz niobium cavity of the Cornell ERL center cell shape was fabricated. Prior to joining the two halves of the cavity by electro beam welding, 30 pits of various radii were drilled into the inside niobium wall in the high magnetic field region of the cavity, each 1.5 mm deep, which is half of the wall thickness of the cavity. Fig. 3.37 shows the fabricated half cup with different sizes of pits. In order to obtain different MFE factors of the artificial pits, pit of 5 different radii R were drilled perpendicular to the cavity wall, with six copies of each size. After drilling the pits and after final electron beam welding of the equator to join the two cavity halves, a heavy BCP of about 120 μm was applied to the pits cavity. This BCP process determined the pits edge radius r along

Figure 3.37: Half cup of the pit cavity after drilling of the pits.

Table 3.6: Pit parameters for the pits cavity

Total number of pits	30
Pits radii	200, 300, 400, 600, 750 μm
Pits edge radii	initially unknown
Pits depth	1.5 mm
Pits position	1 inch from the cavity equator

with the different drill sizes used. The parameters of the pits are summarized in Table. 3.6. Fig. 3.38 shows the pit positions at the cavity inner surface.

In order to use the Cornell single-cell temperature mapping system to record the rf heating from the pits, the pit position pattern is matched to thermometry sensor positions. In the pit cavity, pits are spaced by 18.95 deg, so that a pit is located under a specific temperature sensor on every other board. The single-

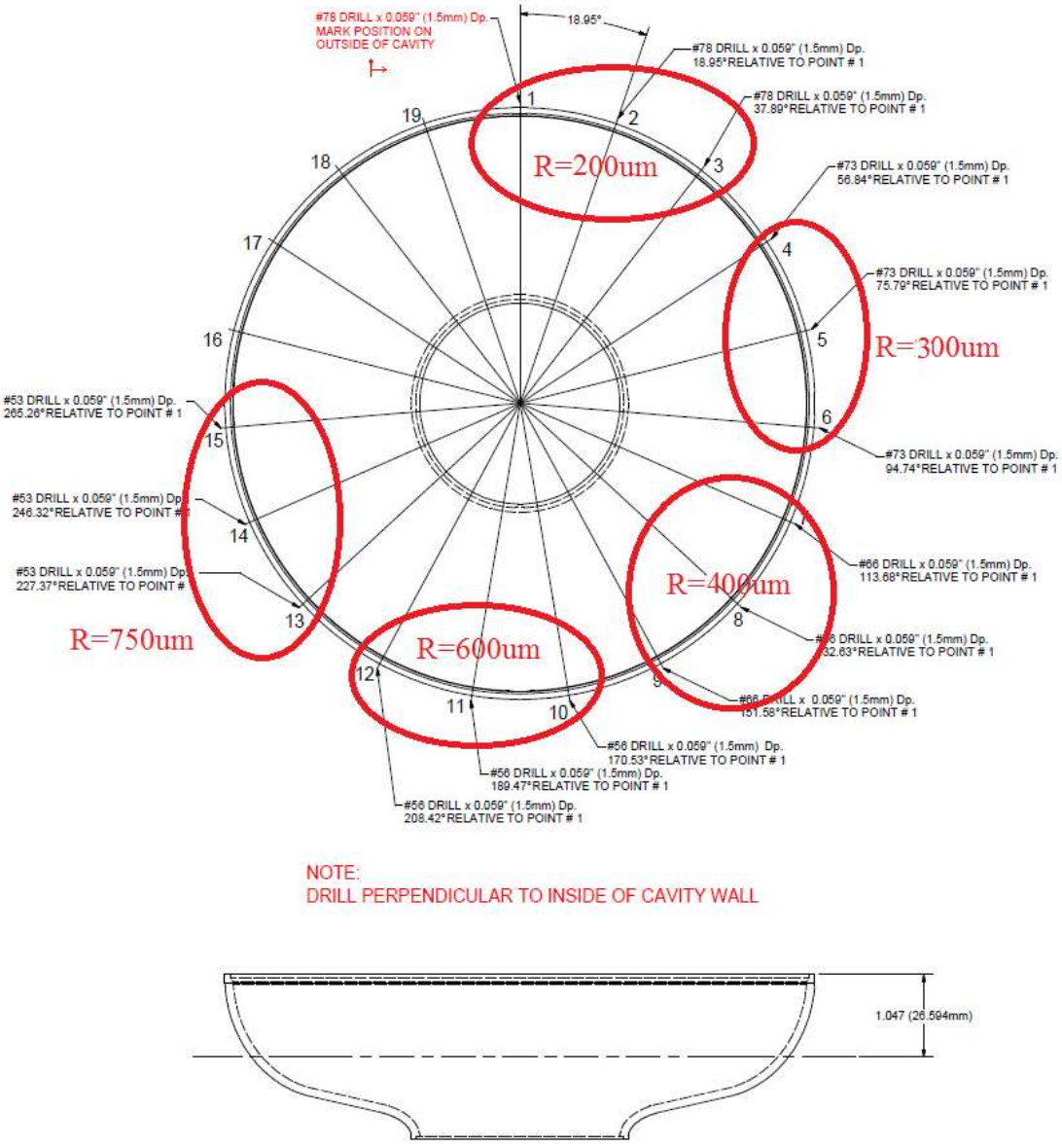

Figure 3.38: Distribution of pits along the inner surface of the cavity.

cell T-map has 38 boards in the azimuthal direction, thus the boards are spaced by 9.47 deg. For example, pit positions 1 to 3 have a radius of 200 μm and pit positions 4 to 6 have a radius of 300 μm. Note that pits are located symmetric to the equator, so that at every given angular position there are two pits, one above and one below the equator. Since all pits are located at the same distance from the equator, they all will see the same local magnetic field, not taking into account any differences in magnetic field enhancement by the pits.

3.8 Cavity thermometry system

3.8.1 Single-cell cavity thermometry system

The thermometry system operates in parallel with the cavity rf test system to record the rf heating at the cavity inner surface. A temperature mapping system based on a previous design [23] was developed to fit on ILC and Cornell ERL shape single cell cavities. On each board, 17 Allan Bradley carbon resistors are arranged, with a total of 38 boards surrounding the cavity, providing a complete coverage of the cavity. Three additional carbon resistors are suspended in the helium bath recording helium temperatures and are calibrated with standard Cernox censors. A national instruments DAQ system is used to measure the resistance of the resistors. Fig. 3.39 shows the system which was used to record the rf heating from the cavity pits.

The following steps were taken to ensure that the single-cell thermometry system achieves nΩ surface resistance resolution:

- To reduce electronics noise, a battery was used instead of a standard voltage supply.
- The DAQ system used differential inputs instead of a single ended measurement scheme.
- Each channel was read 1000 times in a row at 25 kHz, and then the average value was calculated.
- Temperature maps were taken both with and without rf to reduce calibration offsets, and several temperature maps were recorded and then averaged to further decrease the noise level.

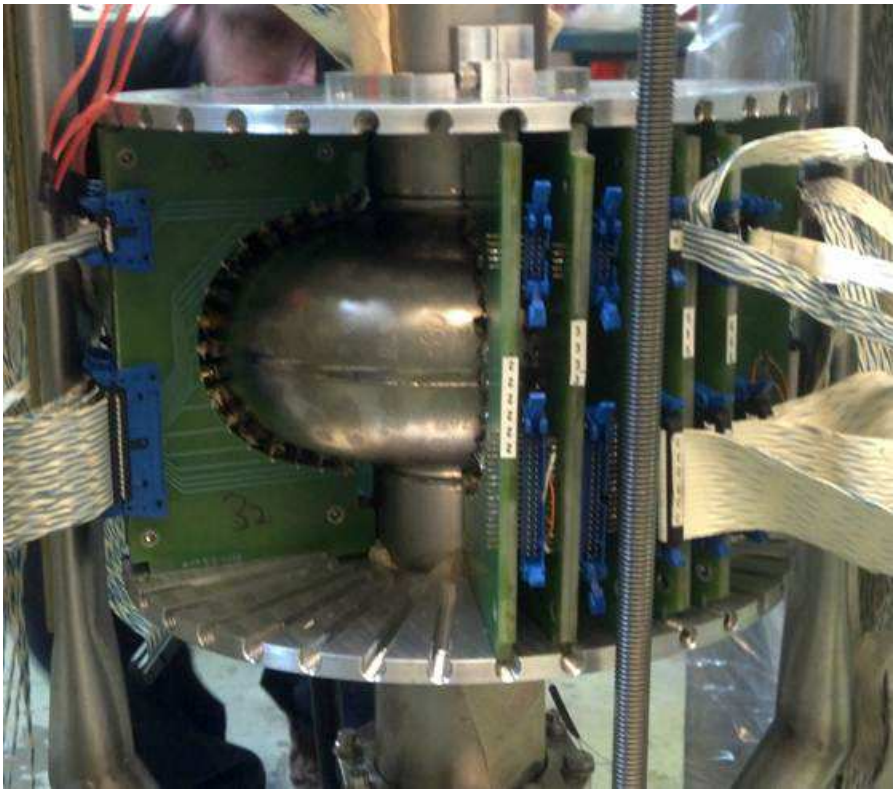

Figure 3.39: The single-cell thermometry system for the pit cavity.

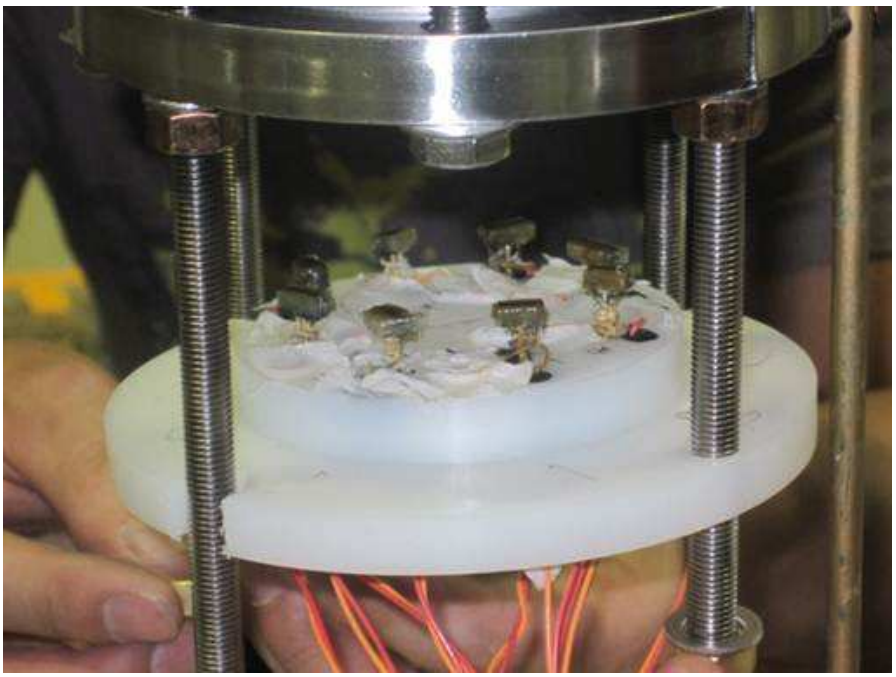

Figure 3.40: The thermometry system for the sample plate of the TE pillbox cavity.

3.8.2 TE cavity thermometry system

Using the same concepts as for the single-cell temperature mapping system, a ring of 8 thermometers (Allan-Bradley resistors) has been mounted near the highest magnetic field region on the bottom plate of the TE pillbox cavity, and can successfully detect surface resistance with nΩ resolution. Fig. 3.40 shows the thermometer setup. The thermometers are directly mounted on a flat teflon plate. The distribution of the thermometers can be seen as in Fig. 3.41. For the TE mushroom cavity, a larger size teflon plate can be used and accommodate more thermometers.

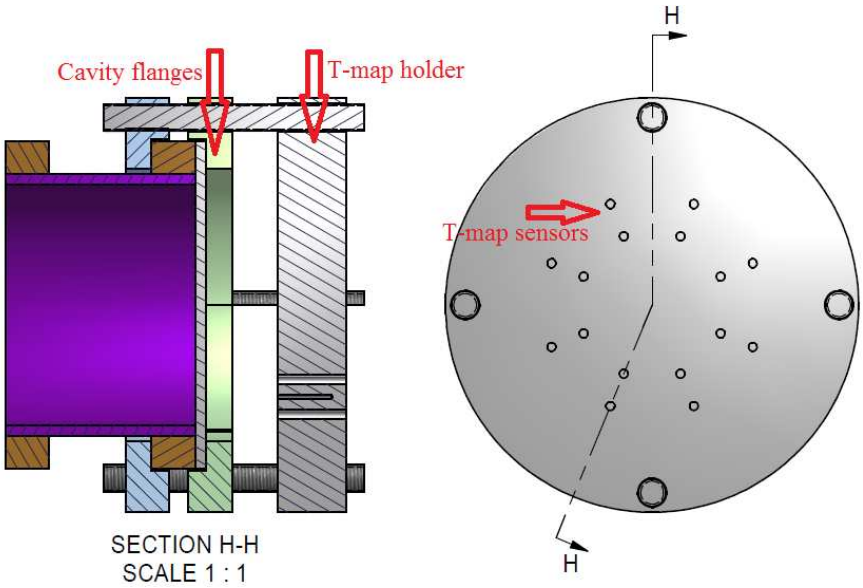

Figure 3.41: The thermometers distribution for the TE pillbox cavity. Note that there are two holes for the cables of each temperature sensor.

CHAPTER 4

TE CAVITIES EXPERIMENTAL RESULTS

4.1 Cavity rf tests with reflected power feedback

Testing of srf cavities is central in superconducting rf research because it measures two important properties: the cavity intrisic quality factor Q_0 as a function of the accelerating field E_{acc}. In the case of the TE sample host cavities, the maximum surface magnetic field H_{max} is measured instead of E_{acc} to quantify the field handling capability of the sample host cavities.

For resonant excitation of the targeted GHz range mode with an extremely narrow bandwidth of less than one Hz, a feedback system is required to keep the frequency of the driving rf source on the cavity resonance. Usually, a phase-locked loop (PLL) is used for this purpose, using rf probe signals of the rf drive and of the cavity field probe (transmitted power signal P_t) [31]. In ordinary TM mode cavity tests, the signal from the transmitted power probe P_t is used to provide the feedback signal. However, in a TE sample host cavity test, the signal from the rf power reflected by the cavity is used instead of the transmitted signal, because there is no transmitted power probe available.

The way a PLL works is that the reflected power P_r and a sampling of the drive rf are fed into an rf mixer. The mixer generates a voltage proportional to the phase difference between the two input signals. The output of the mixer is then used to determine the frequency of the voltage-controlled oscillator, e.g. the rf signal generator. By introducing a phase shift to the sample rf signal, the mixer generates zero voltage when the cavity is operating on resonance [1].

Fig. 4.1 shows the schematic of the feedback arrangement used during cavity test, along with other components needed to measured the forward power P_f, and rf reflected power P_r. An Agilent E8257D analog rf signal generator produces a rf signal up to 14 dBm in power, which is then send to a pre-amplifier. The output power level of the pre-amplifier can be adjusted by a variable attenuator for driving the cavity at different power levels. This output signal then is amplified by a 2-6 GHz traveling wave tube amplifier (TWTA) and fed into the cavity through the input coupler at the bottom of the cavity. Two directional couplers are used after the TWTA. Between two directional couplers there is a high power circulator which can handle up to 250 Watt of rf power.

The first directional coupler diverts part of the forward power P_f to a rf power meter for measurement. The second directional coupler is used to measure the reflected power P_r from the cavity. The circulator is used to prevent reflected power from reaching the TWTA, which could damage the amplifier. Instead, the reflected power is directed to a rf load by the circulator.

Part of the reflected power P_r is diverted and amplified to the "rf" input of a mixer. The second input to the rf mixer is a probe signal of the rf drive power. The mixer output voltage varies as follows: voltage $V = A_1 A_2 \sin(\Delta\Phi)$, where A_1 and A_2 are the rf signal strengths of the two input signals and $\Delta\Phi$ is the phase difference between the two input rf signals.

A phase shifter is used to adjust the relative phase difference of the the mixers' two inputs. The mixer outputs is used as a frequency modulation input of the rf signal generator to keep the rf drive frequency at the cavity resonance frequency, thus always driving the cavity on resonance.

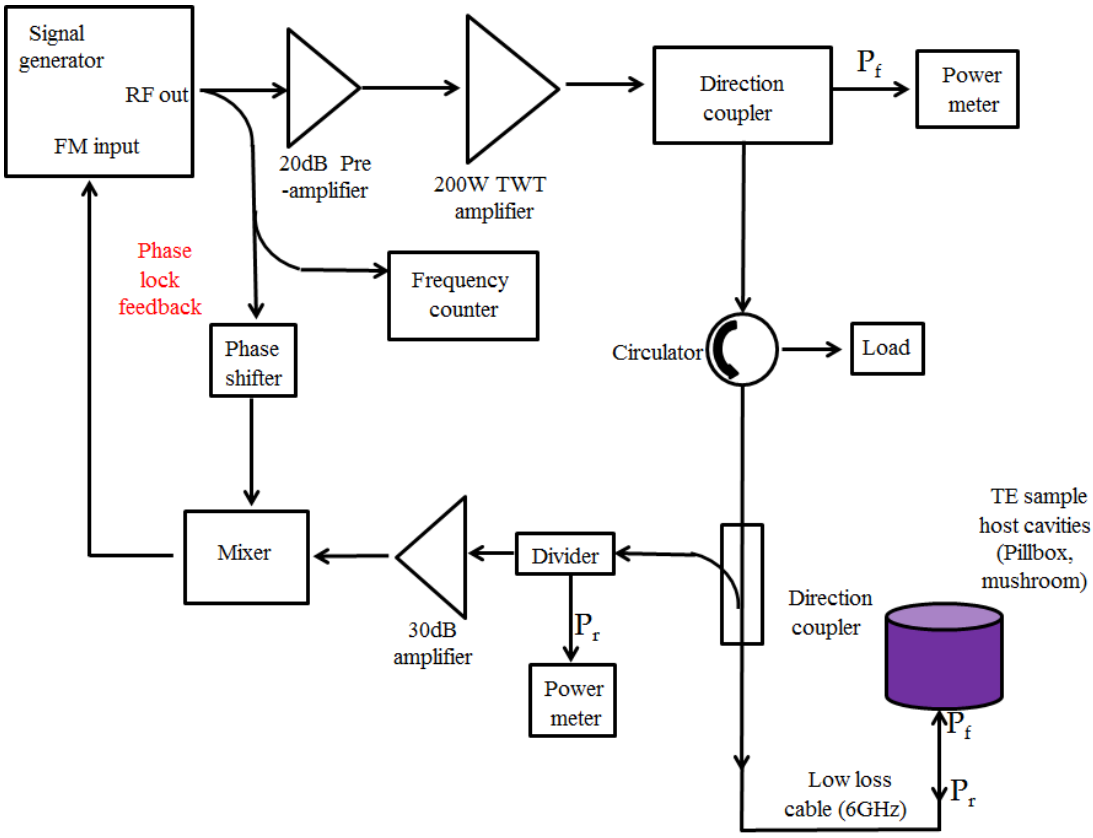

Figure 4.1: Schematic of the test equipment for rf measurements for the TE sample host cavities.

During the TE sample host cavity tests, the cavity quality factor Q_0 and the maximum surface magnetic field H_{max} are determined at every field level by measuring absolute values of forward power P_f, reflected power P_r and emitted power from input coupler P_e. Prior to a cavity test, coaxial cable losses of the rf cables leading to the cryostat are determined. Special low loss 6 GHz cables are used since cable rf losses increases with frequency.

The power reflected from the cavity P_r is minimized by adjusting the phase offset of the PLL feedback via a phase shifter. This ensures that the cavity is driven on resonance. Then the rf drive power is switched off, and the reflected

power trace is measured and recorded by a power meter. From the reflected power meter trace, the stable reflected power P_r and emitted power P_e can be determined. Fig. 4.2 shows an example of the reflected power after the drive rf power has been turned off, from which the decay time constant τ can be extracted.

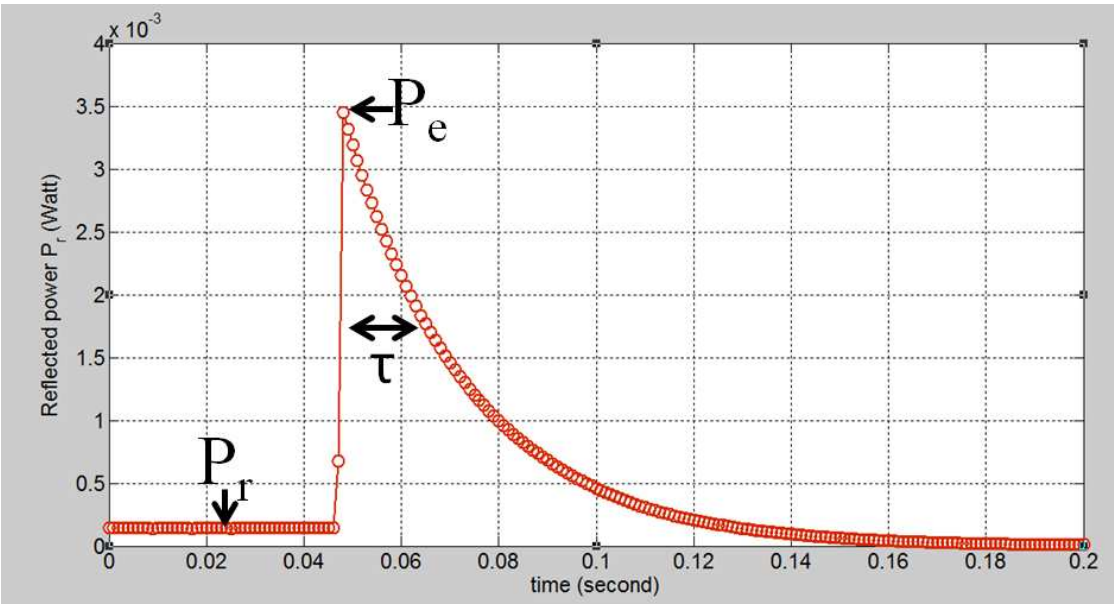

Figure 4.2: Reflected power measured by a power meters. The rf drive power to the cavity was turned of at t = 0.047 sec.

In the following, the equations needed to determine Q_0 and H_{max} from the measured power signals are presented. More details and derivation of these equations can be found in [1].

The coupling factor $\beta = \frac{Q_0}{Q_{ext}}$ of the input coupler can be calculated from either P_r or P_e. Here Q_0 is the quality factor related to the intrinsic losses in the cavity, i.e. the wall losses, and Q_{ext} is the external quality factor of the rf input coupler. In practice, those two methods are both used and an average is taken to deduce

β [1].

$$\beta_e = \frac{1}{2\sqrt{\frac{P_f}{P_e}} - 1} \tag{4.1}$$

$$\beta_r = \frac{1 \pm \sqrt{\frac{P_r}{P_f}}}{1 \mp \sqrt{\frac{P_r}{P_f}}} \tag{4.2}$$

In the later formula the upper sign is used if the coupling factor β larger than 1 and the lower one otherwise. The cavity intrinsic quality factor Q_0 is determined by

$$Q_0 = 2\pi f_0 \tau(1+\beta) \tag{4.3}$$

Here f_0 is the cavity resonance frequency.

The power dissipated in the cavity walls P_{diss} is given by

$$P_{diss} = \frac{4\beta P_f}{(1+\beta)^2} \tag{4.4}$$

Then the maximum surface magnetic field achieved in the TE sample host cavity can be found from

$$H_{max} = \kappa_m \sqrt{\frac{P_{diss} Q_0}{2\pi f_0}} \tag{4.5}$$

where κ_m is defined as the ratio between the maximum magnetic surface field H_{max} and the square root of the energy stored in the cavity.

$$\kappa_m = \frac{H_{max}}{\sqrt{U}} \tag{4.6}$$

κ_m is unique for any specific cavity geometry and can be calculated by numerical methods.

By raising the rf drive power level in continuous operation, the cavity quality factor Q_0 can be measured as function of the maximum surface magnetic field

H_{max} at a given temperature. The cavity temperature is measured by Cernox sensor immersed in the helium bath.

4.2 TE pillbox cavity rf test results

Preparing superconducting cavities for rf test takes several steps in order to thoroughly clean the rf surface. Before rf test, the rf surface of the TE pillbox cavity was cleaned by the following procedures:

- All three parts including the pillbox cavity tube, the top plate and the sample niobium bottom plate were immersed overnight inside a nitric acid bath to remove any possible residues from the indium seal at the flanges;
- All three parts were then immersed inside of BCP acid solutions for etching of 120 μm. The acid temperature was kept below 15 °C to avoid hydrogen contamination of the niobium. The typical etching rate is 1~2 μm/min;
- All three parts received at least 1 hour of high purity deionized water rinsing. After the rinsing, parts were blown dry by clean nitrogen gas and bagged;
- A two hour, 800 °C furnace heat treatment was performed for all three parts. During the baking process, the furnace pressure was kept below 10^{-7} torr.
- After the baking, all three parts were bagged and then transferred inside a class-10 clean room. High-pressure rinsing (HPR) was performed separately for all three parts. After HPR, each part was left on the HPR stand for drying.

- When all the parts were dry, they were carefully assembled with indium wire seals inside a class-10 clean room. The rf input coupler was also assembled and attached to the cavity via the coupler port on the cavity.
- The cavity with the coupler was attached to the test insert inside the clean room and evacuated. Slow pumping the cavity is needed to prevent turbulent flow and dust contaminations.
- The insert was moved outside the clean room and transferred into the cryostat for testing.

During the cavity test, the TE_{011} mode was first identified by measuring the scattering parameter S11 from the input coupler port. The measured frequency frequency of the TE_{011} mode was found to be 5.883 GHz at 1.6 K. This is in good agreement with the 5.881 GHz frequency simulated by SLAC O3P. The small 2 MHz difference is likely due to small machining errors and misalignments. The measured TM_{110} mode frequency is more than 10 MHz away from the TE_{011} mode which proves that the presence of the single coupler tube can efficiently remove the mode degeneracy between the TE_{011} and TM_{110} mode.

The TE pillbox cavity with a baseline niobium sample plate was tested at 1.6 K. Fig. 4.3 shows the measured cavity quality factor Q_0 as function of maximum surface magnetic field on the sample plate. The highest magnetic field achieved on the sample surface is about 450 Oe. Given that the ratio between $H_{max,sample}$ and $H_{max,cavity}$ for TE pillbox is 0.77 for the TE pillbox cavity, the highest magnetic field achieved on the cavity surface is around 600 Oe at the middle of the pillbox tube. At about 350 Oe on the sample surface, the cavity quality factor Q_0 suddenly dropped by about 30% for unknown reason. Above 450 Oe, the cavity quenched as indicated in Fig. 4.4 by sudden increases in reflected power caused

by sudden change in the cavity's quality factor.

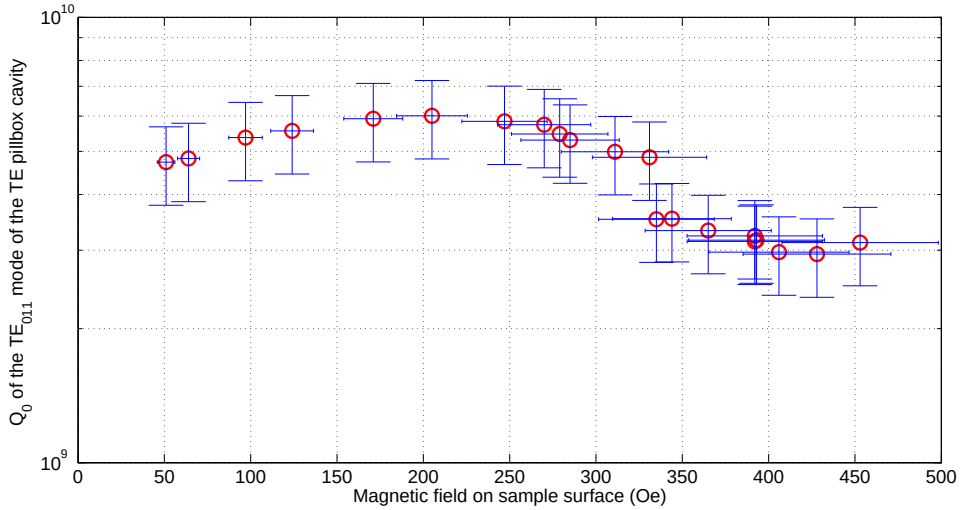

Figure 4.3: TE pillbox cavity quality factor Q_0 versus maximum magnetic field on the sample plate. The uncertainty in measured field is ± 10 % and the uncertainty in measured Q_0 is ± 20 %.

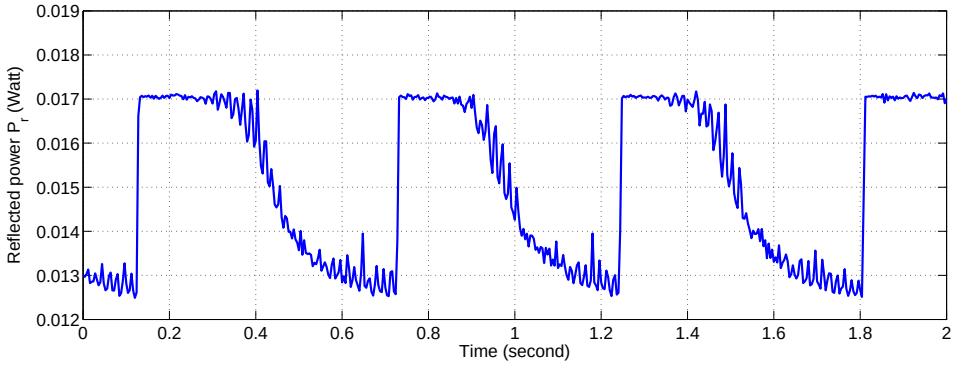

Figure 4.4: Reflected power trace when the TE pillbox cavity quenched repeatedly.

The BCS resistance of niobium at 6 GHz and 1.6 K is about 25 nΩ. Assuming the highest measured quality factor Q_0 as 6×10^9 at 200 Oe, the TE pillbox cavity surface resistance is about 125 nΩ. This indicates there is at least about 100 nΩ

of residual resistance. Likely, this residual loss can be attributed to rf losses at the normal conducting input coupler. In order to quantify the coupler losses, we changed the input coupling strength by moving the off-center hook coupler and found that the measured cavity Q_0 does change with the external coupling Q_{ext}. That means there is significant amount of coupler losses at stronger couplings.

4.3 TE mushroom cavity rf test results

The cavity was tested at 4.2 K and 1.6 K several times with a flat baseline niobium sample plate. The surfaces of the TE mushroom host cavity and the sample plate have been treated exactly the same as the TE pillbox cavity as described in section 4.2. During rf test, no multipacting or field emission was observed, as predicted by simulations. Since the frequencies of TE_{012} and TE_{013} modes are relatively high and a significant number of cavity eigenmodes exist with similar frequencies, a careful measurement of the input coupler scattering parameter S11 was done at different couplings to identify the TE monopole modes. Fig. 4.5 shows all the modes measured between 2 GHz and 6 GHz for the TE mushroom cavity, and compares the measured frequencies to the simulated values in order to identify the TE modes of the cavity.

After identifying the operating TE modes of the cavity, the performance of the TE_{013} modes was measured. Fig. 4.6 shows the cavity quality factor for the TE_{013} mode versus the achieved magnetic field on the sample surface. The highest cavity quality factor is 3×10^9 at 100 Oe. The highest achieved magnetic field on the sample surface is about 600 Oe. Above 600 Oe, the cavity quenched as Fig. 4.7 shows by the sudden increases in reflected power.

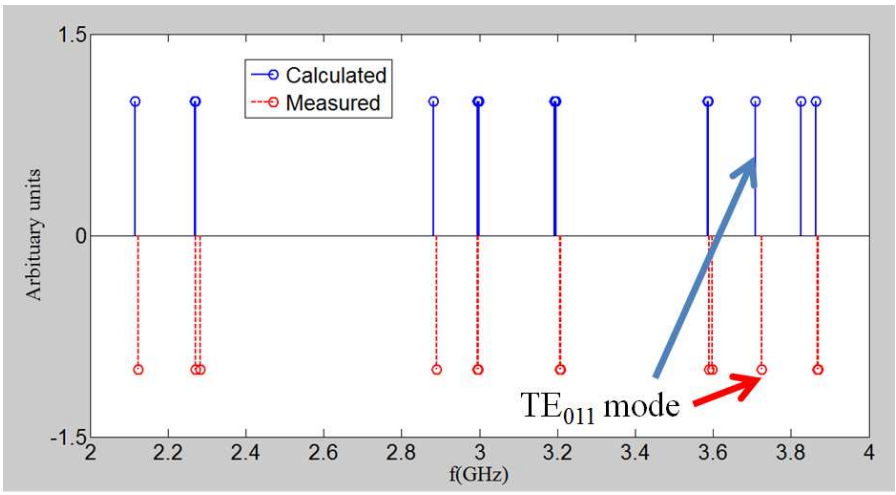

(a) 2-4 GHz

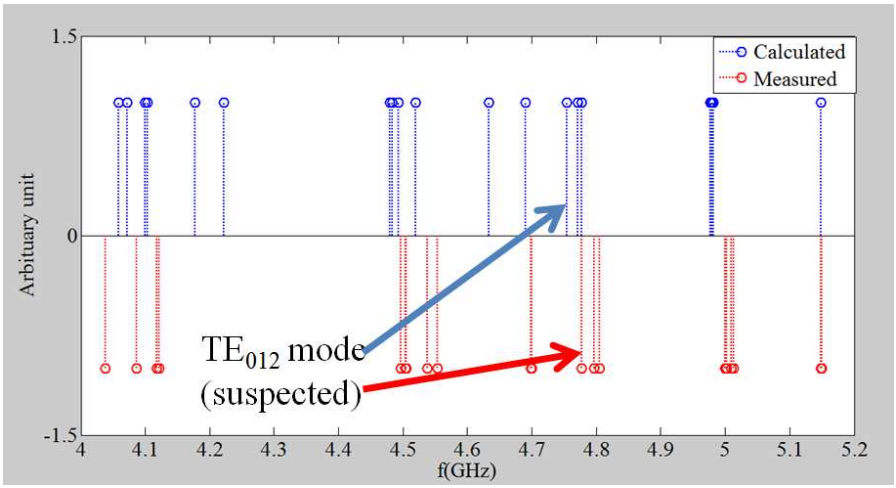

(b) 4-5.2 GHz

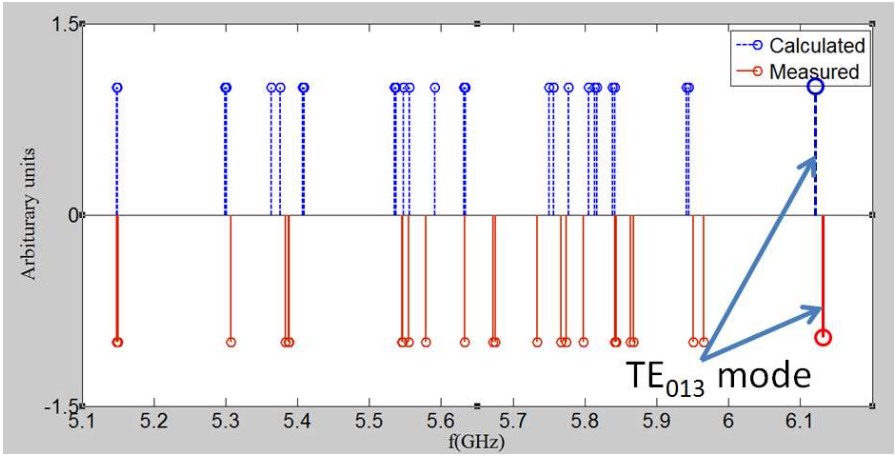

(c) 5-6.2 GHz

Figure 4.5: Resonating modes found by s11 parameters measurements compared with O3P simulations.

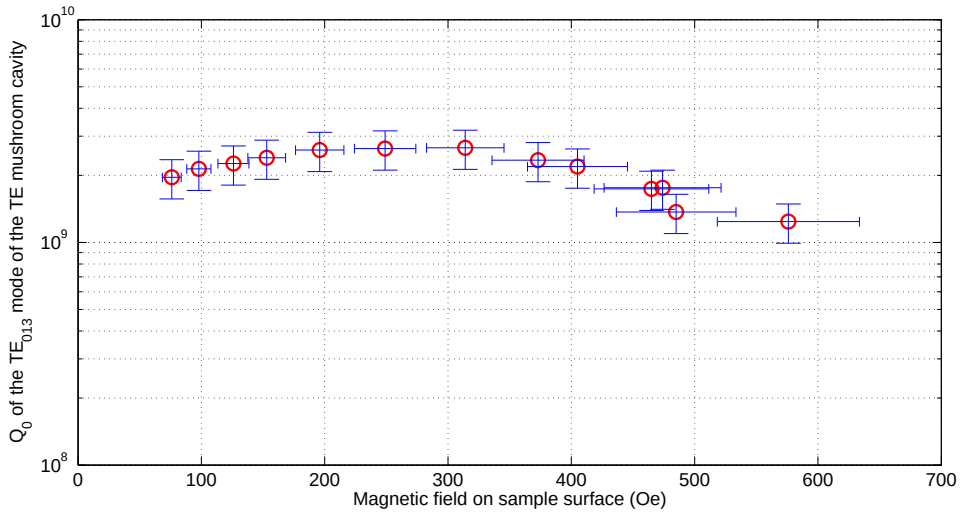

Figure 4.6: TE mushroom cavity quality factor Q_0 of mode TE_{013} versus maximum magnetic field on the sample. The uncertainty in measured field is ± 10 % and the uncertainty in measured Q_0 is ± 20 %.

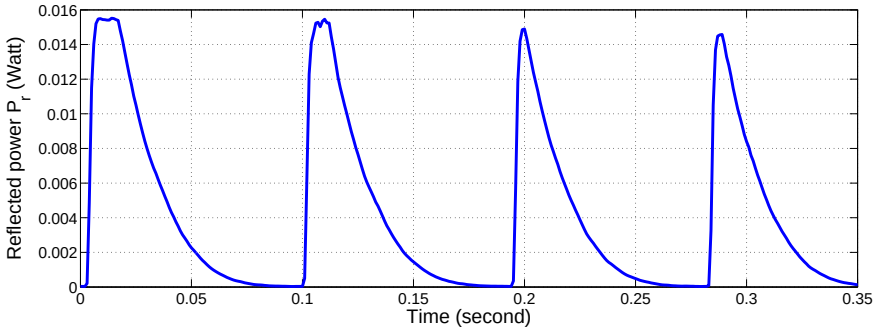

Figure 4.7: Reflected power trace when the TE mushroom cavity operated in the TE_{013} mode quenched repeatedly.

The intrinsic quality factor Q_0 of the TE_{013} mode of the TE mushroom cavity is dominated by residual losses, which as in the case of the TE pillbox cavity are likely coming from rf losses in the normal conducting coupler.

The electromagnetic simulation of the rf input coupler design in section 3.3.1 shows less rf heating due to the normal conducting coupler hook tip compared with the rf measurements. It may be that the real input coupler hook has a smaller loop area that produces less power coupling at the same penetration depth inside the input coupler tube. Therefore in order to create enough power coupling, the normal conducting hook was deeper inside the cavity and caused extra rf losses. The coupler losses will be decreased by a redesign of the input coupler in the near future.

The suspected TE_{012} mode had a very low quality factor. In addition, the coupling of the input coupler to this mode was found to be much stronger then expected based on initial simulations, and showed some nonmonotonic behavior with coupler position; see Fig. 4.8. Improved simulations of the coupler region revealed that the non propagating TE_{012} mode is mixing to a propagating mode in the wider section of the coupling tube, thereby significantly increasing the fields at the input coupler hook, which is both increasing the coupling of the coupler as well as the rf losses at the input coupler. These losses are then responsible for the overall low quality factor of the TE_{012} mode. In a future redesign of the cavity, the coupler part will be narrowed down to avoid this mixing of modes in the coupler region.

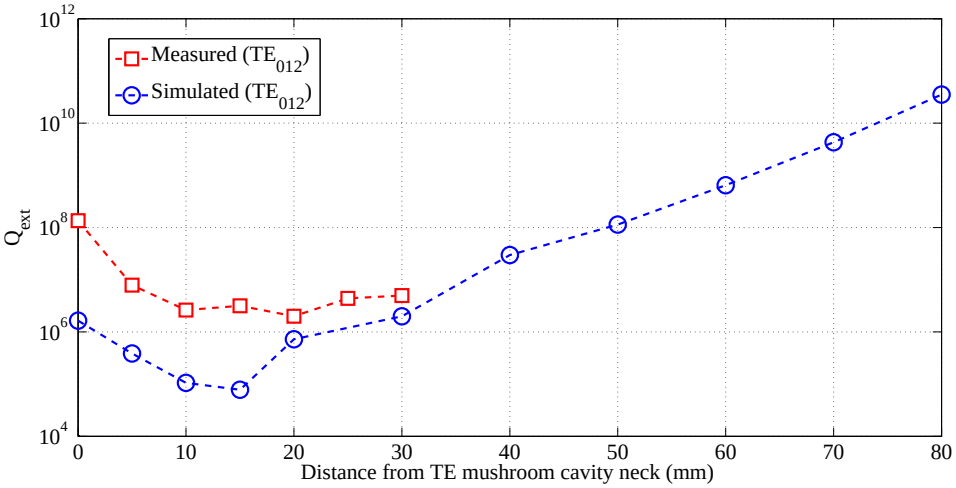

Figure 4.8: Input coupling Q_{ext} changes with coupler position for the TE_{012} mode in the mushroom cavity.

4.4 Thermal feedback analysis and ways to improve maximum field on sample

The TE mushroom cavity and the TE pillbox cavity both quenched at a maximum surface magnetic field of about 600 Oe for resonating modes of 6 GHz. Here we present a simple thermal feedback model trying to explain why the cavities both quenched at this field level. Also several methods to improve the maximum magnetic field in the sample host cavities are drawn from the analysis.

Although the shape of srf cavities can be complex, the cavity wall can be modeled locally as an infinite long flat slab of thickness d. This turns the heat transport calculation into a one-dimensional problem. As shown in Fig. 4.9, we take the coordinate z to be the vertical distance from the top (interior) surface of the cavity. Above this surface is the vacuum which carries the rf field. The

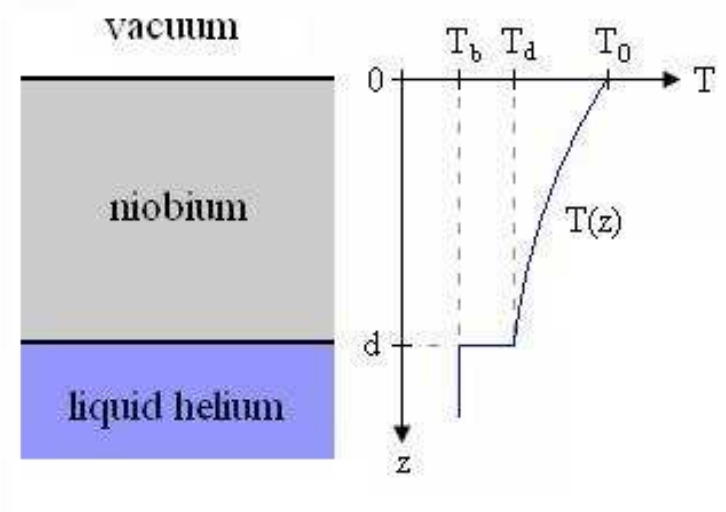

Figure 4.9: Schematic of the model of the cavity wall as an infinite slab of niobium. Above $z = 0$ is the vacuum rf field side. Below $z = d$ is the liquid helium bath.

bottom (exterior) surface of the cavity is located at $z = d$, and below this is the liquid helium bath. In this configuration, the temperature distribution within the cavity wall can be specified by a function $T(z)$. For $0 < z < d$, we expect the steady-state temperature distribution $T(z)$ to satisfy the differential equation

$$\frac{d}{dz}\left[\kappa(T)\frac{dT}{dz}\right] = 0 \tag{4.7}$$

where $\kappa(T)$ is the temperature-dependent thermal conductivity. The quantity $q \equiv -\kappa(T)\frac{dT}{dz}$ is the heat flux (power per unit area) in the z-direction; this relationship essentially defines thermal conductivity. Thus, Eqn. 4.7 simply expresses the condition that the heat flux q must be constant throughout the thickness of the wall, in accordance with the fact that no heat is created or absorbed within the wall in the steady state.

Eqn. 4.7 is a second-order differential equation, so two boundary conditions are required to find a unique solution. The first of these can be found by equat-

ing the heat flux $q(0)$ at the rf surface to the rate at which heat is being produced at the surface. The mechanism of heat production is essentially Joule heating, caused by surface currents induced by the rf magnetic field. The power dissipated per unit area can be expressed as $q = \frac{1}{2}R_s(T_0)H^2$ where H is the peak surface magnetic field, and R_s is the surface resistance, which, as indicated, is a function of the temperature $T_0 \equiv T(z = 0)$ at the rf surface. Altogether, the boundary condition at $z = 0$ reads

$$-\kappa(T_0)\frac{dT}{dz}\bigg|_{z=0} = \frac{1}{2}R_s(T_0)H^2. \tag{4.8}$$

The second boundary condition involves the Kapitza conductance of the niobium-liquid helium interface. When heat flows across an interface between superfluid helium and a metallic solid, there is a discontinuity in temperature at the interface. It has been found that the temperature difference is related to the heat flux q across the surface by $q = (T_d - T_b)H_k(T_d, T_b)$ [1], where T_d is the temperature of the metal at the interface, T_b is the temperature of the superfluid helium bath, and the function H_k, known as the Kapitza conductance, is determined by the nature of the metallic surface. From this, the second boundary condition can be written as

$$-\kappa(T_d)\frac{dT}{dz}\bigg|_{z=d} = (T_d - T_b)H_k(T_d, T_b) \tag{4.9}$$

Together, Eqns. 4.7, 4.8, and 4.9 will render a unique solution for $T(z)$, given the material functions $\kappa(T)$, $R_s(T)$, and $H_k(T_d, T_b)$, the bath temperature T_b, and the magnetic field magnitude H. One can obtain a numerical solution to the heat flow equations by dividing the niobium slab into a series of small layers and turning the differential equations above into a set of finite-difference equations. We can take the slab of thickness d to be divided into N layers of thickness

$\Delta z = d/N$ and label them with the integers $i = 0, 1, 2, ...N-2, N-1$. We can take the temperature T_i in layer i to be constant throughout the layer. Then, differential equation 4.7 becomes

$$\frac{d}{dz}\left[\kappa(T)\frac{dT}{dz}\right]_i = \frac{1}{\Delta z}\left[\kappa_i\frac{T_{i+1}-T_i}{\Delta z} - \kappa_{i-1}\frac{T_i - T_{i-1}}{\Delta z}\right] \tag{4.10}$$

where κ_i is the thermal conductivity between layers i and $i+1$ and is found by evaluating $\kappa(T)$ at the average temperature of those two layers $\kappa_i = \kappa(\frac{T_i+T_{i+1}}{2})$. Similarly, the boundary condition eq. 4.8 and 4.9 can be rewritten as

$$-\kappa(T_0)\frac{dT}{dz}\bigg|_{z=0} = -\kappa_0\frac{T_1 - T_0}{\Delta z} = \frac{1}{2}R_s(T_0)H^2 \tag{4.11}$$

$$-\kappa(T_d)\frac{dT}{dz}\bigg|_{z=d} = -\kappa_{N-2}\frac{T_{N-1} - T_{N-2}}{\Delta z} = (T_{N-1} - T_b)H_k(T_{N-1}, T_b) \tag{4.12}$$

These equations can be rearranged to yield

$$T_0 = \frac{R_s(T_0)H^2\Delta z/2 + \kappa_0 T_1}{\kappa_0} \tag{4.13}$$

$$T_i = \frac{\kappa_{i-1}T_{i-1} + \kappa_i T_{i+1}}{\kappa_{i-1} + \kappa_i} \tag{4.14}$$

$$T_{N-1} = \frac{\kappa_{N-2}T_{N-2} + H_k(T_{N-1}, T_b)\Delta z T_b}{\kappa_{N-2} + H_k\Delta z} \tag{4.15}$$

Here, Eqn. 4.14 applies for $1 \geq i \geq N-2$. Now, even though the temperatures on the left hand sides of the above equations also appear on the right hand sides of these equations, these N equations can be used to define a recursion relation on the set of T_i. Given an initial set of T_i, one can evaluate the right hand sides of the above equations using this set and thus obtain a new set of T_i through these equations. If this process is repeated recursively and the values of κ_i are updated each time, the set of T_i will converge to a numerical solution of the original differential equation.

Table 4.1: Thermal parameters for TE sample host cavities

Cavity frequency f	6 GHz
Residual resistance R_{res}	10 nΩ
Helium bath temperature T_b	1.6 K
Wall thickness d	3 mm
RRR	300

For the niobium thermal conductivity $\kappa(T)$, an analytic expression presented by Koechlin and Bonin is used [32]. The expression involves parameters of the temperature T, the residual resistivity ratio RRR, and the electron mean free path l. For Kapitza conductance H_k, three different forms are used, each obtains from fits to experimental data, and is a function of bath temperature T_b [33].

For the TE sample host cavities, the parameters listed in Tab. 4.1 were used in the above thermal model to solve the unstable threshold field, above which no stable solution is found. The result of the simulation is shown in Fig. 4.10, in which the surface temperature at the inner niobium wall is shown as a function of the applied rf magnetic surface field. At a surface magnetic field above 650 Oe, there is no stable solution of thermal equilibrium, which means that the helium bath can not cool the Joule heat generated by rf field inside. At this field, a global thermal quench is predicted by the model to occur for an rf frequency of 6 GHz, which is in very good agreement with the experimental quench field found in both the TE pillbox and the TE mushroom cavity.

By changing the material thermal parameters, the maximum stable surface field calculated by this thermal model can be increased. The following methods are predicted to be beneficial:

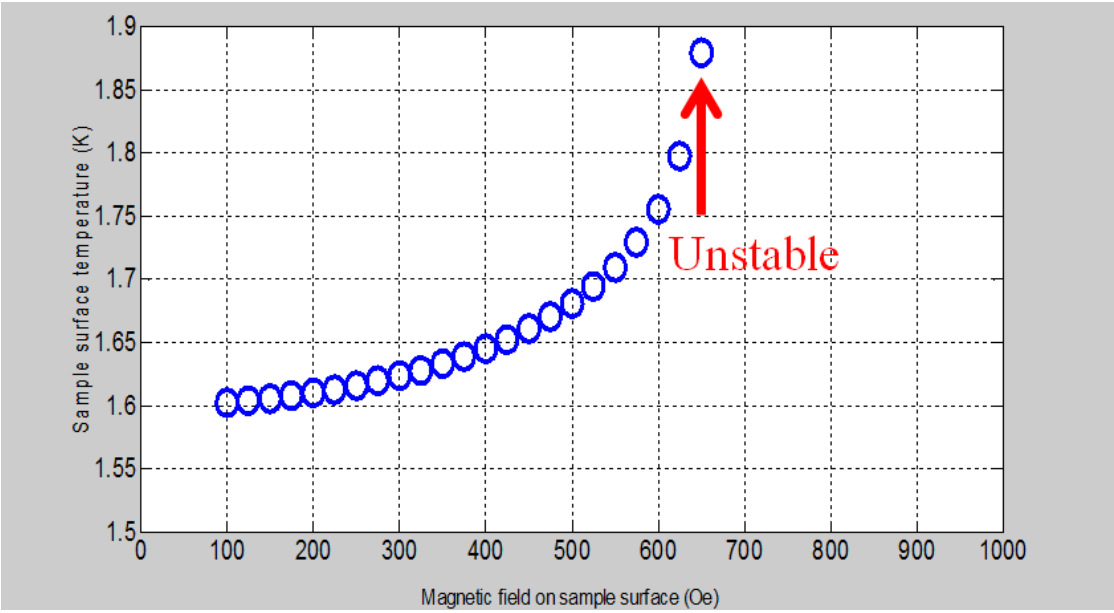

Figure 4.10: Temperature of the inner surface of a niobium wall versus applied rf magnetic surface field as predicted by the thermal model. Above 650 Oe, no stable solution is found, meaning that the cavity would quench at that surface field.

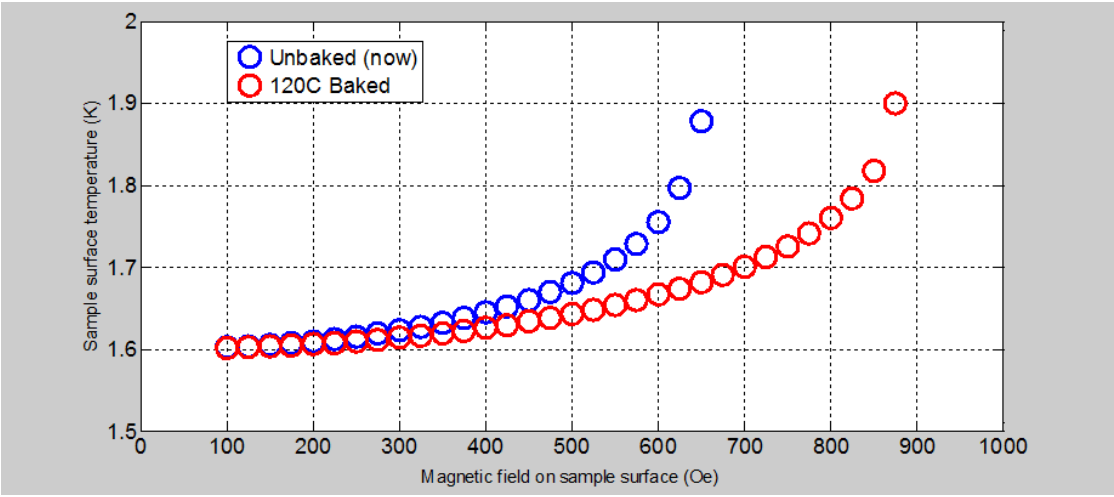

Figure 4.11: Temperature of the inner surface of a niobium wall versus applied rf magnetic surface field as predicted by the thermal model for two different BCS surface resistance conditions.

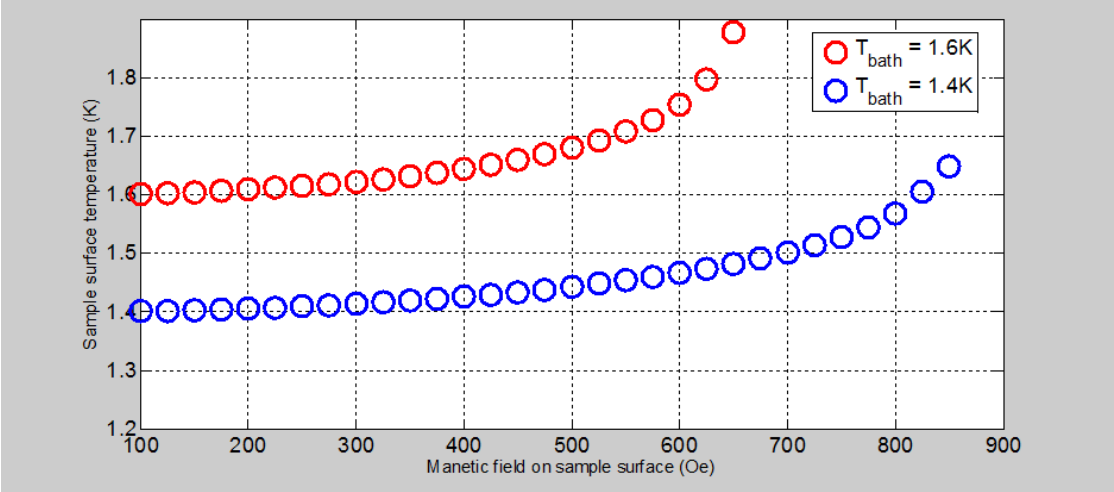

Figure 4.12: Temperature of the inner surface of a niobium wall versus applied rf magnetic surface field as predicted by the thermal model for two different bath temperatures.

- By a 120 °C bake of the cavity, the BCS resistance can be decreased by about 50 %. Fig. 4.11 shows how the surface temperature changes with applied surface field for an unbaked and a baked cavity as predicted by the thermal model. The simulation predicts that the maximum surface field can be increased above 800 Oe by a 120 °C bake of the sample host cavity.
- By lowering the bath temperature T_0 from 1.6 K to 1.4K during rf test, the breakdown field can also be increased above 800 Oe. Fig. 4.12 shows how the simulated sample surface temperature changes with applied surface field for two different bath temperatures.
- The thermal conductivity of the host cavity niobium can be increased by purifying the material by a high temperature heat treatment with a getter material such as titanium at temperatures above 1000 °C [1];
- Operating the TE mushroom sample cavity at its lower frequency (~ 4.7

GHz) TE_{012} mode will increase the thermal breakdown field, since the BCS surface resistance increases quadratically with rf frequency. This will require lowering the rf coupler losses by using a niobium coupler inner conductor tip instead of copper.

4.5 First measurement of a Nb_3Sn flat sample by TE pillbox cavity

As a first step to characterize new material samples, a flat 3.5 inch niobium sample coated with Nb_3Sn by the vapor diffusion coating method at Cornell was tested in the TE pillbox cavity [34]. The base plate was made from a RRR 280 niobium and then treated with a 130 μm BCP prior to coating and a final HPR. It was mounted in the sample coating chamber and degassed at 200 °C for one day to minimize potential RRR degradation. The coating via the vapor diffusion process took approximately 12 hours, including ramping up the temperature to the coating temperature of 1100 °C. A witness sample coated at the same time showed the desired stoichiometry under EDX analysis. After a final HPR, the Nb_3Sn sample was assembled in the TE pillbox cavity and a T-map system was assembled to the highest field region of the sample. The sample plate can be seen in Fig. 4.13.

Previous tests of Nb_3Sn indicate that temperature gradients over the surface of the cavity during the cool down process may create thermocurrents that cause increased surface resistance [35]. Therefore a slow cool down was performed and the temperature gradient across the sample was recorded by temperature sensors at the center and at the edge of the sample. The gradient did not exceed

Figure 4.13: Nb Sample plate before (left) and after (right) Nb_3Sn coating [34].

0.2 K for the cool down through the Nb_3Sn transition at about 18 K, as shown in Fig. 4.14. Compared to the slow cooling rate of 1 K / 6 min in the transition temperature range suggested before [35], our cooling rate is well acceptable.

After the cool down process, the TE pillbox cavity with Nb_3Sn sample plate was tested at 1.6 K. Fig. 4.15 shows the cavity quality factor Q_0 versus magnetic field at the Nb_3Sn sample surface. The sample reached above 250 Oe with an approximate constant combined quality factor of about 4×10^8 for the host cavity with the Nb_3Sn sample plate. Unfortunately, during the test, the T-map did not give useable signals due to rf heating of the temperature sensors by rf power leaked from the rf drive power cable to the rf input coupler. Nevertheless, assuming that the losses of the TE pillbox cavity itself, i.e. without the sample plate, does not change from test to test, an estimation of the average surface resistance of the Nb_3Sn sample plate can be made.

During the first TE pillbox cavity test with a baseline niobium sample plate,

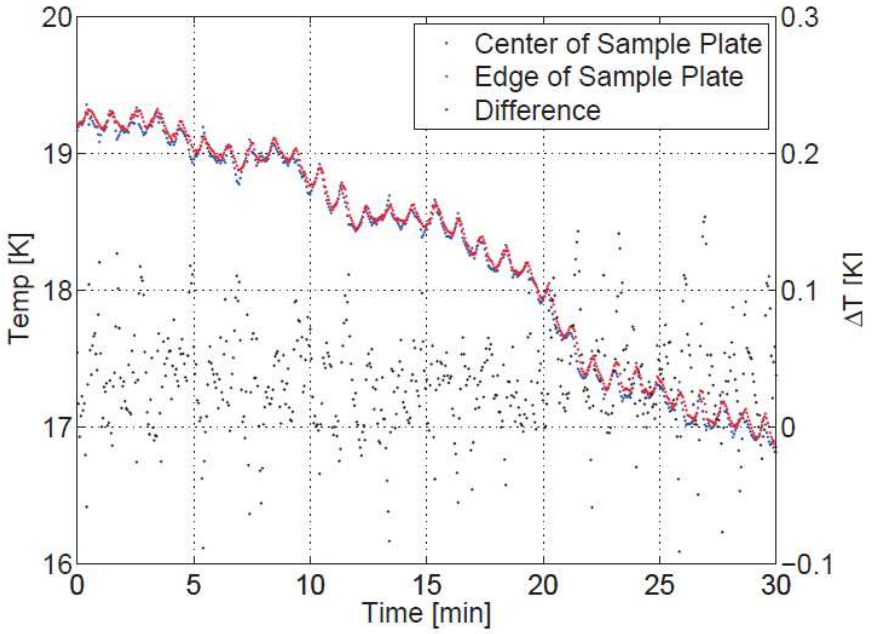

Figure 4.14: The sample was cooled slowly through the Nb_3Sn transition to avoid high residual resistance resulting from temperature gradient induced thermocurrents. The difference in temperature between the center and at the edge of the sample was monitored using Cernox sensors. [34]

the measured cavity quality factor $Q_{0,1}$ can be expressed as

$$\frac{1}{Q_{0,1}} = \frac{1}{Q_{host}} + \frac{1}{Q_{sample,Nb}} \tag{4.16}$$

where Q_{host} is the quality factor for the host cavity not including the sample plate, and $Q_{sample,Nb}$ is the quality factor corresponding to the rf losses in the sample plate.

A similar equation can be written for the test with the Nb_3Sn sample plate, where the overall cavity quality factor $Q_{0,2}$ is

$$\frac{1}{Q_{0,2}} = \frac{1}{Q_{host}} + \frac{1}{Q_{sample,Nb_3Sn}} \tag{4.17}$$

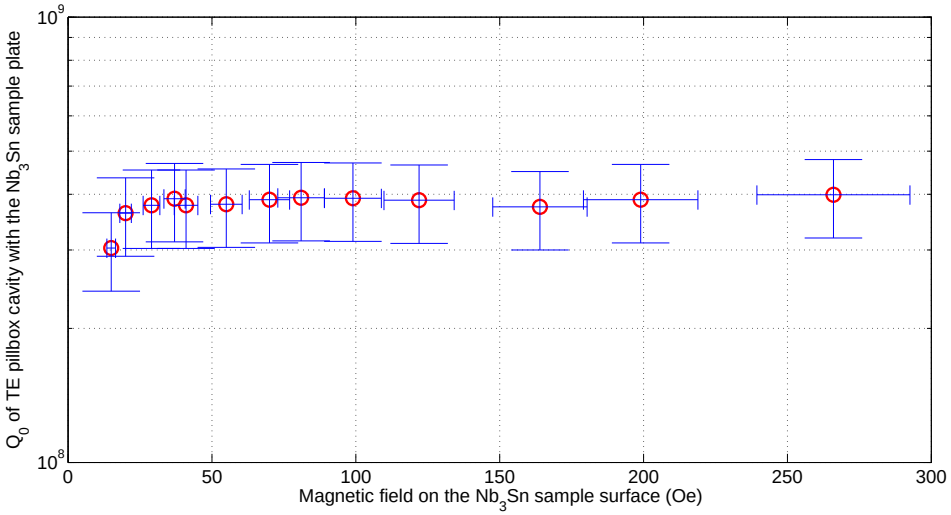

Figure 4.15: Measured quality factor Q_0 vs maximum magnetic field on the Nb_3Sn sample plate as measured in the TE pillbox cavity at 1.6 K. The uncertainty in measured field is ± 10 % and the uncertainty in measured Q_0 is ± 20 %.

A filling factor η can be define as

$$\eta = \frac{1/Q_{sample}}{1/Q_0}. \tag{4.18}$$

The baseline sample plate is made of niobium which has the same surface resistance R_s as the host cavity. Therefore, since $Q = G/R_s$, the filling factor can be written as

$$\eta = \frac{G_0}{G_{sample}} = \frac{\int_{sample} H^2 ds}{\int_{cavity} H^2 ds} \tag{4.19}$$

where G_0 and $G_{sample} = Q_{sample}/R_{s,sample}$ are the geometric factors of the overall cavity and the sample plate. For the TE pillbox cavity, G_0 is 776 Ω, and G_0 is 2587 Ω. For the TE pillbox cavity, this then gives 0.3 for the filling factor η. With Eqn. 4.18, 4.17 and 4.19, the average surface resistance of the Nb_3Sn sample R_{s,Nb_3Sn} can be obtained from

$$R_{s,Nb_3Sn} = \frac{G_0}{\eta}\left(\frac{1}{Q_{0,2}} - \frac{1}{Q_{0,1}}\right) + \frac{G_0}{Q_{0,1}}. \tag{4.20}$$

Using $Q_{0,1}$ of 6×10^9 from the baseline test of the TE pillbox cavity (see chapter 4.2), $Q_{0,2}$ of 4×10^8 for the test with the Nb_3Sn sample plate, the average surface resistance R_{s,Nb_3Sn} of this Nb_3Sn sample is about 750 nΩ. The BCS resistance of Nb_3Sn at 1.6 K and 6 GHz is of the order of nΩ. The measured average resistance of this Nb_3Sn sample is much higher than the BCS value even though the T_c of the sample plate is close to the optimum value of 18 K as measured previously [34]. This means that the residual resistance of this Nb_3Sn sample is at least above 740 nΩ. The source of high residual resistance is likely residual tin left on the surface of the sample plate because no chemistry was done after the coating process.

4.6 Conclusions

The TE pillbox cavity reaches 450 Oe (45 mT) on the sample plate surface with a highest quality factor Q_0 of 6×10^9. The TE mushroom cavity reaches 600 Oe (60 mT) on the sample plate surface with a highest quality factor of 3×10^9. The Q_0 is limited by rf losses in the rf input coupler. The rf losses can be decreased by a redesign of the rf input coupler either by enlarge the input coupler hook area or by makeing it superconducting (use niobium material). The highest magnetic field is limited by global thermal instability which can be improved by a 120 °C bake, lowering rf test bath temperature to 1.4 K, and a high temperature furnace treatment. The sensitivity in surface resistance using a T-map is of the order of 1 nΩ. Fig. 4.16 compares the performance of previous sample host cavities with the performance of our TE sample host cavities. The maximum magnetic field achieved on the sample surface and the sensitivity of surface resistance are both plotted. Compared with other TE sample host cavities ever

existed in srf research history, both the TE pillbox and the TE mushroom cavity have achieved maximum surface magnetic fields on the samples among the highest values ever reached in this type of cavity, while providing good surface resistance sensitivity at the same time. The cavities are now ready for detailed studies of niobium and other new rf superconductors, and that this work has started with the measurement of Nb_3Sn discussed in section 4.5.

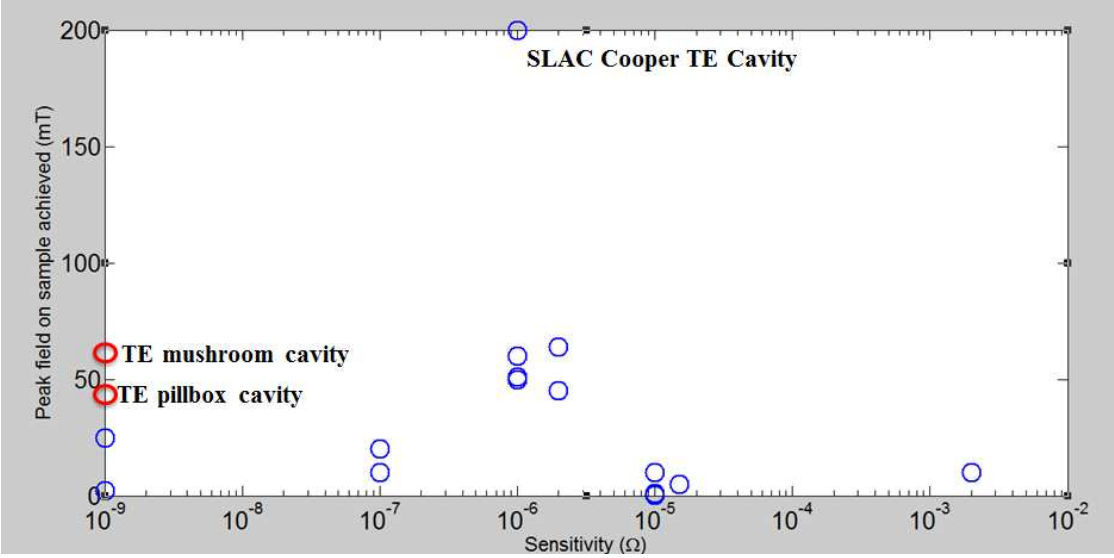

Figure 4.16: Performance of the TE sample host cavities compared to the performance of other sample host cavities in history. High peak fields and good surface resistance sensitivity (small values on the horizontal axis) are desirable.

CHAPTER 5

PIT CAVITY EXPERIMENTAL RESULTS

5.1 Introduction

After fabrication, the cavity with the 30 drilled pits of various radii received a 120 μm BCP, was high pressure water rinsed and dried for assembly to the test insert in a class 10 clean room, and received a final 120 C in-situ bake. In the following sections, we present the results from the rf test of the cavity, and show temperature maps taken by a large scale temperature mapping system mounted to the outside of the cavity. In the final section of this chapter, we show results from a laser confocal microscope inspection of molds taken from the pits in the cavity after the rf test. The microscope data gives important pit shape information, especially the radius r of the edge of the pits. The edge radius strongly impacts the magnetic field enhancement at the edge of the pits, and thus needs to be measured after the final BCP of the cavity to reflect the situation present during test of the cavity. Chapter 6 will compare the experimental pit results with predictions by field enhancement and ring defect models.

5.2 RF test results

Results of the rf test at 1.6 K are shown in Fig. 5.1. The cavity quenched at a maximum surface magnetic field of 550 Oe which corresponds to an accelerating field of 11 MV/m. It should be noted that the maximum surface magnetic field quoted here and Fig. 5.2 does not include the local magnetic field enhancement

by the pit. At the pit edge, the local magnetic field is significantly higher, as discussed later.

Before the quench, a mild Q-drop effect appeared above 300 Oe. There is a sudden drop in Q_0 at about 520 Oe, followed by a strong Q-slope. As we will discuss later, at this field the local, enhanced magnetic field at the first pit edge reaches the critical magnetic field and the edge starts to transition into the normal conducting state, thereby decreasing the cavity's quality factor. No x-rays were registered and thus no field emission was present during the test.

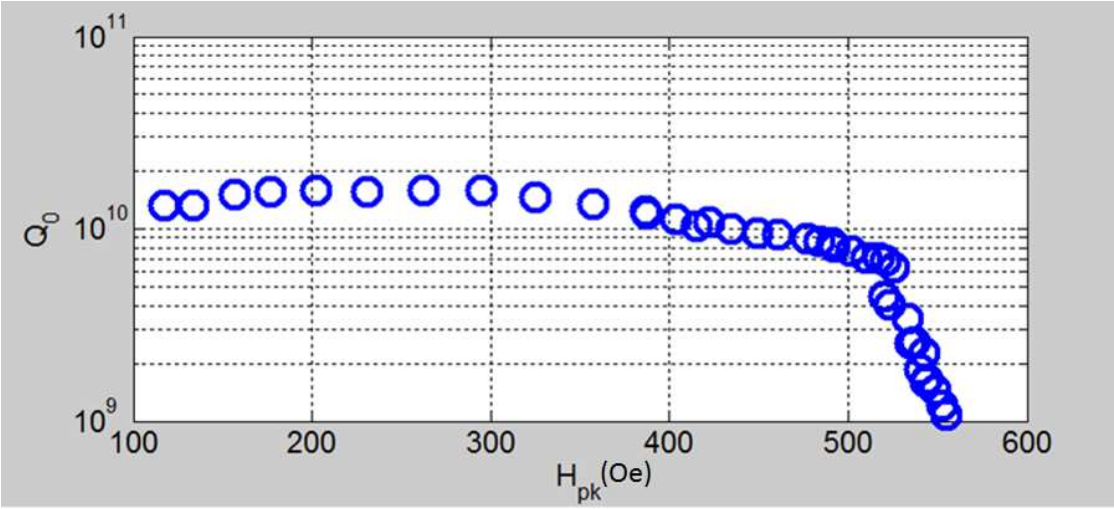

Figure 5.1: The pits cavity quality factor Q_0 versus the peak surface magnetic field H_{pk} at 1.6 K. The uncertainty in the measured field is ± 10% and ± 20% in Q_0. The surface magnetic field on the horizontal axis is the peak surface field of the cavity, not taking into account the local field enhancement by the pits.

The pits cavity was also tested at different temperatures as 2.0 K, 3.0 K and 4.2 K. The results are summarized in Fig. 5.2. The pits cavity quenches around the same peak surface magnetic field of 550 Oe corresponding to accelerating field of 11 MV/m. The quality factor differences between 1.6 K, 2.0 K, 3.0 K and

4.2 K are due to the temperature dependence of the BCS resistance.

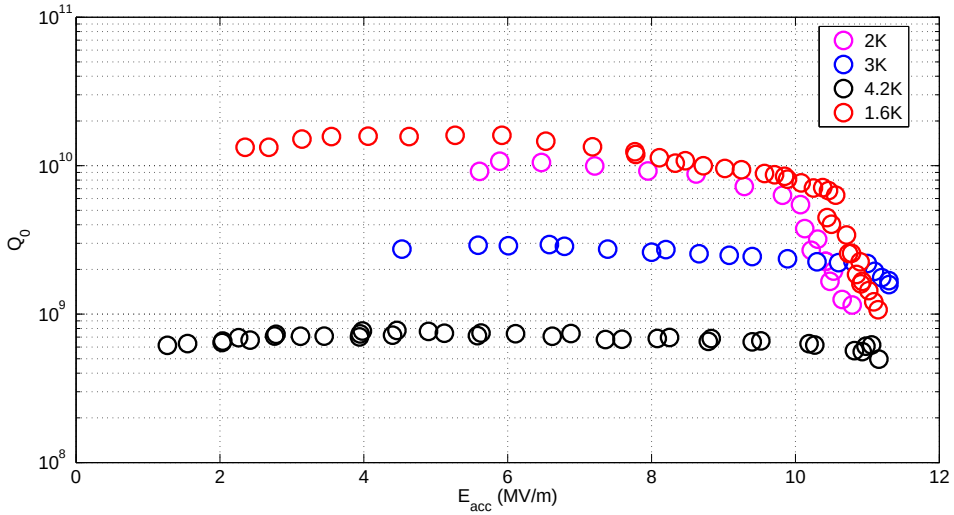

Figure 5.2: The pit cavity quality factor Q_0 versus the accelerating field E_{acc} at different temperatures. A E_{acc} of 11 MV/m corresponding to maximum surface magnetic field H_{pk} of 550 Oe. The uncertainty in the measured field is ± 10% and ± 20% in Q_0.

5.3 Temperature map results

The single-cell T-map system was used to measure the rf heating at the pits locations as function of magnetic field during the entire cavity rf test. Before temperature maps of all the thermometers were taken, three calibrated Cernox thermometers placed inside the helium bath were used to calibrate the T-map from 4.2 K to 1.6 K at an interval of 0.1 K. The calibration process was done along with slow helium cool down from 4.2 K to 1.6 K. Since the resistive element of the thermometers is carbon, which is a semiconductor, one would expects an exponential decrease of resistance with increasing temperature. After calibra-

tion, the temperature dependence of the thermometer resistance data was fitted by a polynomial function of third order,

$$\frac{1}{T} = a_n + bx_n + cx_n^2 + dx_n^3; \quad x_n = lnR_n \tag{5.1}$$

where T is the bath temperature measured by the Cernox thermometers, R_n is the resistance of carbon thermometer n, and a_n, b_n, c_n and d_n are fit parameters. Fig. 5.3 shows an example of a calibration curve for one of the temperature sensors taken during the calibration of the T-map for the pit cavity test. The voltage over the resistor is plotted instead of the resistance itself, because a fixed current source was used to drive the T-map thermometers, and the voltage over the resistors is measured by the data acquisition system.

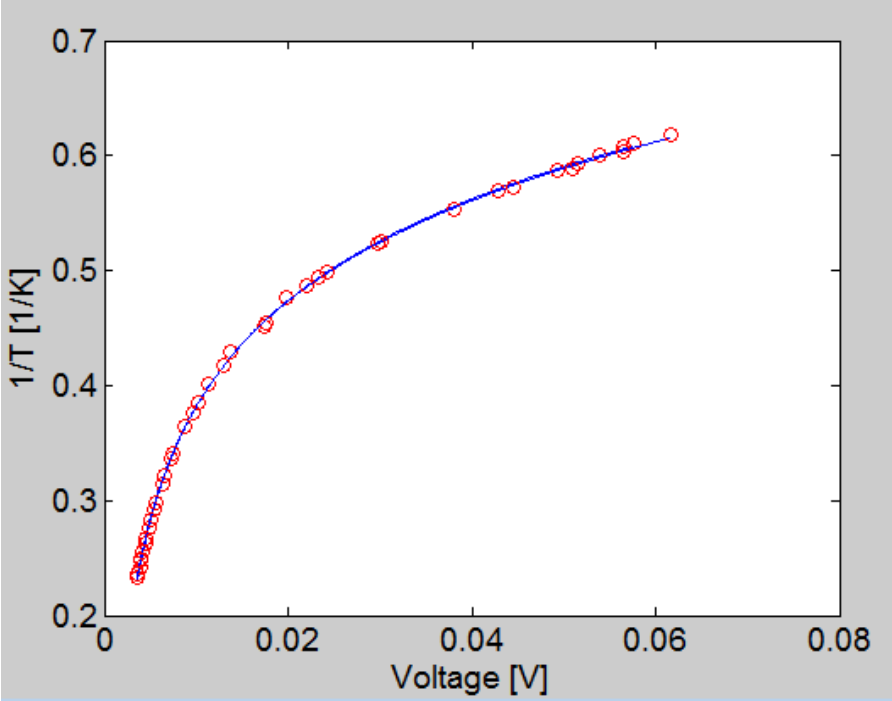

Figure 5.3: Calibration data obtained obtained for one for the temperature sensors of the T-map system during the calibration of the temperature mapping system during the test of the pit cavity. Red circles: data points. Blue curve: polynomial fit according to Eqn. 5.1.

After calibration, temperature maps were taken at different fields up to the quench field of the cavity. As an exaple, Fig. 5.4 shows one T-map taken at the cavity maximum surface magnetic field of 350 Oe. The artificial pits are located at the following positions of the T-map:

- Resistor number 6 and 12;
- Board number (2,4,6); (8,10,12); (14,16,18); (20,22,24); (26,28,30);

Here a number scheme was introduced for all 30 pits. For example, pit (2,6) (Board number 2, Resistor number 6) was named pit #1. Tab. 5.1 shows the detailed pit number scheme.

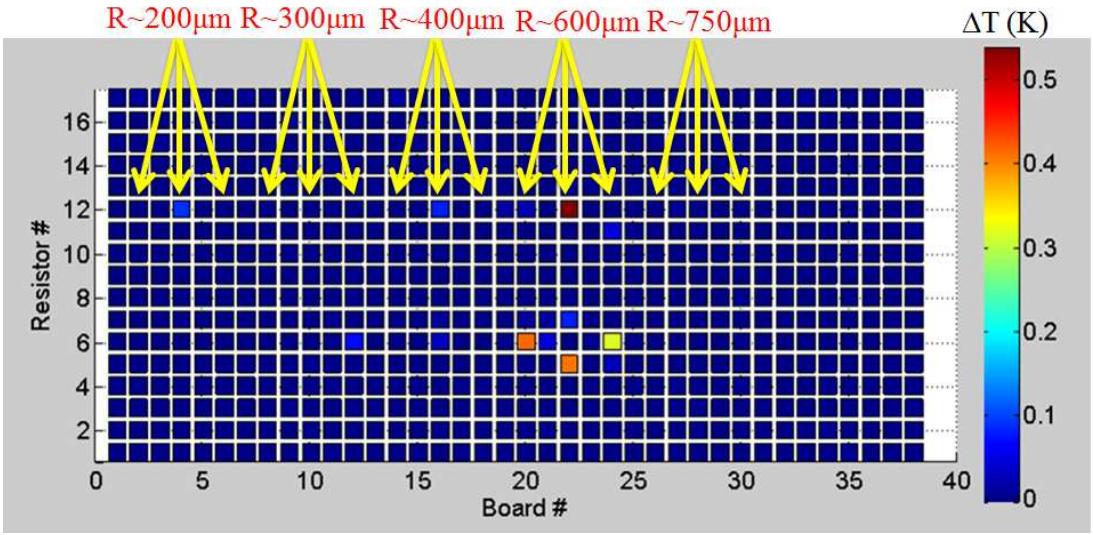

Figure 5.4: T-map taken at H_{pk} of 350 Oe. Plotted here are ΔT between rf on and off. The uncertainty in ΔT is ± 1 mK. Note that the T-map data shows good correlation between the heating pattern and the position of the pits. The row of resistors #9 is at the equator of the cavity. The 38 boards are spaced equally around the cavity.

As pits cavity maximum surface magnetic field increases, the heating pattern

Table 5.1: The number scheme of the 30 artificial pits

Board #	Resistor #	Pit #	Board #	Resistor #	Pit #
2	6	#1	16	12	#16
2	12	#2	18	12	#17
4	6	#3	18	12	#18
4	12	#4	20	6	#19
6	6	#5	20	12	#20
6	12	#6	22	6	#21
8	6	#7	22	12	#22
8	12	#8	24	6	#23
10	6	#9	24	12	#24
10	12	#10	26	6	#25
12	6	#11	26	12	#26
12	12	#12	28	6	#27
14	6	#13	28	12	#28
14	12	#14	30	6	#29
16	6	#15	30	12	#30

keeps nearly the same and the heating get stronger as can be seen in Fig. 5.5, which shows the T-map taken around 500 Oe.

The ratio between the field at the positions of the pits and the maximum surface magnetic field of the cavity, not taking into account the magnetic field enhancement by the pits, is 0.98 as found by CLANS calculations [17].

From this T-map data, we can conclude that:

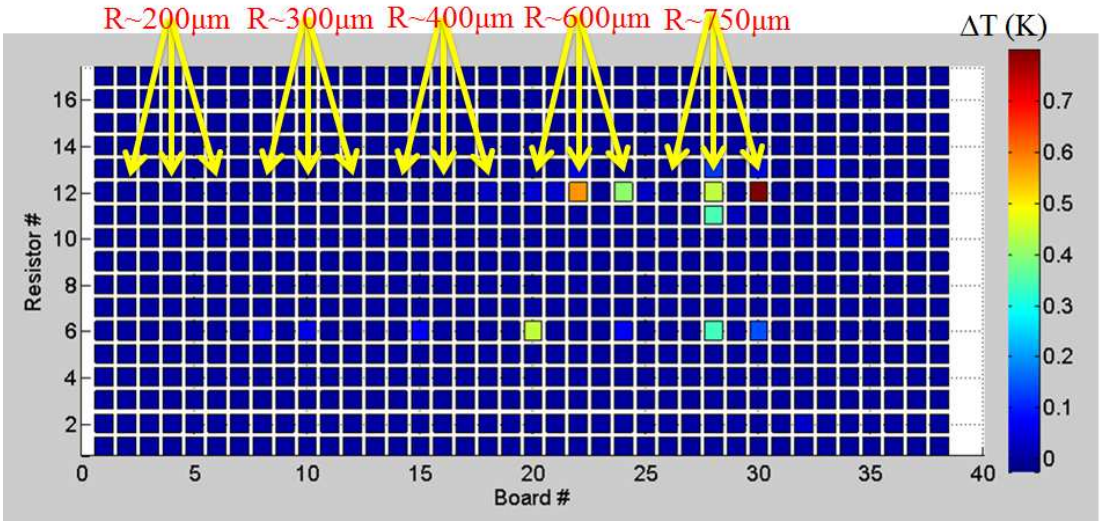

Figure 5.5: T-map taken at H_{pk} of 500 Oe. Plotted here are ΔT between rf on and off. The uncertainty in ΔT is ± 1 mK. Note the heating gets larger as compared to the heating at 350 Oe shown in Fig. 5.4. The row of resistors #9 is at the equator of the cavity. The 38 boards are spaced equally around the cavity.

- T-map heating pattern does correlate well with the pattern of the actual artificial pit positions on the inner cavity surface.
- Smaller diameter pits show smaller heating and larger diameter pits show larger heating in general. This is in agreement with the a simple magnetic field enhancement model, which predicts that the local magnetic field enhancement at the edges of the pits scales with the radis R of the pits according to $R^{1/3}$ [41], assuming that the edges of all pits have the same sharpness. Accordingly, larger pits will have higher local fields, thus larger rf heating.

Fig. 5.6, 5.7, 5.8 and 5.9 show the measured heating signals from pits with radius R = 200 μm, R = 300 μm, R = 600 μm and R = 750 μm as function of the cavity field. Some of the pits heating data are missing because of non-functional

temperature sensors. There are no effective heating signals from the six pits with the radius of $R = 400\ \mu$m.

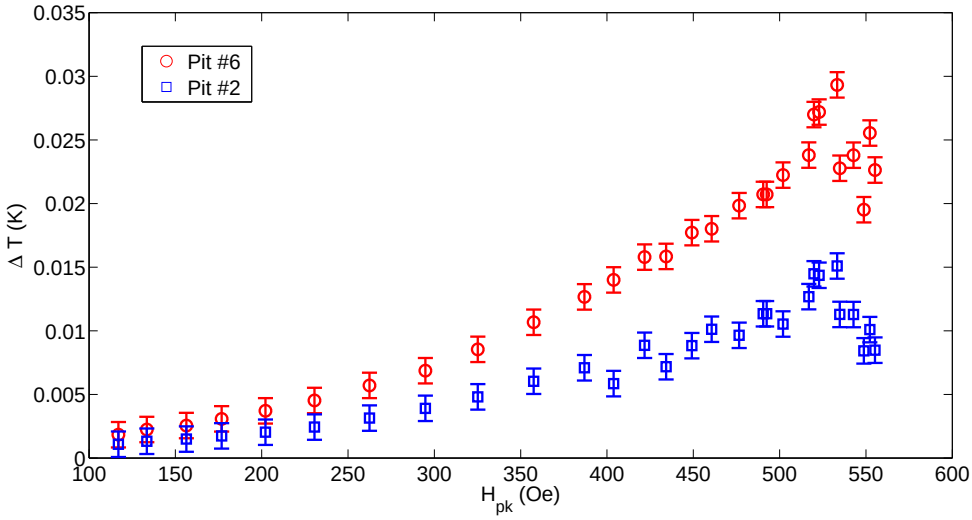

Figure 5.6: The heating of pit #2 and #6 with radius $R = 200\ \mu$m versus surface magnetic field. The heating signals from the other 4 pits with radius $R = 200\ \mu$m are missing because of non-functional temperature sensors. The surface magnetic field on the horizontal axis is the peak surface field of the cavity, not taking into account the local field enhancement by the pits.

Most of the heating signals from the pits show a non-ohmic behavior at larger fields; refer to chapter 6.4 for a detailed discussion of this field dependence of the rf surface resistance. Importantly, it can be seen from Fig. 5.8 and 5.9 that the heating signals of pit #22 and #30 show a sudden jump to the ~ 1 K range at a cavity field at ~ 545 Oe. These two pits eventually will cause a quench of the cavity at even higher field of 550 Oe.

The quench locations were found by measuring the length of time that the resistors stayed warm after the quench of the cavity [36]. The two pits # 22 and #30 were found to cause quench as shown in Fig. 5.10. Fig. 5.11 shows the heat-

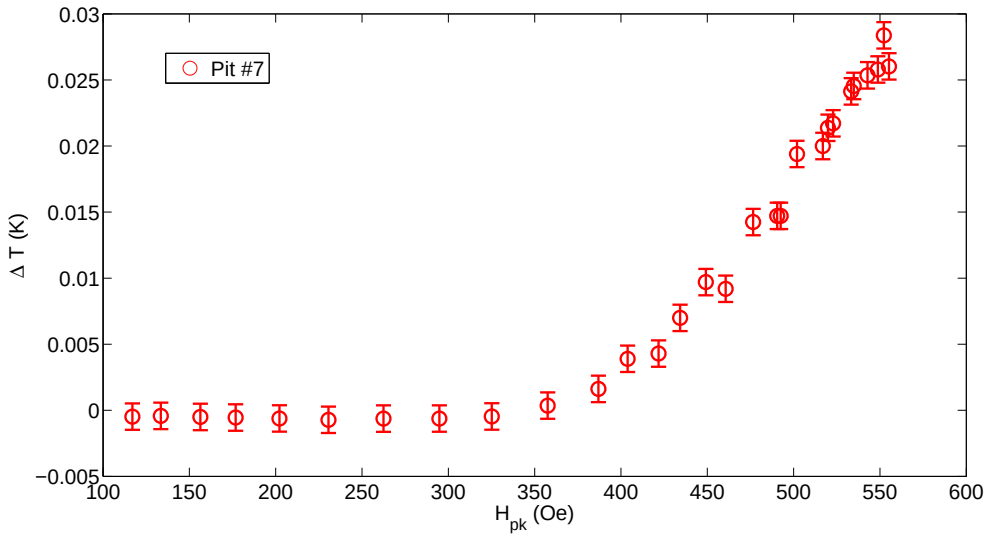

Figure 5.7: The heating of pit #7 with radius $R = 300$ μm versus surface magnetic field. The heating signals from other 5 pits with radius $R = 300$ μm are missing because of non-functional temperature sensors. The surface magnetic field on the horizontal axis is the peak surface field of the cavity, not taking into account the local field enhancement by the pits.

ing versus magnetic field of the two quench pits #22 and #30. Assuming that the thermometer efficiency is about 25% [23], the inner side of cavity actually went up to 4 K just below quench. Both of the two pits show gradual heating until the temperature suddenly jumps to about ~ 1 K at a cavity maximum magnetic field around 545 Oe, which is smaller than cavity quench field of 550 Oe. Note that both pits are among the largest radius pits, which are expected to have the largest magnetic field enhancement [41].

What likely happened here for the two quench causing pits is that the local, enhanced field at pit edge reached the critical (superheating) magnetic field at given temperature, so part of the pit turned normal conducting. Thus the T-map sensors showed a sudden increase of temperature up to ~ 1 K and also the

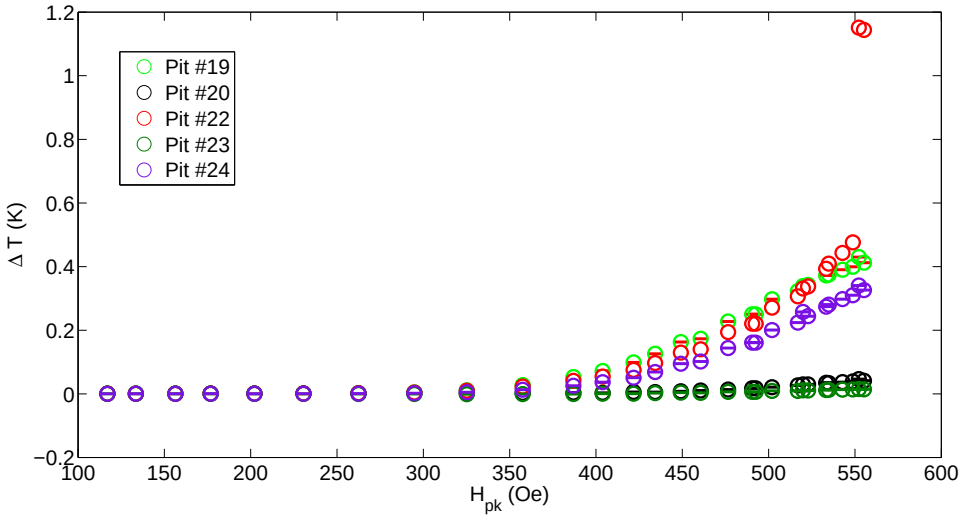

Figure 5.8: The heating of pit #19, #20, #22, #23 and #24 with radius R = 600 μm versus surface magnetic field. The heating signal of pit #21 is missing because of a non-functional temperature sensor. The surface magnetic field on the horizontal axis is the peak surface field of the cavity, not taking into account the local field enhancement by the pits.

cavity quality factor Q_0 decreased significantly. The cavity did not quench at this field and did go to a bit higher in the field before quench occurred. So it is clear that the normal conducting edge of pit is initially stable until the field is too high. A ring-type defect model in chapter 6 will be presented to study this effect in more details.

5.4 Optical inspection results

After the rf test of the pit cavity, an optical inspection was carried out for all the 30 pits inside the pit cavity. Fig. 5.12 shows one of the optical images. As can be seen from the image, the drilling process created an pit edge with a very sharp

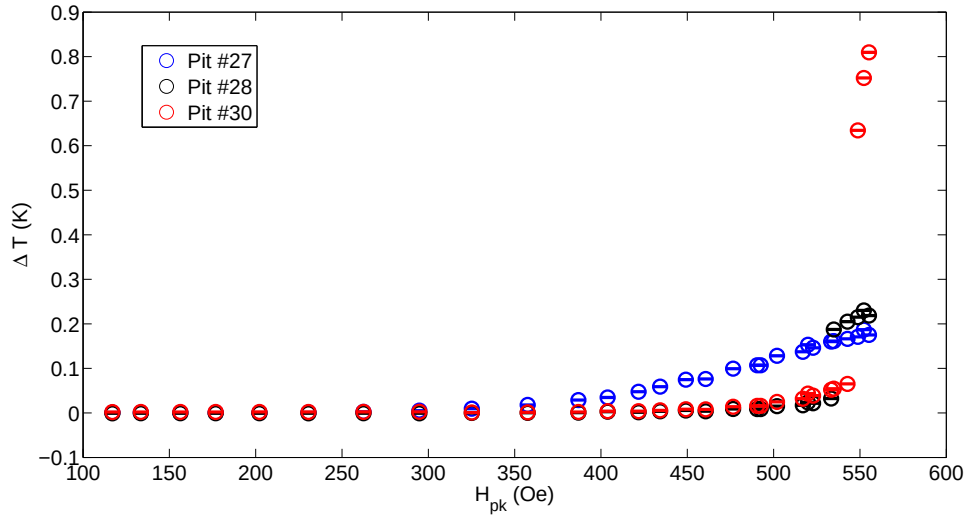

Figure 5.9: The heating of pit #27, #28 and #30 with radius $R = 750$ μm versus surface magnetic field. The heating signals from pit #25, #26 and #29 are missing because of non-functional temperature sensors. The surface magnetic field on the horizontal axis is the peak surface field of the cavity, not taking into account the local field enhancement by the pits.

corner.

5.5 Laser confocal microscopy results

In order to obtain precise values of the pit edge radius r of the individual pits, silicone replicas were made to all thirty pits. Fig. 5.13 shows the silicone solidified with string after being pulled out from the pit cavity. The replicas were found to have at least 1 μm resolution. The replicas were then examined by laser confocal microscopy to measure the sharpness of the pit edges. Fig. 5.14 shows one of the images of a pit taken by laser confocal microscope. The dark area is the pit. In the bright area, the grain structure of the niobium surface can be seen

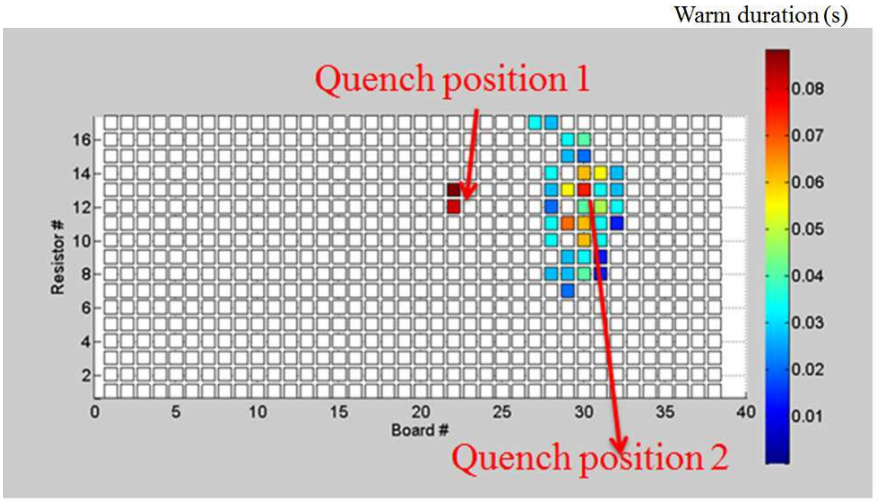

Figure 5.10: Quench locations of the pit cavity at a maximum surface magnetic field of ~ 555 Oe. The quench locations were found by measuring the length of time that the resistors in the temperature map stayed warm after the quench of the cavity. The center of the quench location was found to be pits #22 and #30.

very clearly.

Since the magnetic field is parallel to cavity equator, edges of pits perpendicular to the direction of the magnetic field show the highest fields due to magnetic field enhancement as shown in Fig. 6.6 (see chapter 6.2). We only sample the pit edge curve profiles from those sections as indicated in Fig. 5.15. Fig. 5.16 shows an typical pit edge profile. The edge of the pit radius r is determined by the smallest curvature of the edge section of the profile. For every pit, 60 profile curves are taken from the 60 cross sections at different angles inside the magnetic field enhancement area of the pit. Then the range of pit edge radius r is measured from those 60 profile curves. Also the range of pit radius R is measured from those different pit profiles inside the magnetic field enhancement region. For example, Fig. 5.17 shows the distributions of r for three pits with the largest drill bit radius of 750 μm. It can be seen that the pit #30 has the small-

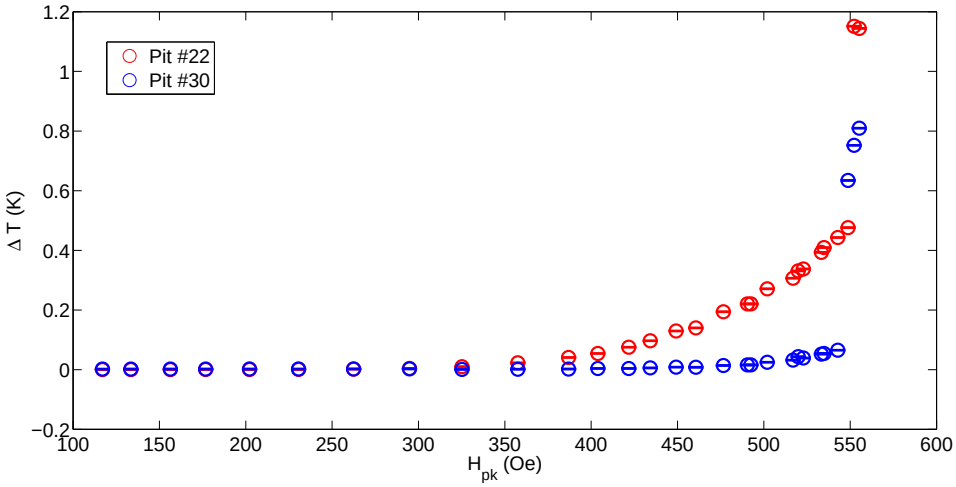

Figure 5.11: Heating of pit #22 and #30 versus the cavity maximum surface field H_{pk}. The uncertainty of measured field values is ± 10%. Notice the sudden jumps in ΔT at ~ 540 Oe, corresponding to the sudden change in Q_0 at the same field; see Fig. 5.1. The surface magnetic field on the horizontal axis is the peak surface field of the cavity, not taking into account the local field enhancement by the pits.

est average edge radius r around 10 μm. Pit (28,6) and pit (28,12) have average edge radius of 30 μm and 24 μm.

Table. 5.2 and 5.3 list the geometrical information measured by laser confocal microscopy including the range of pit radius R and the range of pit edge radius r for all 30 pits of 5 different drill sizes. The analysis of the resulting magnetic field enhancement at the pit is presented in the following chapter.

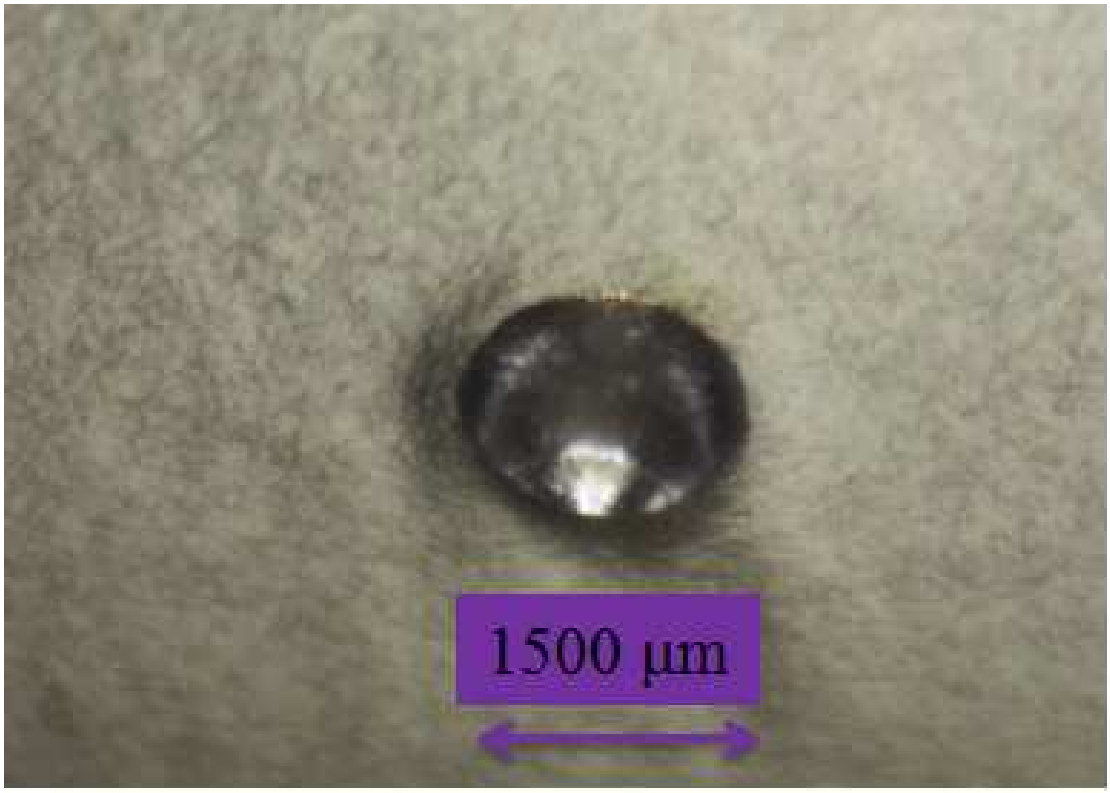

Figure 5.12: Optical inspection image of pit #30.

Figure 5.13: One silicone solidified with string after being pulled out from the pits cavity.

Figure 5.14: Image of pit #30 taken by laser confocal microscope. This pit is one of the pits causing the cavity to quench.

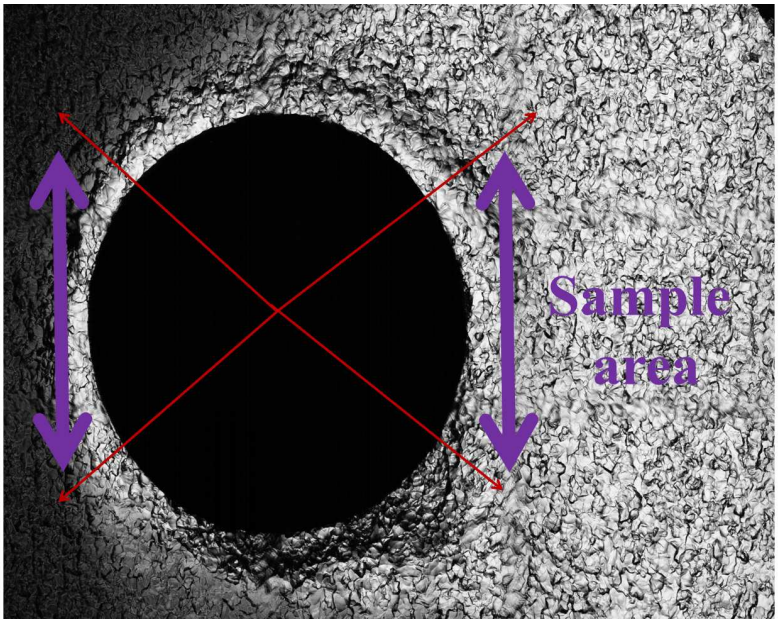

Figure 5.15: Area sampled for extracting edge profile data of the pits (Marked by double arrow).

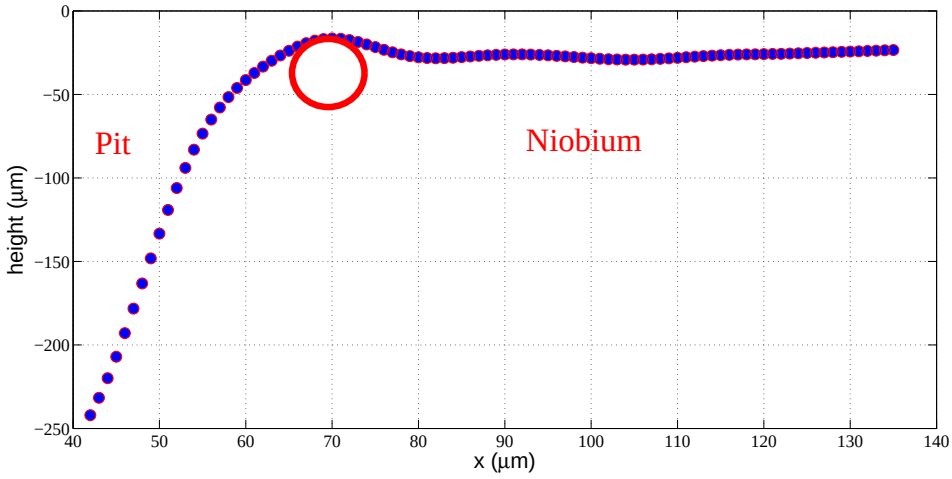

Figure 5.16: A typical pit edge curve extracted from the laser confocal microscopy image. The red circle is used to fit and obtain the edge radius r of the pit.

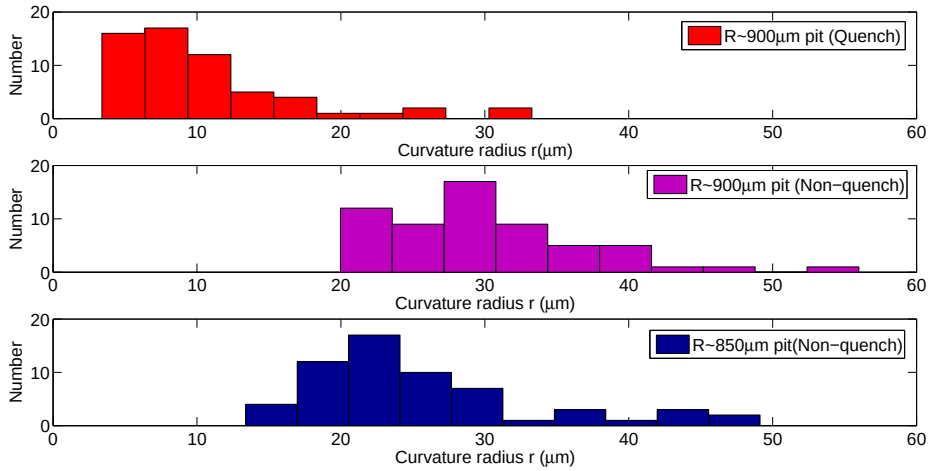

Figure 5.17: The distribution of edge radius r of three pits with nearly the same radius 750 μm. The top one is pit #30. The middle one is pit #27 and the bottom one is pit #28.

Table 5.2: The geometrical parameters of the artificial pits (I): the pits that have effective temperature readings measured by the T-map.

Pit number	Pit drill radius (μm)	Range of pit edge radius r (μm)	Range of pit radius R (μm)
#30	750	5~30	850~900
#27	750	20~55	880~900
#28	750	15~45	820~850
#23	600	30~60	520~550
#24	600	25~60	580~610
#22	600	5~45	570~610
#19	600	20~55	550~600
#20	600	35~60	570~600
#7	300	20~50	280~310
#6	200	25~55	180~210
#2	200	35~60	190~200

Table 5.3: The geometrical parameters of the artificial pits (II): the pits that do not have effective temperature readings measured by the T-map.

Pit number	Pit drill radius (μm)	Range of pit radius r (μm)	Range of pit edge radius R (μm)
#29	750	30~50	850~900
#26	750	10~45	850~870
#25	750	25~60	850~900
#21	600	25~60	600~650
#18	400	35~50	400~450
#17	400	20~35	350~400
#16	400	25~55	370~420
#15	400	20~50	400~450
#14	400	35~45	400~450
#13	400	25~40	400~420
#12	300	25~50	270~310
#11	300	20~50	290~320
#10	300	30~55	300~340
#9	300	35~60	280~320
#8	300	35~55	300~340
#5	200	20~45	200~210
#4	200	25~40	190~220
#3	200	25~50	200~220
#1	200	20~45	190~220

CHAPTER 6

NEW INSIGHTS INTO PITS BREAKDOWN AND HIGH FIELD Q-SLOPE

This chapter will first introduce the magnetic field enhancement theory, which will be applied later to the pit cavity. A ring-type defect model will be then explained. Magnetic field enhancement calculations based on geometrical information of the pits inside the pit cavity will be presented and compared to the experimental results. Finally, observations of high field Q-slope based on the heating signal of the pits will be discussed.

6.1 Magnetic field enhancement at the edge of a pit

The magnetic field enhancement effect at the sharp edge/corner of a pit as shown in Fig. 6.1 has been calculated in previous work [16], [40], [41]. The results obtained for sufficiently deep pits (depth > R) generally show that the magnetic field enhancement factor β can be expressed as [41]

$$\beta = C(\frac{r}{R})^{-1/3}, \tag{6.1}$$

where r is the radius of edge/corner, R the radius of the pit, and C is a constant of about 1.17. Accordingly, pits with larger radius or sharper edges cause a larger magnetic field enhancement.

Real pit-like defects observed in the superconducting cavities have a complex 3-dimensional shape. To obtain a realistic field enhancement factor for these pits, I used SLAC's parallel computing EM code ACE3P [38] to compute the exact surface magnetic field in the entire pit edge area. Studies have shown that Omega3P has a very accurate surface field precision compared to

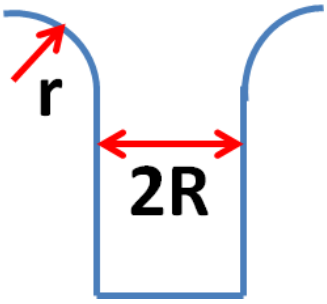

Figure 6.1: The sketch of a pit with radius R and edge radius r.

other 3-dimensional codes [42]. As a first, simple example, we have simulated a rounded pit on the axis of a pillbox cavity with the TE_{111} mode. The size of the modeled pit is small compared to the size of the cavity, which ensures that the surface field would be uniform over the area of the pit without the pit present. The pillbox cavity has a radius 100 mm, with a pit radius R = 1 mm. The simulated geometry and mesh configuration can be seen in Fig. 6.2 and Fig. 6.3.

The calculation was performed and checked with different mesh densities. As the pit edge radius r becomes smaller, the surface field calculated by Omega3P becomes more dependent on the mesh densities. Nevertheless, for sufficiently dense meshes, our calculated results agree well with the $(r/R)^{-1/3}$ dependence of the maximum surface enhanced magnetic field as shown in Fig. 6.5. An example of the calculated surface magnetic field distribution is shown in Fig. 6.4. The corresponding field enhancement factor near the edge of the pit is displayed in Fig. 6.6. An angular non-uniform field enhancement around the edge can be seen from these results, with significant field enhancement in some sections. The maximum magnetic field enhancement factor is about 2.65 which is in good agreement with the calculation results using Eqn. 6.1.

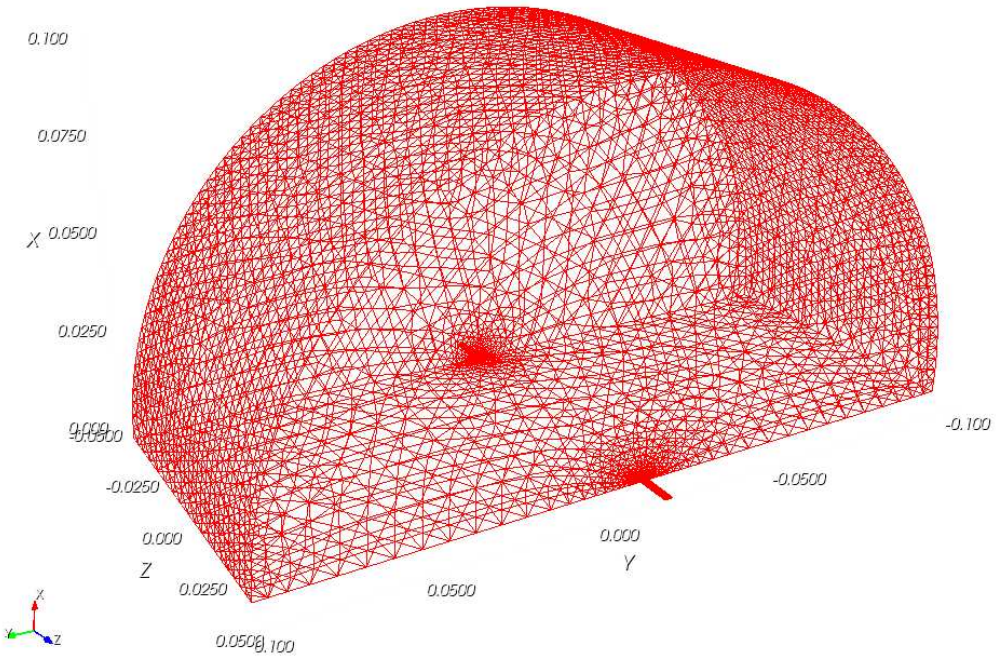

Figure 6.2: Geometry and mesh configuration used for the 3D pit magnetic field enhancement calculations.

6.2 Ring-type defect model based on magnetic field enhancement on ring edges

The phenomena of thermal magnetic breakdown has been numerically simulated over the years and is based on a thermal feedback process. Past models treated the defect as an axial-symmetric disk with its entire area becoming normal conducting when thermal breakdown happens. However, as observed in many cases, quench causing defects are correlated with pits on the surface with a sharp edge, and not disk like objects. Therefore, based on the assumption that only the edge of the pit becomes normal conducting, a 2-dimensional ring-type defect thermal program was developed. Figure. 6.7 shows the mesh configura-

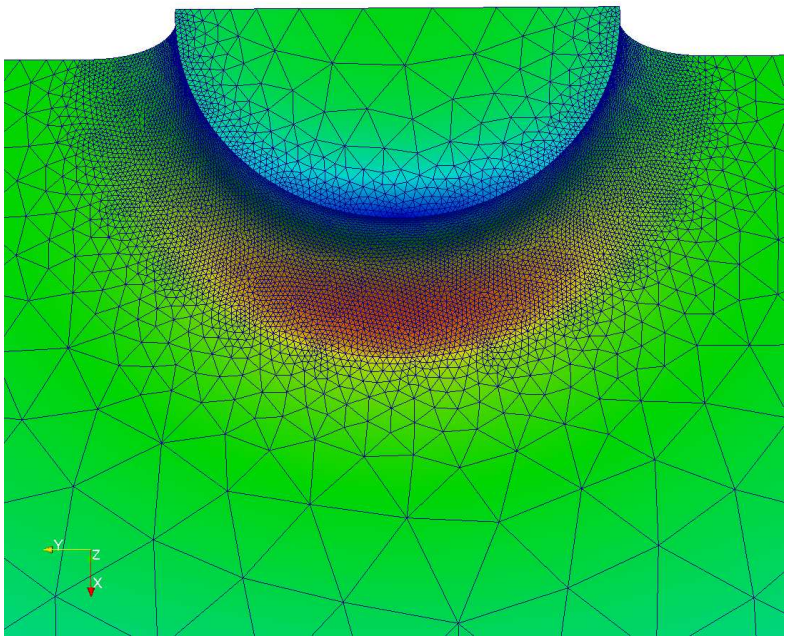

Figure 6.3: Mesh configuration at the pit used for 3D magnetic field enhancement calculations. Here R = 1 mm, r = 75 μm.

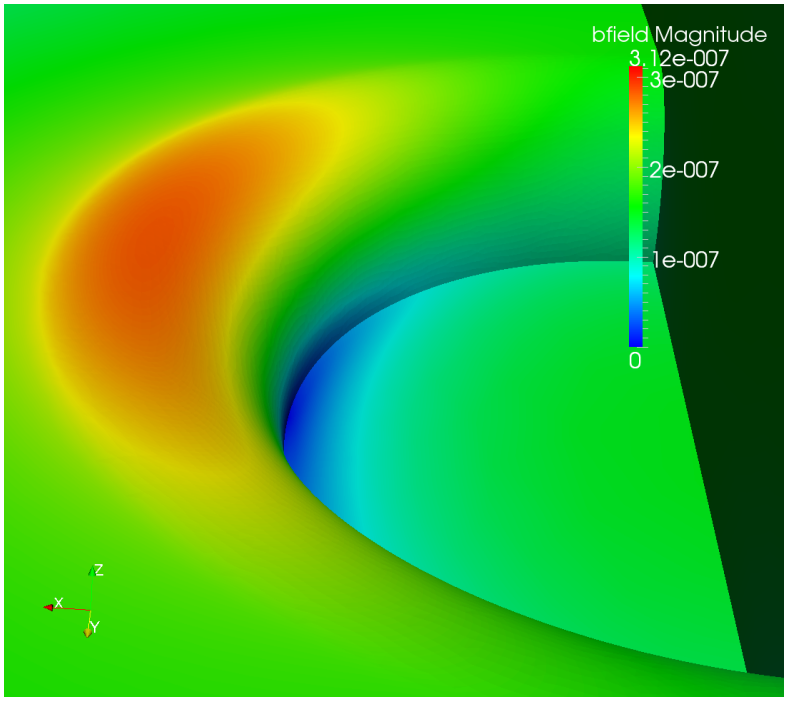

Figure 6.4: Magnetic field distribution near the pit edge. The direction of the magnetic field is in the x-direction outside of the pit.

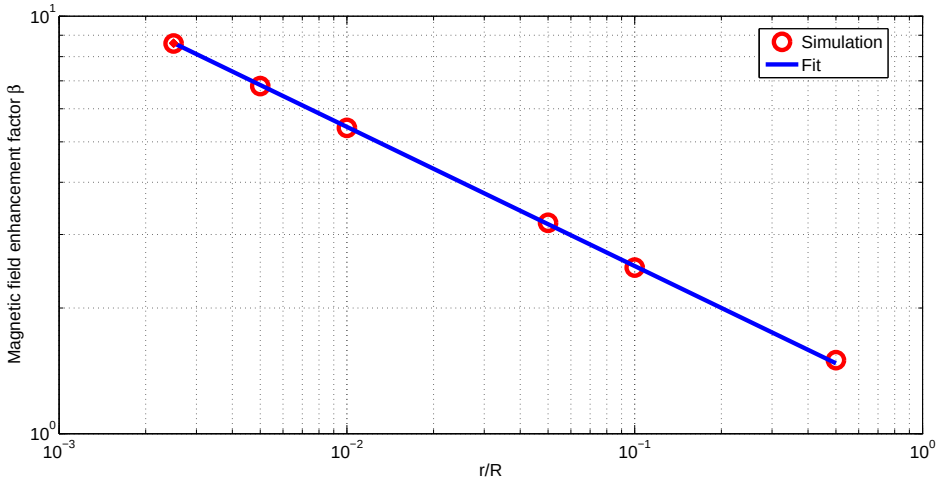

Figure 6.5: Magnetic field enhancement factor calculation by ACE3P using a 3-d model. The fit equation is $\beta = 1.17 * (r/R)^{-1/3}$.

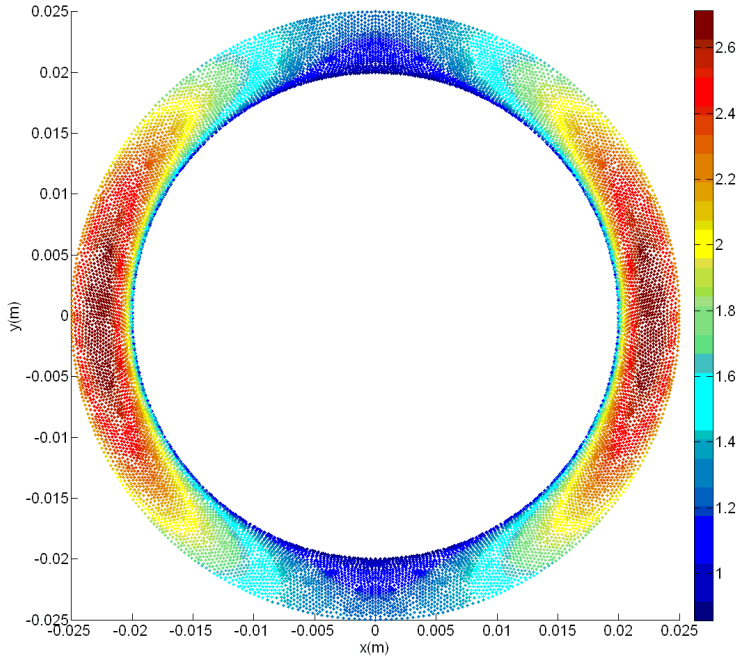

Figure 6.6: Magnetic field enhancement near the pit edge.

tion difference between a ring-type defect and a disk-type defect. The ring-type defect model is based on the same heat balance equations and boundary conditions as the disk-defect thermal model [22].

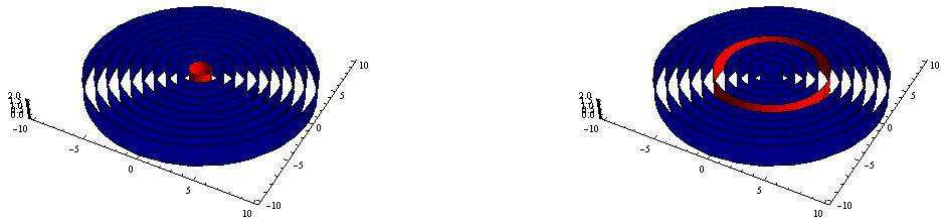

(a) Mesh configuration for a disk-type defect (b) Mesh configuration for a ring-type defect

Figure 6.7: Different mesh distributions of ring type and disk type defect models with normal conducting (red) and superconducting (blue) mesh elements.

In the ring-type defect model, the program splits a cylindrical section of the niobium wall into many circular ring-shaped mesh elements. To model the heating at the edge of the pit, in the first version of the ring defect model a normal conducting defect was located at a ring section at a certain distance from the center of the modeled niobium disk. To speed up simulations, the mesh density is higher near the defect element and lower away from it, where temperature gradients are smaller. The mesh spacing in the radial direction was chosen to increase exponentially (the distance between the i-th element to the ring-defect is proportional to e^i). The z direction (through the niobium) can also be easily meshed using an exponential function. For a selected surface field at one side of the niobium disc, the rf power is calculated based on the temperature dependent surface resistance. Given the temperature dependent thermal conductivity of niobium and Kapitza conductance between niobium and helium, the rf power produced at the surface is compared with the power emitted into the helium bath at a given iteration number. The over-relaxation method [39] is used to

estimate the $(n+1)$-th iteration from the n-th iteration. Once the two heat transfer numbers are sufficiently equal (e.g. their difference is less than 1.0×10^{-6}), thermal equilibrium is reached and a valid solution is found.

To test the ring-shape defect thermal modeling program, we have calculated the heating due to a ring-type defect and compared it to the heating by a disk defect of the same radius. The ring defect inner radius is 1 μm with a ring width of 49 μm, so that the outer radius of the ring defect becomes 50 μm. The radius of the disk defect is assumed to be 50 μm. The temperature distribution of those two cases should approximately be the same because the rf deposited power in both cases is nearly equal. Figure. 6.8 shows that the calculated temperature distribution agrees very well indeed for the two cases. In a second test of the program, a large ring-type defect with an inner radius of 5 mm and a ring width of 1 μm was simulated. The result of this simulation is shown in Fig. 6.9. The ring induced heat distribution is nearly symmetric as expected for such a large radius defect.

In the second, improved version of the ring defect model, a position dependent magnetic field enhancement (MFE) factor at the rf surface is added to better mirror the situation found in pit defects. For a first approximation, the enhancement factor is one far outside of the pit and jumps to a selected value above one at the pit edge of a given width. Inside the pit, the field enhancement factor is scaled below one because the surface magnetic field inside the pit is lower compared to the field at the flat surface outside of a pit.

Accordingly, the radius of the "ring defect" in the model is equal to the radius R of the pit, and the width of the "defect" is assumed to be equal to the radius r of the edge of the pit, where the MFE factor is high. Initially in the

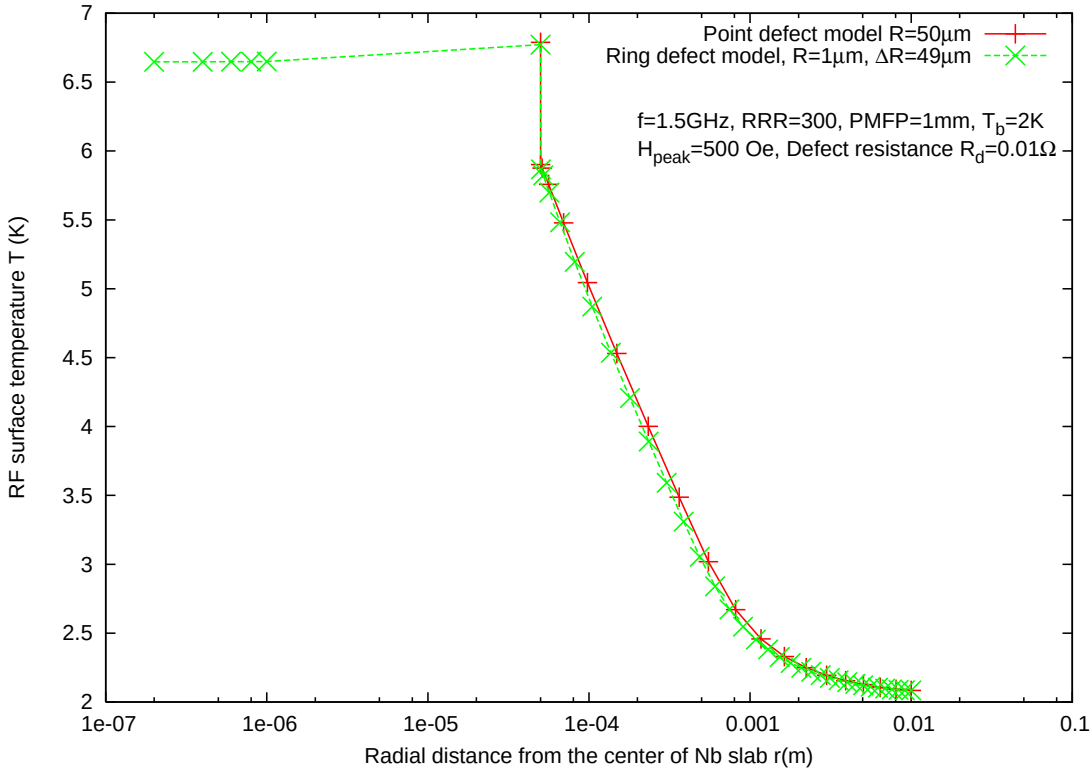

Figure 6.8: rf surface temperature distribution of a disk defect (radius = 50 μm) and of a ring defect (outer radius = 50 μm, inner radius = 1 μm). The rf deposited power is nearly identical in both cases. The rf frequency is 1.5 GHz, RRR = 300, phonon mean free path = 1 mm, bath temperature = 2 K, magnetic field =500 Oe and the normal conducting defect resistance is 10 mΩ.

model, the entire surface is assumed to be superconducting. Only when the field exceeds the superheating (critical) magnetic field at the given temperature of the niobium at a given location, that section of the surface is assumed to become normal conducting. Since an axis-symmetric mesh is used, a uniform MFE factor is assumed instead of angular dependent MFE factor along the pit edge. Nevertheless, a 3-dimensional electromagnetic code is used to obtain realistic magnetic field enhancement factors based on measured surface pit dimensions.

Simulations of pit defects of different radius R and edge width r (and thus

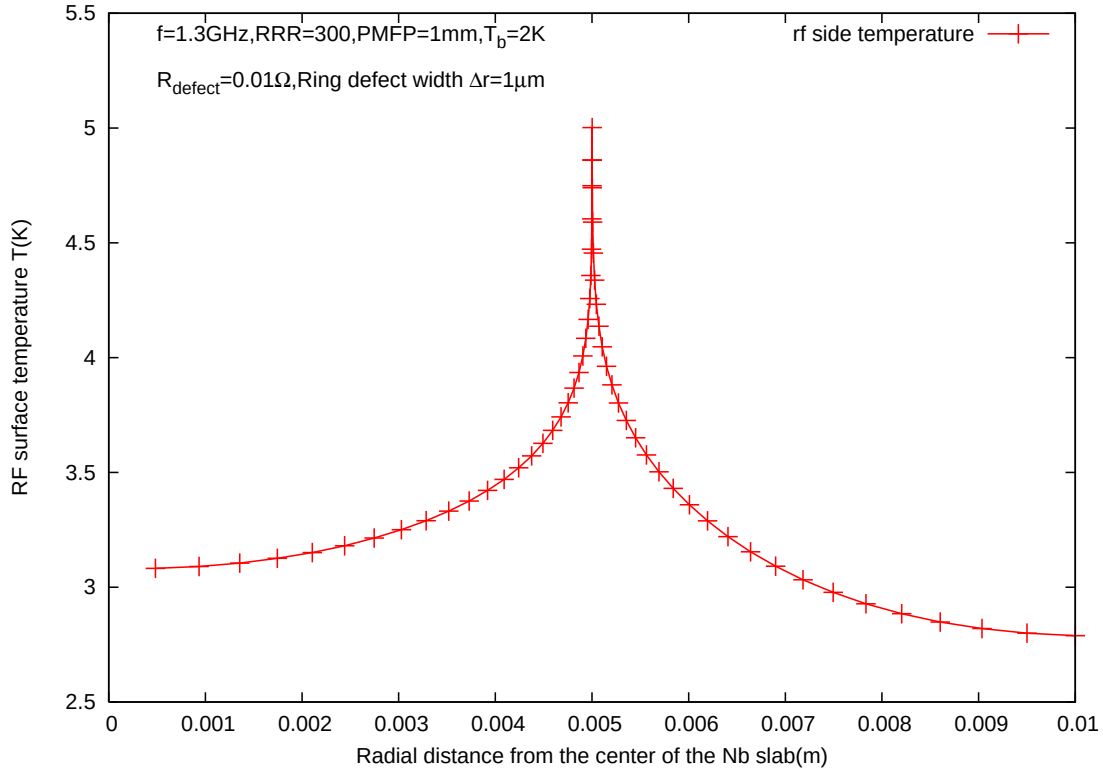

Figure 6.9: rf surface temperature distribution of a 5 mm ring-type defect with 1 μm width. The modeled niobium plate has a radius of 10 mm. The rf frequency is 1.3 GHz, RRR = 300, phonon mean free path = 1 mm, bath temperature = 2 K, magnetic field =500 Oe and the normal conducting defect resistance is 10 mΩ.

different field enhancement factor at the pit) were performed to explore the relationship between the pit geometry and the quench field. Fig. 6.10 shoes the temperature profile on the rf surface as function of radial distance from the center of the pit at a field just below quench. Clearly visible is the heating by the edge of the pit becoming normal conducting. The normal conducting resistance of niobium was taken as 10 mΩ. Future versions of the ring defect model will also take into account the temperature dependence of the normal conducting resistance. Fig. 6.11 shows a typical pre-quench temperature distribution at the cross section of the simulated heating by a pit. The rf field level (enhanced field

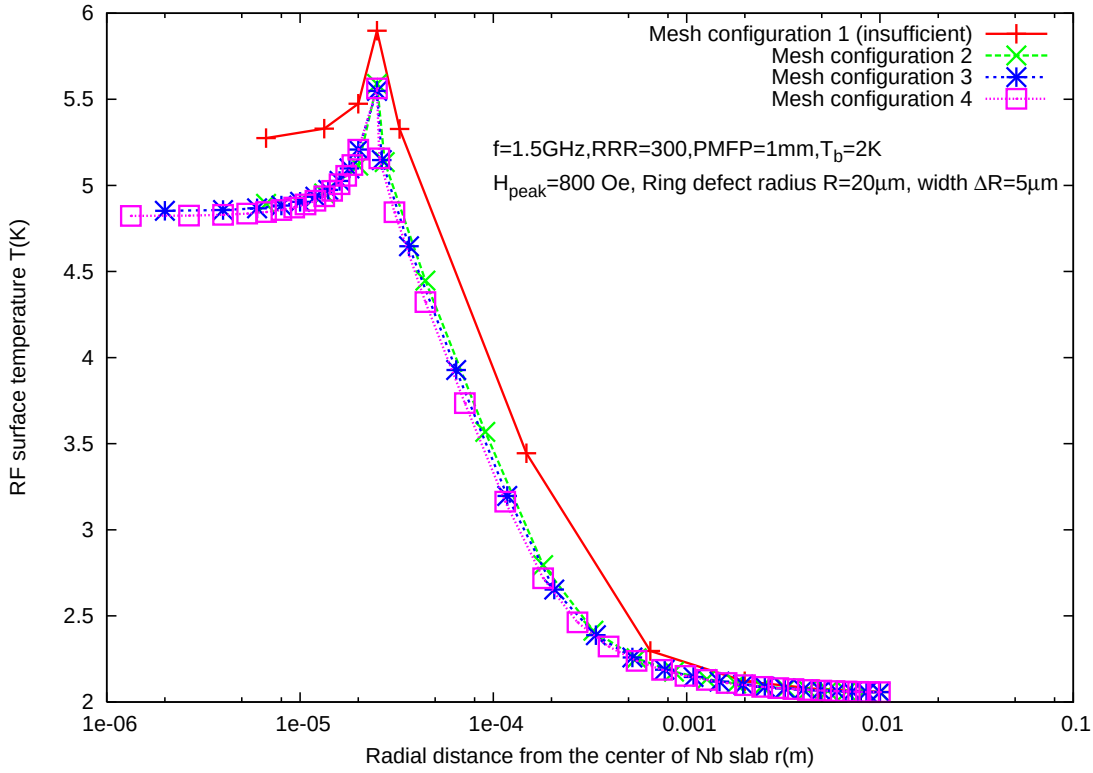

Figure 6.10: RF surface temperature distribution along the radial direction for a given ring-type defect with R = 20 μm and r = 5 μm. The rf frequency is 1.5 GHz, RRR = 300, phonon mean free path = 1 mm, bath temperature = 2 K, magnetic field =800 Oe and the normal conducting defect resistance is 10 mΩ.

at the edge of the pit) is 1315 Oe which is slightly below the quench field of this pit defect of 1319 Oe. As can be seen from Fig. 6.11, the highest temperature located at the pit edge is 5.76 K. In contrast, the critical temperature of niobium at this field level (enhanced field at the edge of the pit) is 5.4 K. This confirms that the pit edge has become normal conducting, while inside the pit the niobium remains superconducting. As the field increases further, the normal conducting pit edge expands and finally leads to a thermal instability (quench), when the entire simulated niobium slab becomes normal conducting.

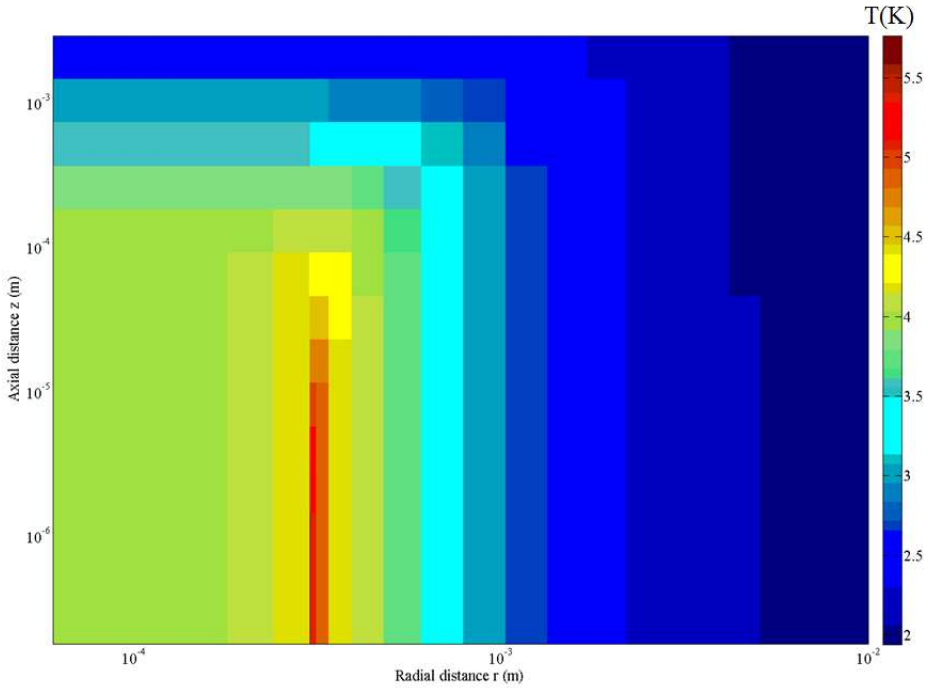

Figure 6.11: Temperature distribution in Kelvin over the cross section of the simulated niobium slab at a field level of 1315 Oe (enhanced field at the edge of the pit) which is slightly below the quench field of this pit defect of 1319 Oe. The diameter of the simulated niobium disk is 10 mm with 3 mm thickness. The field enhancement factor used at the edge of the pit corresponds to a pit of R = 30 μm diameter with a edge radius r of 1 μm. The helium bath temperature is 2 K. The rf surface in the image is at the bottom, and the side facing the helium is at the top.

Using two different pit diameters, the quench fields were calculated by the improved ring-type model for different magnetic field enhancement factors as shown in Fig. 6.12. In the blue colored region, all parts of the simulated niobium slab are superconducting. In the light red region, at least the edge of the pit has become normal conducting. Notice that the pit edge becomes normal conducting at rf fields lower than the quench field, especially for larger field

enhancement factors. This behavior provides an explanation for the heating observed at the location of a pit at fields below the quench field.

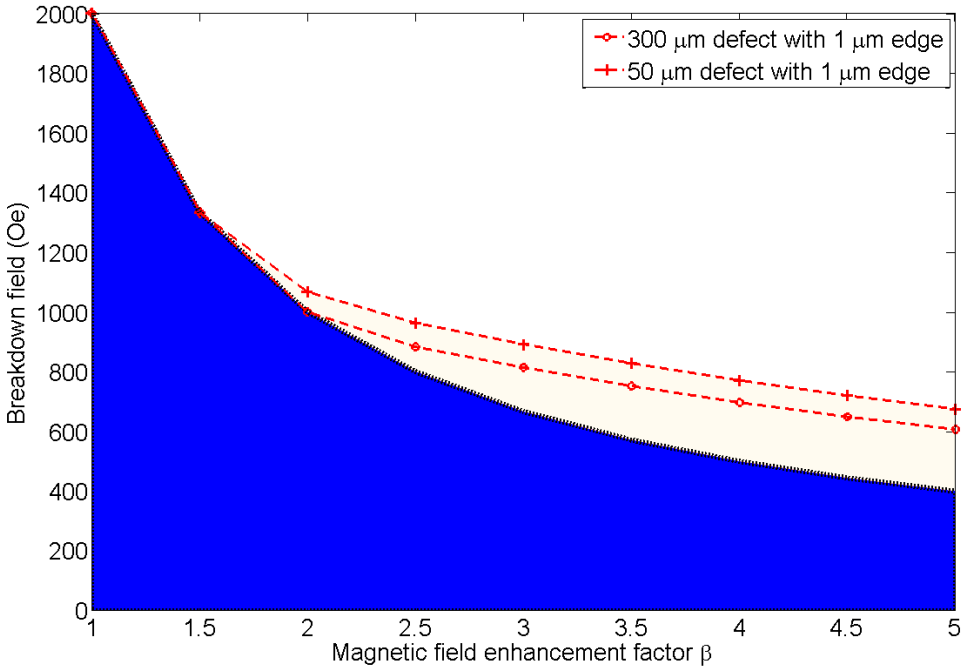

Figure 6.12: Quench fields v.s. magnetic field enhancement factors for two different ring defect sizes. In the blue color region, all parts of the simulated niobium slab are superconducting. In the light red region, at least the edge of the pit has become normal conducting.

In conclusion, the ring-type defect pit model with magnetic field enhancement at the pit edge predicts that the edge first gets normal conducting, but remains thermally stable, and then at a somewhat higher field (about a few percent), the whole cavity quench happens. The temperature map data for the sensors on top of the pits causing quench in the pit cavity shows the same: first a step in ΔT when the edge becomes normal conducting, and then the cavity quench at a slightly higher field as shown in Fig. 5.11.

6.3 Analysis of magnetic field enhancement in the pit cavity

By applying the magnetic field enhancement theory to the measured shape data of the pits in the pit cavity, the range of field enhancement factors and the range of local fields at the pit edges at the highest field achieved in the pit cavity (~ 555 Oe) can be calculated, as is summarized in Table. 6.1. Here local magnetic field at the pit edge $H_{local} = 0.98 * H_{pk,cavity} * \beta$.

The superheating field at 1.6 K is 1900 ~ 2300 Oe, depending on the purity of the niobium. From Table. 6.1, it can be seen that pit #30, #28, #27 and #22 are predicted to transition first to the normal conducting state at cavity fields near the measured quench field, since the local magnetic field is above the critical field. Indeed, the heating signals from pit #30 (see Fig. 6.13), #28 (see Fig. 6.14), #22 (see Fig. 6.15) measured by the T-map showed a clear jump in ΔT, i.e. a transition of the edge to the normal conducting state.

Fig. 6.16 shows the heating measured by T-map sensors versus magnetic field at the position of the pit #27. The maximum heating is about 200 mK when the cavity quenches. It does not have a clear jump compared to pit #30 and #28 of the same drill bit radius. It may be the case because the pit has a lower local magnetic field at the pit edge compared to pit #30 and #28, as shown in Table. 6.1. Fig. 6.17 shows the laser confocal images of pit #30, #28 and #27. It can be seen that there are some visible differences among the pit edge radii of the three pits. Pit #30 and #28 have sharper edges, and #27 does not.

The MFE model correctly predicts which pits have the largest MFE and thus should become normal conducting first, and ultimately will limit the performance of the cavity by causing it to quench. It also correctly predicts the ap-

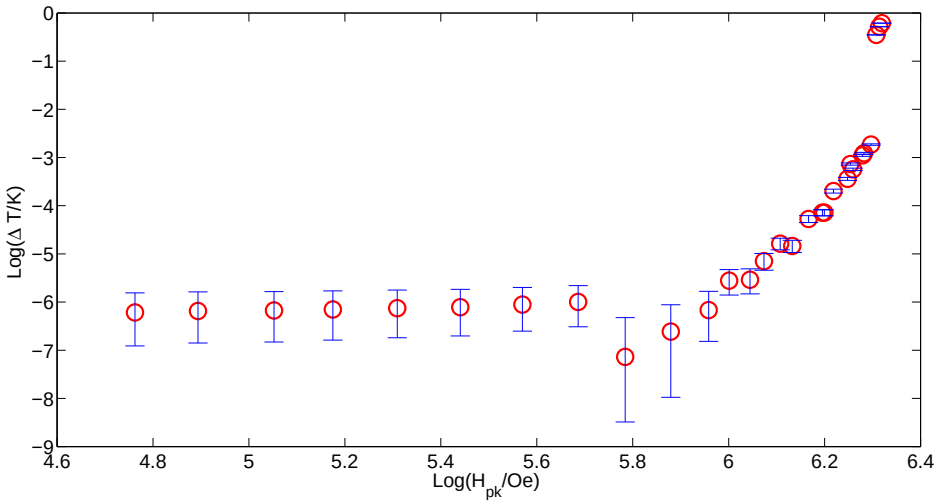

Figure 6.13: Heating measured by the temperature mapping sensor versus magnetic field at the position of the pit #30. The data is plotted on a log scale. The surface magnetic field on the horizontal axis is the peak surface field of the cavity, not taking into account the local field enhancement by the pits.

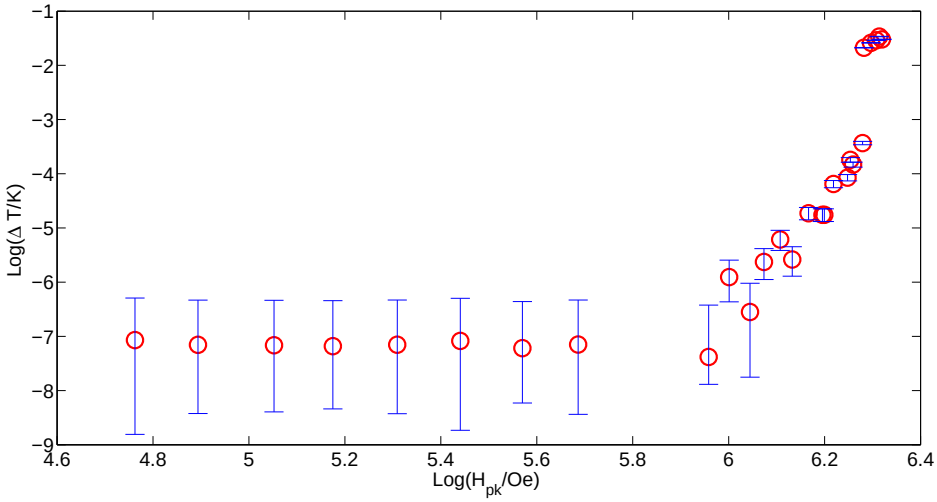

Figure 6.14: Heating measured by the temperature mapping sensor versus magnetic field at the position of the pit #28. The data is plotted on a log scale. The surface magnetic field on the horizontal axis is the peak surface field of the cavity, not taking into account the local field enhancement by the pits.

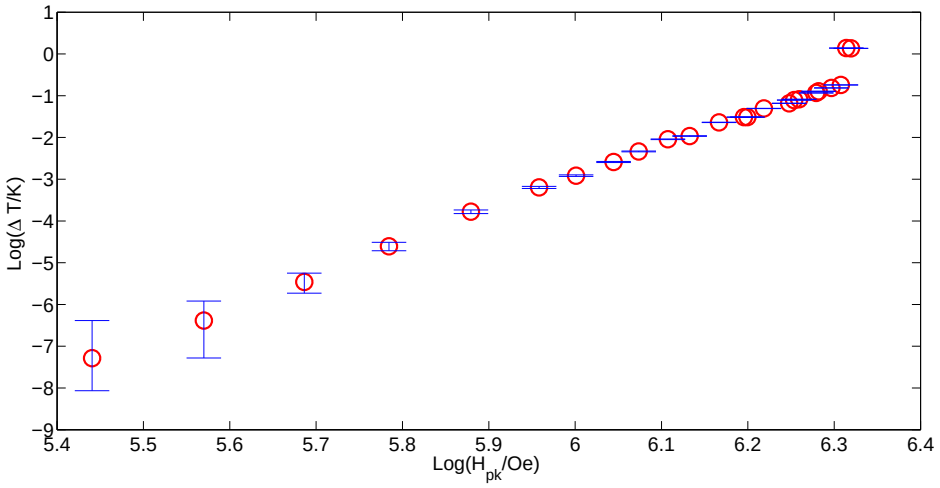

Figure 6.15: Heating measured by the temperature mapping sensor versus magnetic field at the position of the pit #22. The data is plotted on a log scale. The surface magnetic field on the horizontal axis is the peak surface field of the cavity, not taking into account the local field enhancement by the pits.

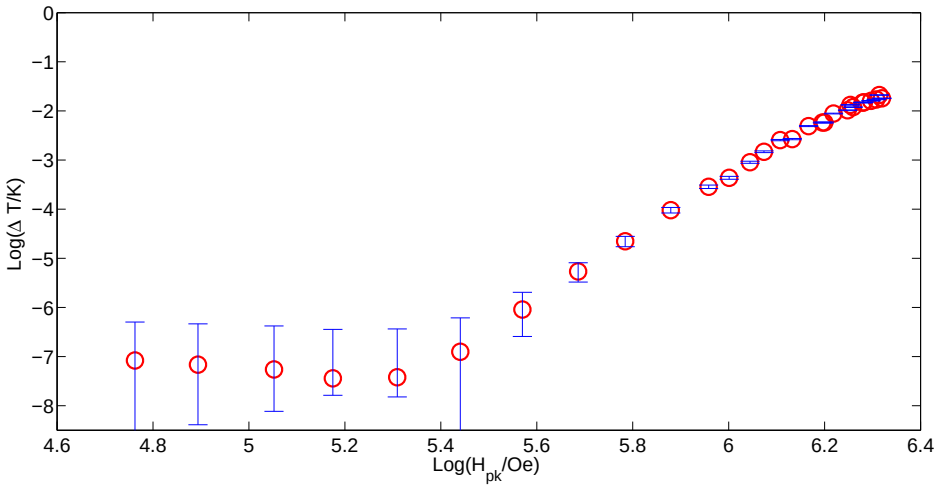

Figure 6.16: Heating measured by the temperature mapping sensor versus magnetic field at the position of the pit #27. The data is plotted on a log scale. The surface magnetic field on the horizontal axis is the peak surface field of the cavity, not taking into account the local field enhancement by the pits.

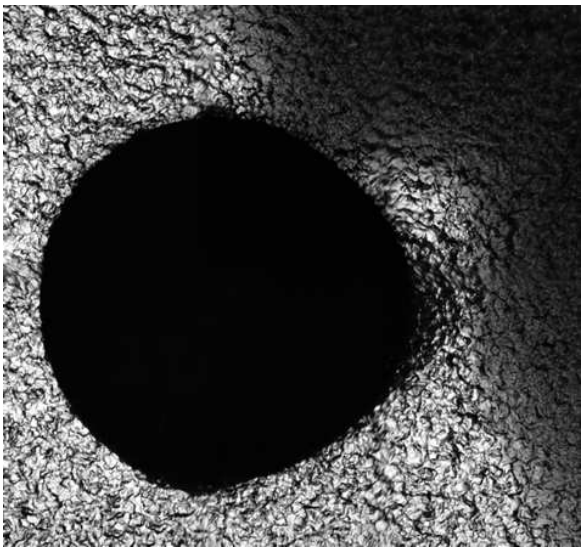

(a) Pit #30

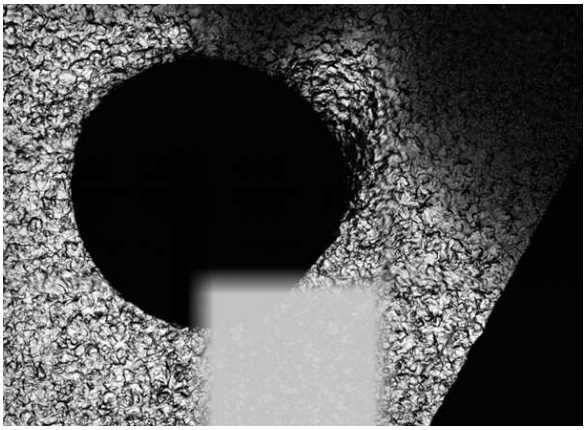

(b) Pit #28

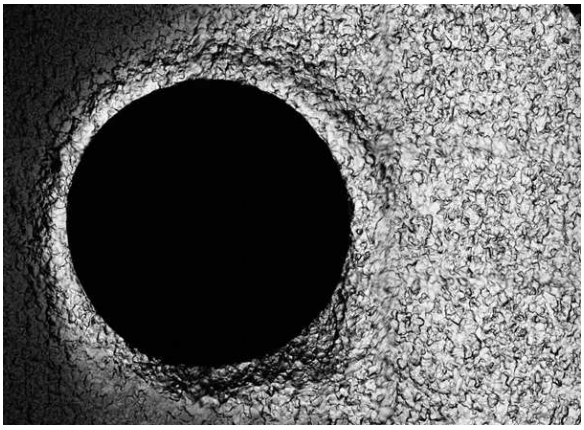

(c) Pit #27)

Figure 6.17: Laser confocal microscopy picture of three pits #30 (top), pits #28 (middle) and pits #27 (bottom).

Table 6.1: The magnetic field enhancement calculation results based on the geometrical parameters of the artificial pits (I): the pits that have effective temperature readings measured by the T-map.

Pit number	Pit drill radius (μm)	Range of pit edge radius r (μm)	Range of pit radius R (μm)	Range of magnetic field enhancement factor $\beta = 1.17*(r/R)^{-1/3}$	Range of local magnetic fields at H_{pk} reached in the pit cavity (Oe)
#30	750	5~30	850~900	3.6~6.6	1940~3560
#27	750	20~55	800~850	2.9~4.1	1560~2210
#28	750	15~45	790~810	3.0~4.4	1620~2370
#23	600	30~60	520~550	2.4~3.1	1290~1670
#24	600	25~60	580~610	2.5~3.4	1350~1830
#22	600	5~45	570~610	2.7~5.8	1460~3130
#19	600	20~55	550~600	2.5~3.6	1350~1940
#20	600	35~60	570~600	2.5~3.0	1350~1620
#7	300	20~50	280~310	2.1~2.9	1130~1560
#6	200	25~55	180~210	1.7~2.4	910~1290
#2	200	35~60	190~200	1.7~2.1	910~1130

proximate field at which that should happen. This shows that the pits found in srf cavities can cause quench and thus limit the performance of the cavity only if their edge radius is a few μm and if they are in the high magnetic field region. This also explains why some pits are a problem and others are not.

6.4 Analysis of high field behavior of the superconducting pit edges

In addition to the two quench causing pits verified by T-map sensors, there are 9 pits that do not cause quench, but still showed measurable heating signals. Assuming there is magnetic field enhancement at these pit edges, the temperature rise information versus real local magnetic field can provide new valuable information about the high field Q-slope.

At low fields, assuming that the surface resistance is field independent, one expects the heating signal will be proportional to H^2. Fig. 6.18 shows the heating versus magnetic field for pit #2 and #6. It clearly shows an ohmic behavior due to a field-independent BCS surface resistance.

Fig. 6.19 shows the heating signals versus magnetic field of pit #22 and #19. For pit #19, below field level of $\log(H_{pk}/Oe) < 4.6$, the pit heating signal is so small that it is below noise level. Within the field range of $5.6 < \log(H_{pk}/Oe) < 6.2$, the heating signal obeys a power law with an exponent of 8. Above field level of $\log(H_{pk}/Oe) > 6.2$, the heating signal does not show an abrupt jump as those pits that induce cavity quench but rather increases more slowly with a power law of an exponent of 4. The maximum heating is about 450 mK when the cavity quenches.

Fig. 6.20 and 6.21 shows the heating signals versus magnetic field of pit #24, #23 and #7. The heating signals also can be clearly divided into three sections as described previously for the case of pit #19, shown in Fig. 6.19(b).

The slope information from the pit heating is summarized in Tab. 6.2, taking

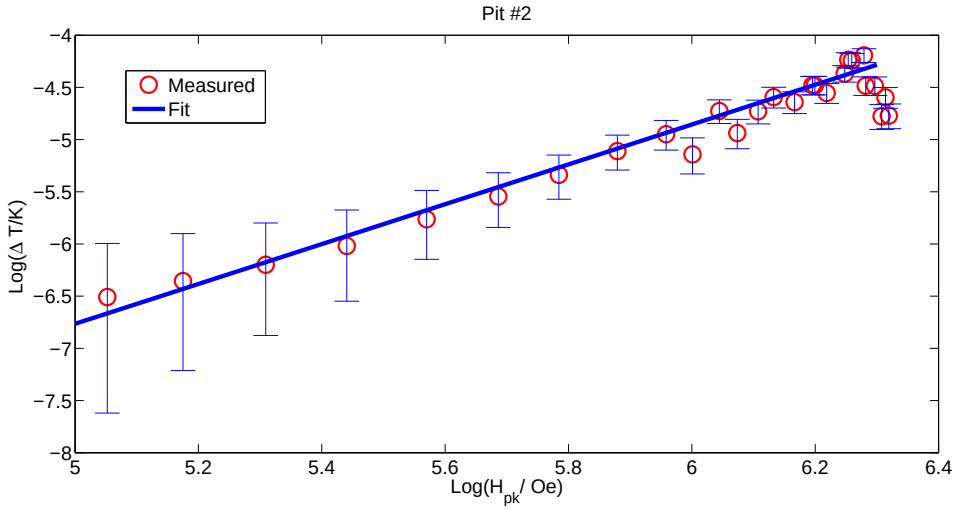

(a) Pit #2

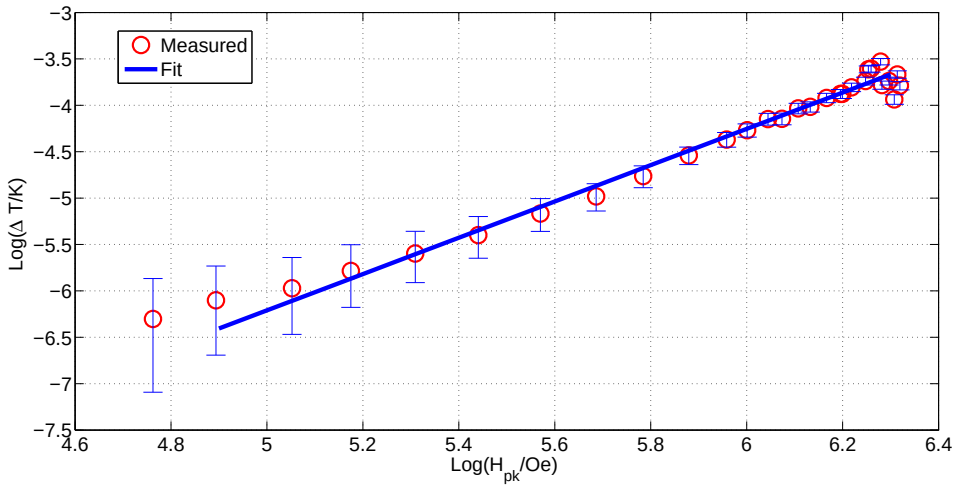

(b) Pit #6

Figure 6.18: Measured heating signals versus magnetic field for pit #2 (top) and #6 (botoom) with the smallest drill bit radius of 200 μm. Both fit has a slope of 2 in the log-log graph, i.e., the heating is proportional to H^2. The surface magnetic field on the horizontal axis is the peak surface field of the cavity, not taking into account the local field enhancement by the pits.

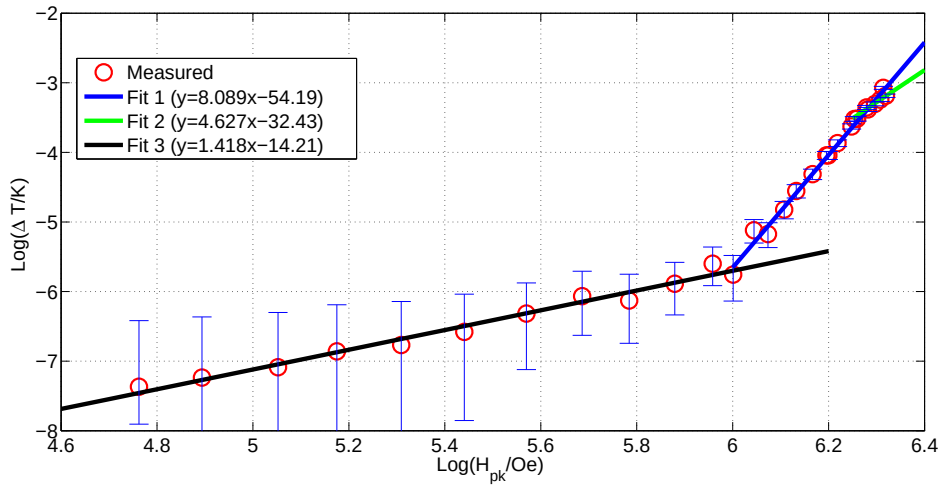

(a) Pit #20

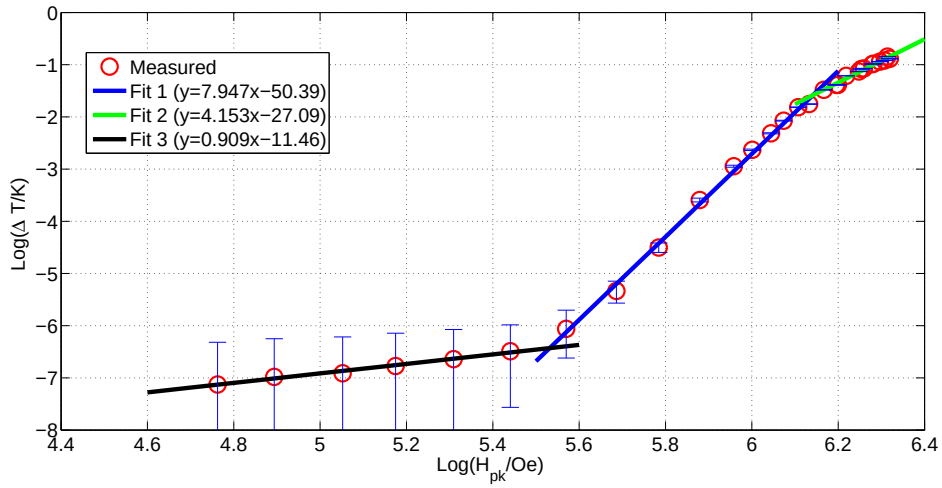

(b) Pit #19

Figure 6.19: Measured heating signals versus magnetic field for pit #22 (top) and #19 (bottom) with a drill bit radius of 600 μm. The surface magnetic field on the horizontal axis is the peak surface field of the cavity, not taking into account the local field enhancement by the pits.

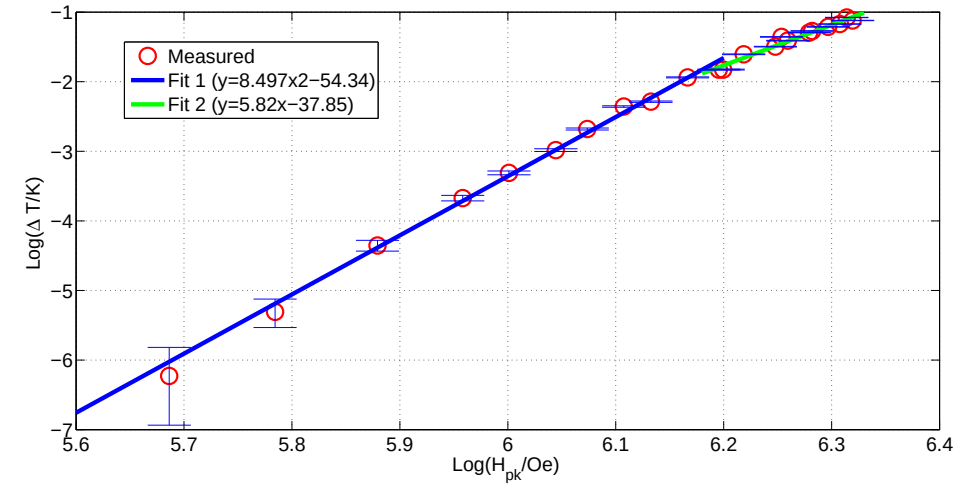

(a) Pit #24

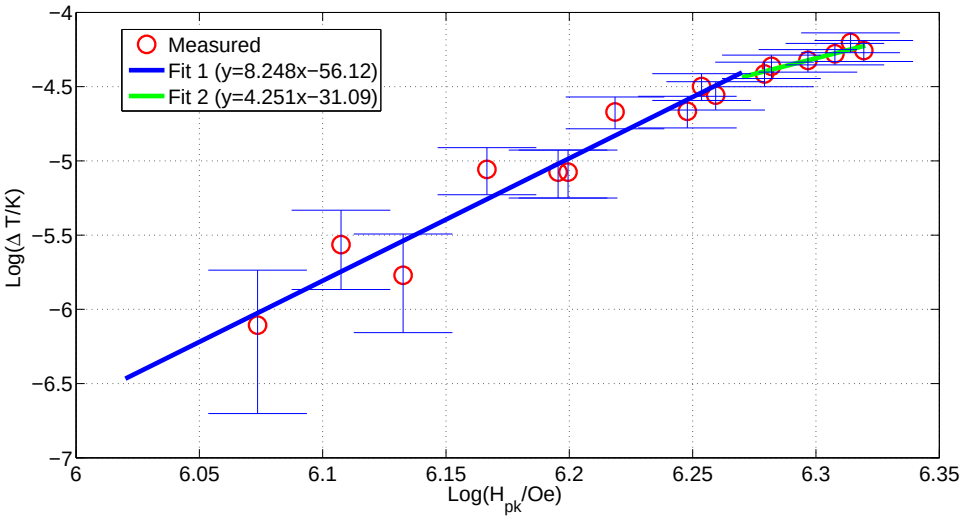

(b) Pit #23

Figure 6.20: Measured heating signal versus magnetic field for pit #24 (top) and #23 (bottom) with a drill bit radius of 600 μm. The surface magnetic field on the horizontal axis is the peak surface field of the cavity, not taking into account the local field enhancement by the pits.

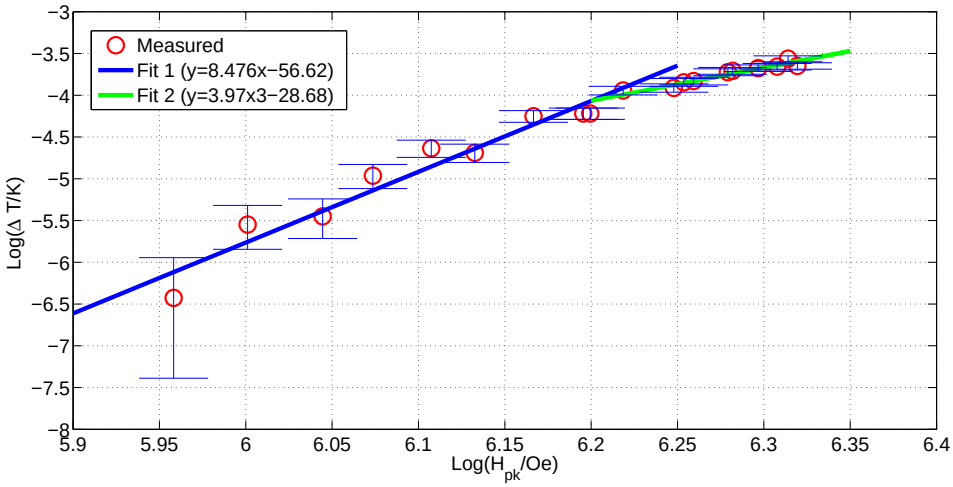

Figure 6.21: Measured heating signal versus magnetic field for pit #7 with a drill bit radius of 300 μm. The surface magnetic field on the horizontal axis is the peak surface field of the cavity, not taking into account the local field enhancement by the pits.

into account the local magnetic field enhancement factors as given in Table. 6.1.

The following observations can be made based on the slope of the pit heating signals.

- At low field, the heating is proportional to H^2, as one would expect for ohmic heating;
- At higher fields, there is clear transition to a strong non-linear behavior, with a final slop of $\log(\Delta T/K)$ versus $\log(H_{pk}/Oe)$ of 4 to 5 at highest fields. This points to a strong field dependence of the BCS surface resistance, for local fields in the 1000 ~ 2000 Oe region at the edges of the pits. It should be noted here that the situation is rather complex, since only a small area at the pit edge is at high fields, and it is not uniform. Nevertheless, from

Table 6.2: Slope information from fitting the field dependence of the heating signals of the pits (Only for pits that do not cause quench).

Pit number	Slope of $ln(\Delta T/K)$ vs $ln(H_{pk}/Oe)$ in field region I (H_{local} < 800 Oe)	Slope of $ln(\Delta T/K)$ vs $ln(H_{pk}/Oe)$ in field region II (800 Oe < H_{local} < 1300 Oe)	Slope of $ln(\Delta T/K)$ vs $ln(H_{pk}/Oe)$ in field region III (H_{local} > 1300 Oe)
#27	~ 2	6.2	4.3
#28	~ 2	10.0	5.0
#23	~ 2	8.3	4.2
#24	~ 2	8.4	4.8
#19	~ 2	7.8	4.1
#20	~ 2	8.1	4.6
#7	~ 2	8.5	4.0
#6	1.92	N/A	N/A
#2	1.97	N/A	N/A

the slope information one concludes that the BCS surface resistance scale with the magnetic field to a power of 4 to 6 at medium fields, and with a power of ~ 2 of the high fields above 1300 Oe.

- The transition to field dependent surface resistance happens at fields similar to where the high field Q-slope starts in BCP cavities (~ 900 Oe), taking into account the MFE at the pit edges;
- The pit heating data shows that a BCS cavity surface can reach high fields close to the superheating field. The strong Q-slope found in BCS cavities above ~ 900 Oe thus is likely caused by a combination of a non-linearity of

the BCS surface resistance and thermal feedback caused by the increased rf losses over a larger area. For the pit edges, the high field area is very small, so the total power disposed is small and thermal feedback is less important.

These results will be useful to guide future theoretical work on understanding the field dependence of the surface resistance.

CHAPTER 7

SUMMARY AND OUTLOOK

A TE sample host cavity is desirable for basic srf material research because it allows to rapidly test small, flat sample plates. In the past it has been found very challenging to reach meaningful fields on the sample plate and to reach good sensitivity in rf surface resistance at the same time. I have designed and fabricated a new generation of TE host cavities: a pillbox shape and a mushroom shape cavity. For the first time I was able to reach good rf magnetic fields (> 60 mT) and good sensitivity (nΩ) in such a cavity at the same time. Both the TE pillbox cavity and the TE mushroom cavity are now ready for studying alternative materials for srf applications such as Nb_3Sn and MgB_2. I have already tested a flat Nb_3Sn sample plate using the TE pillbox cavity. The current performance of the two TE sample host cavities is limited by losses in the rf input coupler and by thermal breakdown due to rf heating at the high rf frequency (6 GHz). Future work will focus on reducing the rf losses of the input coupler by increasing the coupling loop area or by making it superconducting using high purity niobium. The thermal breakdown field will be increased by reducing the rf surface resistance of the host cavity and by increasing the thermal conductivity of the niobium walls of the host cavity.

The small pits often found on the inner surface of srf cavities are frequently limiting the maximum field gradient in these cavities. However not all pits present a problem to cavity performance. So it is very desirable to study those pits systematically to determine the related parameters. I have made a single cell cavity with 30 artificial pits in the high magnetic field region to gain new insight in how pits limit the cavity performance. The relevant parameters are

the pit diameter, the pit edge radius and the pit height. The test of the pit cavity showed clear evidence that the edges of two of the largest radius pits transitioned into the normal conducting state at a field just below the quench field of the cavity, and that the quench was indeed induced by these two pits. I also measured the shape of the 30 pits by laser confocal microscopy. Predictions by a magnetic field enhancement factor $\beta \sim (r/R)^{-1/3}$ model which depends on the radius of the pits R and the radius of the edge of the pits r is in good agreement with the observed behavior of the artificial pits in the cavity. I also developed a ring-type defect model which gives further insight into the heating and quench behavior of pits. The pits also give some new insight into the non-linear surface resistance of niobium at high fields.

BIBLIOGRAPHY

[1] H. Padamsee, J. Knobloch, T. Hays, RF Superconductivity for Accelerators, John Wiley and Sons, 1998.

[2] R. Geng, et.al., *"HIGH GRADIENT STUDIES FOR ILC WITH SINGLE-CELL RE-ENTRANT SHAPE AND ELLIPTICAL SHAPE CAVITIES MADE OF FINE-GRAIN AND LARGE-GRAIN NIOBIUM"*, Albuquerque, New Mexico, USA.

[3] G. Catelani and James P. Sethna, *"Temperature dependence of the superheating field for superconductors in the high-κ London limit "*, PHYSICAL REVIEW B 78, 224509 (2008)

[4] A. Gurevich, Appl. Phys. Lett. 88, 012511 (2006)

[5] Y. Iwashita, *"Developement of high resolution camera and observations of superconducting cavities"*, EPAC08, Genoa, Italy.

[6] J. Laurent AND H. Padamsee, CERN/EF/RF 83-2.

[7] A. Romanenko and R.Russo, *"RF properties at 6 GHz of ultra-high vacuum cathodic arc films up to 450 oersted"*, SRF05, Ithaca, New York, USA.

[8] S. Tantawi, et.al., *"Superconducting materials testing with a high-Q copper RF cavity"*, PAC07, Albuquerque, New Mexico, USA.

[9] Liang, C, *"A New Surface Resistance Measurement Method with Ultrahigh Sensitivity"*, PhD thesis. 1993, Virginia Polytechnic Institute and State University: Blacksburg, Virginia.

[10] T. Junbinger, PhD Thesis, 2012, University of Heidelberg, Germany.

[11] B. Xiao, PhD Thesis, 2012, William and Marry University, USA.

[12] Y. Xie, Hasan Padamsee, Alexander Romanenko, *"Relationship Between Defects Pre-Heating and Defects Size"*, SRF2009, Berlin, Germany.

[13] Yi Xie, Matthias Liepe, Hasan Padamsee, *"THERMAL MODELING OF RING-TYPE DEFECTS"*, SRF2009, Berlin, Germany.

[14] H. Padamsee, RF Superconductivity, Science, Technology, and Applications, Wiley-VCH, 2009.

[15] D.C. Mattis and J. Bardeen, Phys. Rev.,111:412,1958.

[16] J. Knobloch, PhD thesis, Cornell University, 1997.

[17] D. Myakishev and V. Yakovlev, *"The new possibilities of SuperLANS code for evolution of axisymmetric cavities"*, PAC95, Texas, USA.

[18] Matlab 2007a, The Mathworks, Inc.

[19] ANSYS 2009, The ANSYS, Inc.

[20] G. Eremeev, PhD thesis, Cornell University, 2008.

[21] B. Visentin, *"Low, Medium, High Field Q-Slopes Change With Surface Treatments"*, ANL-05/10, Argonne, 2004

[22] J. Vines, et.al., *"Systemtic trends for the medium-field Q-slope"*, SRF07, Beijing, China.

[23] J. Knobloch, et.al., *"High field Q-slope in superconducting cavities due to magnetic field enhancement"*, SRF99, Santa Fe, New Mexico.

[24] G. Ciovati, PhD thesis, Old Dominion University, 2005.

[25] M. Rabinowitz, Appl. Phys. Lett.19, 73 (1971)

[26] A. Romanenko, PhD thesis, Cornell University, 2009

[27] D. Rubin, et.al., *"Observation of a narrow superconducting transition at 6 GHz in crystals of $YBa_2Cu_3O_7$"*, Phys. Rev. B 38, 6538-6542 (1988).

[28] MWS 2009, The CST, Inc.

[29] Yi Xie and Matthias Liepe, *"COUPLER DESIGN FOR A SAMPLE HOST TE CAVITY"*, SRF11, Chicago, USA.

[30] Haipeng Wang, et.al., TUP11, PAC11, New York, USA

[31] M. Liepe, PhD thesis, University of Hamburg, German, 2001

[32] F. Koechlin and B. Bonin. *"Parametrization of the niobium thermal conductivity in the superconducting state"*. SRF95, Gif sur Yvette, France, 1995

[33] K. Mittag. Cryogenics 73 (1973) 94.

[34] S. Posen et. al., *"RECENT DEVELOPMENTS IN THE CORNELL Nb3Sn INITIATIVE"*. IPAC12, New Orleans, USA, 2012.

[35] G. Mller et. al., EPAC 1996. p. 2085.

[36] D. Gonnella et. al., *"QUENCH STUDIES OF A SUPERCONDUCTING RF CAVITY"*. IPAC12, New Orleans, USA, 2012.

[37] Q. S. Shu, et.al., *"Experimental Investigation of Quenches in Superlluid He of TESLA 9-Cell Superconducting Cavities"*, SRF1995, Gif-sur-Yvette, France.

[38] Lie-Quan Lee, Zenghai Li, Cho Ng, and Kwok Ko, Tech. Rep., SLAC-PUB-13529, 2009, *"Omega3P: A Parallel finite-Element Eigenmode Analysis Code for Accelerator Cavities"*

[39] Richard S. Varga, Matrix Iterative Analysis, Second ed., Springer-Verlag, 2002

[40] Y. Iwashita, *"Evaluation of Magnetic Field Enhancement Along a Boundary"*, Linac04, Lubeck, Germany.

[41] V. Shemelin, H. Padamsee, *"Magnetic field enhancement at pits and bumps on the surface of superconducting cavities"*, SRF Report 080903-04, Cornell University.

[42] K. Tian et.al., *"BENCHMARK OF DIFFERENT ELECTROMAGNETIC CODES FOR THE HIGH FREQUENCY CALCULATION"*, PAC09, Vancouver, Canada